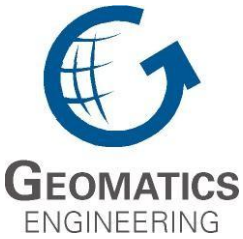

UCGE Reports
Number 20323

Department of Geomatics Engineering

Geometric Modelling of 3D Range Cameras and their Application for Structural Deformation Measurement

(URL: http://www.geomatics.ucalgary.ca/graduatetheses)

by

Sonam Jamtsho

December 2010

UNIVERSITY OF CALGARY

Geometric Modelling of 3D Range Cameras and their Application for Structural Deformation Measurement

by

Sonam Jamtsho

A THESIS

SUBMITTED TO THE FACULTY OF GRADUATE STUDIES

IN PARTIAL FULFILMENT OF THE REQUIREMENTS FOR THE

DEGREE OF MASTER OF SCIENCE

DEPARTMENT OF GEOMATICS ENGINEERING

CALGARY, ALBERTA

December 2010

Abstract

Three-dimensional range cameras are the state-of-the-art range imaging technology which has potential for various close-range high-precision metric applications. One of such application is measuring the structural deformation under external loading condition.

The SR4000 range camera was used for beam deflection measurement because it is less prone to scene-dependent errors such as the scattering artefact. The deformation test was conducted on two concrete beams with and without the steel-reinforced polymer sheets in an indoor testing facility. The measurement precision and accuracy for the 65 mm deformation test for both the concrete beams are within 1 mm. Further test on the concrete beam with the steel-reinforced polymer sheets has shown that even 3 mm deformation can be reliably detected with measurement precision of 0.3 mm and accuracy of 0.4 mm. These results clearly indicate the high metric potential of 3D range cameras in spite of their coarse imaging resolution and low single point accuracy.

Acknowledgements

Indeed, this thesis would have never been accomplished without the generous support of my supervisor, Dr. Derek Lichti who is an Associate Professor in the Department of Geomatics Engineering. His extensive help ranged from fixing the simplest programming bugs to providing valuable research guidance over the last two years. His dedication and support is truly amazing. He never gets tired of editing the same material over and over again. In addition, I thank him for providing the Graduate Research Scholarship (NSERC fund) to support my research activity since January 2009.

I would like to thank Dr. Mamdouh El-Badry (Department of Civil Engineering) for designing the structural beams for the deformation test and allowing me to carry out the range camera experiment along with other research groups. I am very thankful to Mr. Dan Tilleman for his extensive technical support throughout the duration of the deformation test. Thanks also to Mr. Mirsad Berbic for helping us to build the camera housing for the deformation test.

I would also like to thank the group members of the Imaging Metrology Group (IMG), especially Sherif Halawany, Herve Lahamy, Ting On Chan and Jacky Chow for helping me to conduct the scattering and deformation experiments. I am very grateful to Sherif and Jacky for painstakingly segmenting the laser scanner point clouds and registering the targets of the two range cameras. I am also thankful to Ivan Detchev and Adam Jahraus for helping me during the deformation test.

I met few good people in Calgary who made my livelihood better especially in 2010. One among them is Ms. Phung Lam who provided me with many opportunities to participate in numerous activities from watching "Meteor Shower" to exploring the majestic lakes and mountains in and around Calgary. Her friendship truly uplifted my spirit and gave me bountiful experiences, besides the mundane life of a graduate student. Thank you, Phung, for giving me wonderful experiences in Calgary.

Last but not the least, I would like to extend my gratitude to the Royal Government of Bhutan for providing subsidiary funding support for traveling and other needs during the two years of my graduate studies.

To my mother, **Yangzom** *who still ignorantly believes that the sun is moving around the earth yet her simplicity and unconditional love transcends over my understanding of the earth moving around the sun*

Table of Contents

List of Figures

List of Tables

Abbreviations

AP	**A**dditional **P**arameter
AIC	**A**kaike **I**nformation **C**citerion
CW	**C**ontinuous **W**ave
CCD	**C**harge **C**oupled **D**evice
CMOS	**C**omplimentary **M**etal **O**xide **S**emiconductor
DFT	**D**iscrete **F**ourier **T**ransform
ESF	**E**dge **S**pread **F**unction
EOP	**E**xterior **O**rientation **P**arameter
FOV	**F**ield **o**f **V**iew
GPS	**G**lobal **P**ositioning **S**ystem
LED	**L**ight **E**mitting **D**iode
LVDT	**L**inear **V**ariable **D**ifferential **T**ransducer
PMD	**P**hotonic **M**ixing **D**evice
PSF	**P**oint **S**pread **F**unction
RC	**R**ange **C**amera
RIM	**R**ange **IM**aging
RF	**R**adio **F**requency
RMSE	**R**oot **M**ean **S**quare **E**rror
SV	**S**tereo **V**ision
SNR	**S**ignal to **N**oise **R**atio
SRP	**S**teel **R**einforced **P**olymer
ToF	**T**ime **o**f **F**light
TLS	**T**errestrial **L**aser **S**canner

Chapter 1

Introduction

"Our future discoveries must be looked for in the sixth place of decimals", said by Albert A. Michelson, a Nobel laureate who precisely measured the speed of light.

All that remains in photogrammetry is to work towards more and more precise measurement. That is the ultimate goal of this thesis.

1.1 Background

Three-dimensional (3D) range imaging camera systems are a recent development for close-range terrestrial photogrammetric applications. They operate based on the phase-shift principle to determine the distance between the target and the camera. Each pixel in the sensor frame independently measures distance and amplitude information of the scene which is realized through CCD/CMOS lock-in pixel technology (Lange, 2000). Unlike 3D laser scanners, a range camera does not need to sequentially scan its field of view to collect spatial and radiometric information. The range and the amplitude information are obtained simultaneously by sampling the returned modulated optical signal at every element location of the solid-state sensor.

After the advent of the 3D range cameras the range based applications have gained substantial research interest due to the ease of obtaining the 3D information of the imaging environment. Three-dimensional range cameras have been used in imaging applications in various fields ranging from facial recognition to robotic vision. The use of range cameras has been reported in various fields of applications such as robotic and machine vision in the field of mobile robotic search and rescue (Wiedemann et al., 2008; Ellekilde et al., 2007;

Bostelman et al., 2005), gesture recognition for human-computer interaction (Lahamy and Lichti, 2010; Li and Jarvis, 2009; Kollorz et al., 2008; Breuer et al., 2007; Hansen et al., 2007), 3D sensing for automated vehicle guidance and safety system, and wheelchair assistance (Bostelman and Albus, 2007; Bostelman et al., 2006), outdoor surveillance (Falie and Buzuloiu, 2008b), and biometrics application such as for facial recognition through enhanced depth mapping (Hansen et al., 2007).

The downside of the range imaging technology is that this device is still in its infant stage, which means that the technology is not completely evolved in terms of the software and hardware developments. The miniaturized silicon sensors are not completely able to account for dubious signals caused by signal attenuation due to multipath or scattering errors. Besides, the range camera also suffers from standard lens distortions and rangefinder errors. Like any other optical measuring devices, the observations of the range camera are biased by geometric and radiometric distortions, which need to be accounted for through a calibration process. The methodology of camera calibration is well established for all 2D imaging cameras, however, the 3D range cameras are not able to be calibrated efficiently using traditional approach due to the complicated systematic biases such as scattering effect on the range measurements. Nevertheless, research is underway for developing a calibration procedure for the range cameras by incorporating range measurements in a self-calibration approach (Lichti et al., 2010; Robbins et al., 2009; Lichti, 2008; Karel, 2008) or by separately modelling the range distortions beside performing standard digital camera calibration in a two-step calibration process (Boehm and Pattinson, 2010; Beder and Koch, 2007; Lindner and Kolb, 2006; Reulke, 2006).

1.2 Motivation

Three-dimensional range cameras such as the latest generation MESA Swissranger SR4000 is highly accurate measuring device. It can be potentially explored for high-precision metric applications such as for measuring the structural deformation under external loads. The structural deformation measurements are particularly important for civil engineering in order to assess the strength of the structural members under different loading environments. More importantly, the structures used in buildings and bridges are subject to fatigue while exposed to various environmental conditions leading to deterioration of member strength and other structural properties. Therefore it is necessary to continually monitor the health of the structures in order to mitigate any impending danger as a result of the structure failures. One method of assessing the health of the structures is by measuring the beam deflection under external forces in laboratory settings.

So far, the deflection measurements were measured using a 1D laser transducers and bulky photogrammetric and terrestrial systems such as the multiple system of digital cameras and the terrestrial laser scanners respectively. The use of miniaturized range cameras for structural deformation measurement is superior to the terrestrial laser scanner because the range camera is a compact system which facilitates faster field operation and accessibility even in congested sites, and it is many times cheaper than the scanner system. Additionally, it can capture the 3D scene in a few seconds of exposure time whereas the laser scanners have to scan the whole imaging scene which is more time consuming. The range camera is advantageous over the photogrammetric multiple camera system because it can directly obtain the 3D information of the scene using only one camera without having to undergo tedious processing steps required for the stereo-photogrammetry. Lastly, the range cameras is a viable alternative to the 1D laser transducer because it can provide dense point cloud of the surface unlike the point based measurement system of the laser transducers.

The RIM technology in the SR4000 range cameras acquires three dimensional measurements of the scene thus facilitating accurate modelling of the captured surface. Additionally, RIM cameras acquire area-based images at a high acquisition speed capturing up to 54 frames per seconds which can be used for capturing dynamic scenes for kinematic applications that are not possible with any of the prevailing beam deflection measurement systems. Such potential of the non-contact sensors like 3D range camera presents new avenues of application in static and dynamic scene analysis for structural deformation measurements, which certainly deserves further research attention in this technology.

However, a ToF camera suffers from significant geometric errors (Mure-Dubois and Hugli, 2007; Guomundsson et al., 2007; Kahlmann et al., 2006), which have to be rectified in order to achieve high measurement accuracy. The modelling of systematic errors can be achieved in a self-calibration approach where all the model parameters comprising of both lens and range related error terms are estimated simultaneously. Such a robust calibration method is perhaps more accurate than a un-integrated calibration approach because it accounts for the composite structure made of various components. Nevertheless, the self-calibration method is biased because it portrays a high correlation between the model parameters that are supposed to be independent of each other. Additionally, the problem of over-parameterization is a big issue in model identification when many highly-correlated parameters are involved in the system. So there is a need to accurately select the best model parameters for self-calibration of the 3D range cameras. Hence, an Akaike Information Criterion method of model identification has been proposed to solve the ambiguity posed by the correlated model parameters.

The self-calibration method of the range cameras does not account for the range errors caused by the scene-dependent scattering artefact because these range errors are difficult to model accurately using a general physical model. In the 3D range cameras, the scattering artefact is caused by the secondary reflections occurring between the lens and the image plane. The reflected beam from the foreground objects undergoes multiple reflections within the camera device thereby introducing parasitic signals that bias the late-arrival, backscattered signals from the background targets. These additive signals cause degradation of the depth measurements for the farther objects thus limiting the use of such camera for high precision close-range photogrammetric applications. Experimental results from the SR3000 range camera show range bias of up to 2500 mm on the background range image in presence of the foreground object. Such scattering-induced range bias prohibits the use of range cameras for various metric applications.

Only few attempts had been made to quantify the scattering effect caused by the multiple signal attenuation. Mure-Dubois and Hugli (2007) and Kavli et al. (2008) have published results on compensation of the scattering bias using inverse filtering approach, where they basically use a trial and error method of defining the inverse filter based on Gaussian or empirically defined PSF approximation. Nonetheless, the linear system model presented by them is questionable because the scattering effect is non-linear and highly scene-variant. Such scene-dependent errors are highly variable and complex which necessitates further definition and investigation. In the absence of strong physical basis, the only alternative is to empirically formulate the range distortions through exhaustive experimentations.

1.3 Literature Review

1.3.1 Geometric Distortions

Like any other digital imaging sensors, the 3D range cameras are biased with radiometric and geometric distortions. The systematic errors of the ToF cameras range from standard camera distortions like radial and decentring lens distortions to more complicated range biases due to surface reflectivity (Falie and Buzuloiu, 2008a; Oprisescu et al., 2007), incidence angle (Karel et al., 2007), scattering artefact (Jamtsho and Lichti, 2010; Chiabrando et al., 2010; Karel et al., 2010; Kavli et al., 2008; Mure-Dubois and Hugli, 2007), internal camera temperature and integration time (Kahlmann et al., 2006), multipath (Guomundsson et al., 2007), amplitude attenuation (Jaakkola et al., 2008) and internal electronic noises (Falie and Buzuloiu, 2007; Lange and Seitz, 2001; Lange, 2000).

The measurement accuracy of the range cameras defines the applicability of such cameras for various applications. Due to the infancy of the 3D ranging and imaging technology, as of yet, it has not been able to realize the full potential of the range sensors owing to range distortions. However, research is underway to enhance the camera potential through rigorous calibration process. Chiabrando et al. (2009) investigated two aspects of the calibration of SR4000 range camera: first part deals with the range measurements as a function of warm up time period and incidence angle; and second part deals with the amplitude calibration as a function of range. Beder and Koch (2007), Reulke (2006) and Santrac et al. (2006) focussed on estimating the standard camera parameters such as principal distance, principal point offset and lens distortions. Kahlmann et al. (2006) investigated calibrating the distance of one central pixel as a function of range between the camera and the target, integration time, and internal and external temperature. Fuchs and May (2007), Lindner and Kolb (2006) and Du et al. (2005) used two step calibration process: standard camera calibration to quantify the intrinsic camera parameters; and depth calibration to quantify the systematic range distortions. The other calibration processes deals with integrated self calibration method such as by Lichti et al. (2010), Robbins et al. (2009), Lichti (2008) and Karel (2008).

1.3.2 Scattering Distortion

Mure-Dubois and Hugli (2007) and Kavli et al. (2008) discuss the scattering artefact in the ToF cameras and the correction model based on shift-invariant linear system model for compensating the scattering effects on the range measurements. According to Mure-Dubois and Hugli (2007), the scattering problem is loosely expressed as a convolution of the input signal with the impulse response of the system in presence of the scattering bias. For the scattering phenomenon occurring in the 3D range cameras, the measured signal in every pixel is equal to the convolution of the input signal and the point-spread function of the camera including the scattering bias. The solution to this problem explicitly requires modelling of the scattering PSF of the camera so that a method of deconvolution can be employed to undo the effect of the scattering. They used a linear shift-invariant system model to quantify the scattering bias using a blind-deconvolution approach where the point-spread function of the camera including scattering bias is plausibly defined by a trial and error method using a Gaussian approximation. This method is limited due to the non-idealization of point source of light from the camera for measuring the point-spread function, which is fundamental in the linear-system model.

Kavli et al. (2008) uses the same approach of linear system model to compensate for the scattering distortions in ToF cameras using "generally shaped empirical models" for the

point spread function. Plus the size of PSF is the same as the image, unlike a maximum size of 64 by 64 kernel used in the former method. The filtering process is solved by using the forward model iteratively with the compensation model moving from the brightest part to the dimmest parts subtracting the scattering effects from the measurements sequentially. The authors claim to have gained more than 60% improvement in the distorted range image using their technique. However this method is too computationally intensive with the filter size as same as the size of the image, and the PSF model is still plausibly defined.

1.3.3 Structural Deformation Measurements

Measuring devices such as total station, CCD digital and video cameras, terrestrial laser scanners and GPS receivers are most commonly used for structural deformations measurements either in laboratory or real world test sites. Lin et al. (2009) uses digital video camera and electronic distance measurement device capable of automatic 3D measurement by scanning mechanism to investigate the dynamic behaviour of as-built membrane roof structures. Other examples of the use of photogrammetric methods for detecting deformations include Jauregui et al. (2002), Whiteman et al. (2002), Wiggenhagen (1997), Fraser and Riedel (2000) and Niederost and Maas (1997). The use of the terrestrial laser scanners for deformation measurements are presented in Ronnholm et al. (2009), Lovas et al. (2008), Gordon and Lichti (2007), Park and Lee (2007) and Tsakiri et al. (2006).

The following three papers are reviewed further due to their relevance to the proposed use of the 3D range cameras for the deformation studies. Gordon and Lichti (2007) comprehensively studied the application of the terrestrial laser scanners for precise structural deformation of timber and concrete beams. They have demonstrated the viability of the coarse resolution laser scanners for use in structural deformation measurements using dense point clouds. A detailed physical model of the beam deflection is described. Fundamentally, beam deflection is a problem of solving the linear differential equations. Further mathematical simplification of the differential equations of a simply supported loaded beam constrained with the boundary conditions of the beam deflection results in a low order polynomial function. Hence the beam deflection problem is a simple problem of curve fitting where unknown coefficients are solved using a constrained least squares adjustment.

Park and Lee (2007) also investigated the usability of the terrestrial laser scanners for health monitoring of the structures in buildings or bridges for the purpose of safety and serviceability. The choice of TLS is advantageous over other deformation monitoring devices such as linear variable differential transducers and GPS antenna because TLS allows measurements of entire surface of the structures unlike the point based measurements of the other devices.

Thus TLS provides accurate surface deformation model which facilitates better understanding of the health of the structural members and connections. They perform similar indoor beam deflection experiment like Gordon and Lichti (2007), but using an I-shaped steel beam simply supported at two ends. Like the first paper, the point-clouds of the deformed beam are fitted with a low order polynomial from which the vertical displacement is computed and compared to LVDT measurements. They reported that the TLS deflection estimations are within 1.6 % of the LVDT measurements and the strain component is also in close agreement with the measurements from the long gage fibre optic sensors.

Ronnholm et al. (2009) compares four different sensors for deformation measurements. A terrestrial laser scanner, an off-the-shelf digital camera, a total station and a dial gauges were used for measuring deformations of the simply supported concrete T- and rectangular-section beams under different load conditions. The deflection measurements were computed point wise and also by fitting low order polynomial using the measured points from all the sensors. For the laser scanner, an additional surface based component was used to compute the deflection of the beams. The deflection measurements of a total station, camera and laser scanner were compared to the more precise dial gauge measurements. They reported that deflection measurements of all the sensors were agreeable within 0.5 mm. Thus concluding that the laser scanners are viable technology to replace or compliment other measuring devices for use in the structural deformation measurements in buildings and bridges.

These three papers exclusively prove that the laser scanners could be deployed for the structural deformation measurements. However, the laser scanners are bulky and very expensive. Additionally, the TLS is a scanning device that collects data in horizontal and vertical increments thus only reliable for static scene capture. The dynamic scene measurement is important in structural deformation measurements in order to profile dynamic response of the beams under stress, thus enable the complete understanding of the characteristics of the structural members and their connections. Therefore there is a need for relatively inexpensive imaging device which can measure both static and dynamic scenes for structural deformation application. Only 3D range cameras which are the state-of-the-art range imaging technology fulfills such a need.

1.4 Research Objectives

The first objective of this thesis deals with the geometric modelling of the 3D range camera, where the method of self-calibration encompassing both lens distortions and the rangefinder errors is implemented either in an integrated approach or in a two-step photogrammetric

adjustment. A large number of model parameters are involved in the self-calibration, which causes ambiguity in the definition of the calibration model. This ambiguity necessitates a search for a viable method of model identification. An AIC method is proposed to qualitatively select the best model amongst many candidate models in order to solve the problem of over-parameterization. Additionally, the scene-dependent scattering artefact, which causes amplitude and range biases is studied elaborately using a simple two-planar objects experiment. The geometric modelling component has the following objectives:

- To propose the use of AIC method for model identification in the self-calibrating bundle adjustment
- To compare one step self-calibration method and the two step photogrammetric adjustment for calibrating the 3D range cameras
- To characterize the scattering artefact of the time-of-flight cameras specifically for the SR3000 and SR4000 SwissRanger cameras.
- To design and conduct exhaustive experimentation on the scattering phenomenon.
- To empirically model the scattering effect of the range cameras through analytical curve-fitting methods.
- To use empirical scattering compensation model to compensate for the scattering affected image for a two planar surfaces scattering scene.

The second objective of this thesis deals with the application of the 3D range camera for the structural deformation measurements in a laboratory test site. Especially, the SR4000 range camera is used for investigating the use of the range camera for precise engineering applications such as for the structural deformation measurements. The use of the SR4000 is conducive for high-precision metric applications because it is less prone to the scene-dependent scattering errors, unlike the earlier generation SR3000 range camera which is very susceptible to scattering artefact. As far as the author is concerned, there has been no publications of any work until now that deals with measuring beam deflection using the 3D range cameras. This component has the following objectives.

- To design an experiment for the structural deformation measurement in a laboratory test field.
- To develop an automatic point-cloud processing methods for analysing structural deformation scenes.

- To quantify the beam deflections due to the external loading using static scene analysis.
- To develop a methodology for the beam deflection measurements for the static deformation scenes which can be used for the processing of the dynamic scenes in future projects.

1.5 Outline

Chapter 2 deals with the background information of the 3D range camera which has been exclusively used for all the experiments conducted in this research. It includes description of the time-of-flight principle of the range imaging cameras and the method of CCD/CMOS demodulation process. Further a comparison between the 3D range imaging system and the conventional 3D stereo-vision system is discussed. This chapter ends with a short review of geometric and radiometric systematic errors of the range cameras followed by brief assessment of the three widely used range cameras.

Chapter 3 discusses the calibration of the 3D range cameras. An AIC method of model identification is proposed to solve the problem of over-parameterization in the self-calibration bundle adjustment. The integrated self-calibration method incorporates the geometric models of the standard digital camera calibration model and the rangefinder error models. Further, both one-step self calibration and two-step photogrammetric adjustment for calibrating 3D range cameras have been exclusively studied and presented. The calibration process is crucial for any sensors where the raw measurements are affected by the unmodelled systematic distortions. Mainly, the range observations of the 3D range cameras are significantly affected by systematic error components which needed to be modelled using either a physical or empirical models. An empirical high-order polynomial range correction model was used to correct for the range bias for the scattering experiments as only range information is crucial for scattering scene analysis. On the other hand for the structural deformation analysis, the one-step self-calibration parameters were used to calibrate the 3D coordinates in order to measure an accurate 3D scenes in object space.

Chapter 4 exclusively deals with the scattering phenomenon observed in the 3D range cameras which affects the range measurements significantly. The scattering artefact is caused by multiple internal reflections occurring inside the camera system when a light from the foreground objects arrives at the camera earlier than the light from the background objects, thereby attenuating the late-arrival signals. Since this phenomenon is highly scene-dependent a general physical correction model is difficult to realize. So only a simple two planar-objects experiment has been conducted to study and quantify the scattering induced

range and amplitude biases for both the SR3000 and the SR4000 range cameras. Further, an analytical spline compensation model based on the two-planar objects experimental scene is proposed to rectify for the range distortions due to the scattering artefact.

Chapter 5 looks into the use of the 3D range camera in measuring the deflection of structural members under external loading conditions. An in-house laboratory test field is set up to conduct the deformation test using concrete beam with and without the steel-reinforced polymer sheets. Only the SR4000 range camera is used for structural deformation measurements because this particular range camera has high SNR and is very resistant to the scene-dependent errors thus meeting the sensibility of the deformation analysis. A differencing method was used to compute the deflection values at a given measurement epoch. That is the deflection measurement at subsequent epochs are subtracted from the deflection measurement at the zero load state. So even if the systematic biases exists, the first difference method ensures that the biases are nullified. This is true only if the measurement biases at different loading epochs are same as the bias for the zero load state, which is explicitly assumed. The range camera measurements are compared to the measurements of the terrestrial laser scanner because the later technology has been well adopted for measuring the beam deflections.

Chapter 6 presents concluding remarks and recommendations for future tasks.

Chapter 2

Background: 3D Range Camera

The SR3000 and SR4000 are third- and fourth- generation ToF miniature cameras produced by MESA in Switzerland, whereas the PMD Camcube 3.0 is the recent range camera produced by PMDTec in Germany. These range cameras provide both range and intensity images achieved by a complex design of CCD/CMOS pixel technology. Unlike laser scanners, they do not require mechanical motors to scan the scene to obtain spatial and intensity information. Every pixel, a so called smart lock-in pixel, is designed to measure range and intensity of the objects simultaneously from the radio-frequency modulated near-infrared (NIR) signals transmitted by the camera and backscattered by the surrounding objects. The range measurement is based on the principle of the continuous wave time-of-flight method.

Sections 2.1 and 2.2 describe the time-of-flight principle and the demodulation process of the lock-in-pixel technology of the range camera. Section 2.3 describes two different methods of computing the phase, amplitude and intensity offset of the modulated returned signal using phase-shift method. Section 2.4 discusses some integral aspects of the range camera ranging from the active light source system to the systematic effects observed in the measuring device. Section 2.5 presents the differences between the conventional 3D stereo-vision system and the recent 3D range camera system. Finally, the differences of the three different range camera systems are presented in tabular form in Section 2.6.

2.1 Time-of-Flight Principle

Range sensors are mainly based on interferometry, triangulation or time-of-flight mechanisms (Lange, 2000). Interferometry and triangulation techniques are mostly confined to near-field ranging applications whereas most medium and long range 3D sensors are based on the ToF

principle. It is possible to measure the absolute distance if the time delay or the phase-shift can be measured accurately as the speed of the light is precisely known. Three different variations of ToF exist, which are pulsed-based, continuous wave and pseudo-noise method. Pulsed modulation is the most common ToF system where highly accurate timing device is used to measure the two way time-of-flight of the pulsed light. The common drawback of the pulsed system is that it requires short pulses with extremely rapid rise and fall times in order to achieve high range resolution. Even the laser scanners which are the common optical devices that produce short pulses with high optical power suffer from low repetition rates, and thus are not able to be used for capturing moving objects.

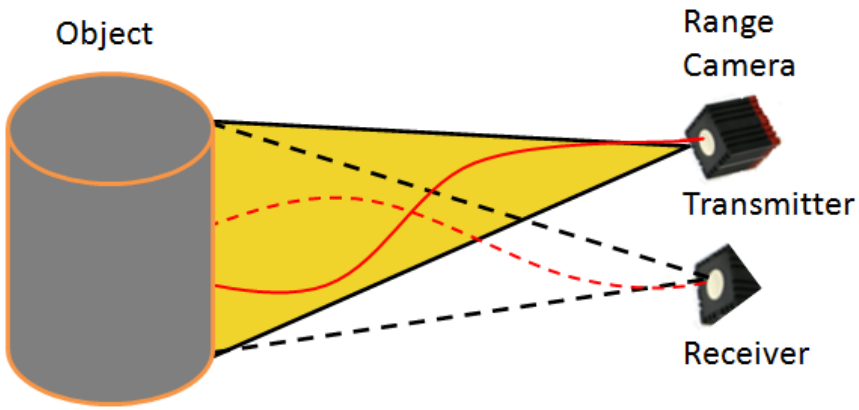

FIGURE 2.1: Principle of continuous-wave time-of-flight measurement

The RIM cameras are based on the continuous wave time-of-flight principle with alternative modulation, demodulation and detection method (Lange, 2000). In CW modulation, the phase shift of the transmitted and received signals is measured rather than the time of transmission of the signal directly. The emitted light is reflected by the objects in the scene and travels back to the camera, where the returning RF-modulated signal is demodulated by each pixel of the image sensor, producing a per-pixel range and intensity measurements. Figure 2.1 shows the schematic representation of continuous-wave ToF principle of the 3D range camera.

2.2 CCD/CMOS Demodulation Pixel Technology

A non-scanning 3D ToF sensor requires an array of specialized pixels known as demodulation pixels which are capable of measuring the phase and amplitude of the modulated signal as well as the background brightness. These pixels are based on CMOS active pixel sensor

(APS) architecture fabricated with CCD technology. The CCD option facilitates a noise-free photon detection, whereas the CMOS circuitry ease the readout process of the demodulation sensor (Oggier et al., 2004). The integration of CCD and CMOS technologies makes use of dual advantages: random pixel access due to CMOS APS which enable to set the region of interest (ROI) within the sensor frame; and noise-free addition of optically generated electrons plus directed transportation and storage of the optical electrons into defined storage sites in the semiconductor due to CCD principle (Oggier et al., 2004).

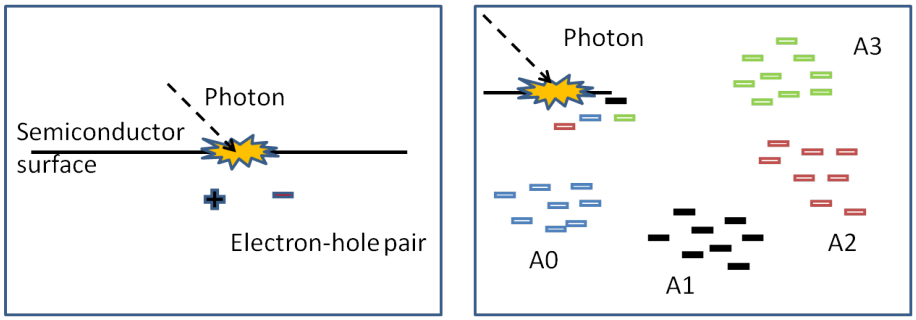

(a) Generation of electron-hole pair

(b) Fast separation of charges

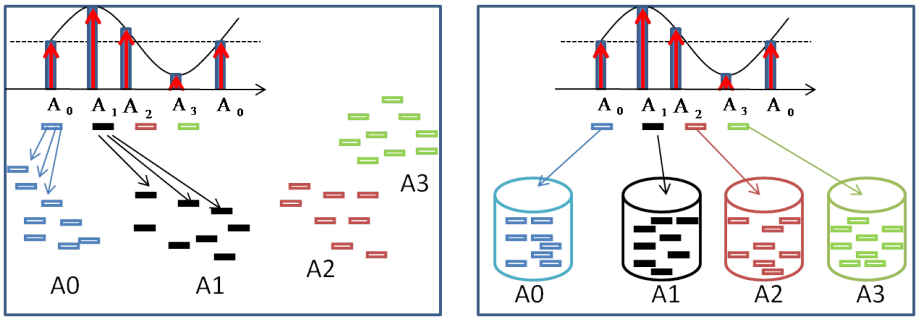

(c) Repeated and accurate addition of charges

(d) Storage of charges separately

FIGURE 2.2: Demodulation process

These lock-in CCD/CMOS pixels compute the time-of-flight distance of the object from the camera by synchronously sampling an optically modulated sinusoidal signal as described in Section 2.3. In order to achieve such demodulation, each pixel has to perform four important tasks - conversion of photons into electrons, a fast separation of charge, a repeated addition of noise-free optically generated electrons, and storage of the optical electrons in the pixel (Lange and Seitz, 2001). These four tasks of the pixels is realized by CCD/CMOS integration which is schematically represented in Figure 2.2.

Firstly, the detector converts the impinged photons into electron-hole pairs. The performance of this conversion is determined by the quantum efficiency of the semiconductor and the optical fill factor of the pixels. Quantum efficiency (QE) is defined as the percentage of photons impinging on the surface that will produce an electron-hole pair whereas the optical fill factor is the ratio of the light sensitive area to the total pixel area. Secondly, the optically generated electro-hole pairs have to be separated and transported to defined sites within each pixel quickly. This shutter mechanism of the pixel is dependent on the demodulation contrast of the pixel which is defined as the ratio of the demodulated amplitude to the intensity offset of the received signal according to Equation 2.1.

$$C_{demodulation} = \frac{A}{B} \tag{2.1}$$

Thirdly, the pixel has to perform repeated addition of noise-free signal charges accumulated per modulation period so that the total charge within an integration time can be used for demodulating into phase and amplitude information of the scene. It is important to note that for a 20MHz modulation frequency corresponding to modulation period of 50 ns, only a few photons impinge on the surface of the detector which produce a few electrons, typically even less than one electron per modulation period (Oggier et al., 2004). Therefore, it is necessary to add charges repeatedly over many modulation periods in order to obtain credible 3D information from the modulated optical signal. Fourthly, the repeated additions of the charges within each pixel have to be done correctly for all the sampling points thus enabling faster and efficient read-out process and demodulation of the signal.

2.3 Continuous Wave Phase-shift Measurement: Demodulation and Sampling Process

Unlike pulsed-based ToF where high precision clocks are required, the phase-shift measurement employs a more complex and integrated sensor design for signal processing (Lange, 2000). The camera emits an amplitude modulated signal and the transmitted signal undergoes modulation in phase and intensity due to interaction with the target scene. The phase modulation is caused by the distance of the target from the range camera. The reflected signal from the scene is received by the camera sensor via a centrally located aperture focused through an optical lens system. Each pixel in the sensor board has a unique ability to

demodulate the returned signal into amplitude and range component. Two different methods of measuring the amplitude, phase and intensity offsets are described in the following sections.

2.3.1 Cross-correlation Method

The demodulation of the received signal is achieved by correlating it with the original modulated signal by using a cross-correlation method. The received modulated signal, s(t) and the original modulated signal, g(t) are used to compute the cross-correlation function c(τ) at a given phase location using Equation 2.2.

$$c(\tau) = s(t) \otimes g(t) = \frac{A}{2} \cdot \cos(\varphi + \omega\tau) \tag{2.2}$$

where,

$s(t) = 1 + \mathrm{A} \cdot \cos(\omega t - \varphi)$, $g(t) = \cos(\omega t)$, A = amplitude of the modulated signal and φ = phase of the signal

The correlation function is computed at four sample locations ($\omega_{\tau_0} = 0°$, $\omega_{\tau_1} = 90°$, $\omega_{\tau_2} = 180°$, $\omega_{\tau_3} = 270°$) with equal length, Δt per modulation period, T ($1/\lambda_{mod}$). Figure 2.3 shows the modulated sinusoidal signal sampled at four locations per modulation period.

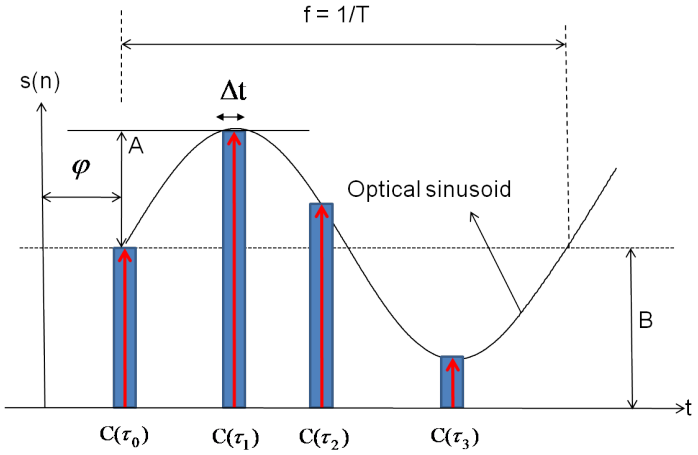

FIGURE 2.3: Cross-correlation method

As the received signal also contain some background light, the correlation function is simply modified by adding an offset value, B as given in Equation 2.3.

$$\left.\begin{aligned} C(\tau_0) = c(\tau_0) + B = \frac{A}{2} \cdot \cos(\varphi) + B \\ C(\tau_1) = c(\tau_1) + B = -\frac{A}{2} \cdot \sin(\varphi) + B \\ C(\tau_2) = c(\tau_2) + B = -\frac{A}{2} \cdot \cos(\varphi) + B \\ C(\tau_3) = c(\tau_3) + B = \frac{A}{2} \cdot \sin(\varphi) + B \end{aligned}\right\} \tag{2.3}$$

The amplitude (A), phase-shift (φ) and intensity offset (B) are calculated as given in Equations 2.4, 2.5 and 2.6 respectively.

$$A = \frac{\sqrt{[C(\tau_0) - C(\tau_2)]^2 + [C(\tau_1) - C(\tau_3)]^2}}{2} \tag{2.4}$$

$$\varphi = atan\left[\frac{C(\tau_0) - C(\tau_2)}{C(\tau_1) - C(\tau_3)}\right] \tag{2.5}$$

$$B = \frac{C(\tau_0) + C(\tau_1) + C(\tau_2) + C(\tau_3)}{4} \tag{2.6}$$

The amplitude is a measure of the depth resolution achieved and it is also used to obtain the grayscale image by multiplying it with the square of the distance (as the illumination decreases as a square of the distance) and correcting for the unevenness of the LEDs illumination over the field of view. The intensity offset determines the saturation level of the sensor and provides the 2D intensity image.

2.3.2 DFT Method

The DFT method can be used to compute the phase-shift measurement parameters by sampling the modulated sinusoidal signal with a sampling function (Lange, 2000). A sampling of the signal refers to convolving the input signal with an impulse or sampling function. In the context of the periodic signal, the DFT can be used to calculate the phase and the amplitude of the base frequency and its harmonics. For N sampling points, DFT can only determine $\frac{N}{2} - 1$ frequency components. As only four sampling points are used in the case of the range camera, DFT can determine one frequency component i.e. base frequency, without any harmonics. Such selectivity of only one discrete frequency is a well known property of CCD lock-in amplifiers, therefore the demodulation pixels are also known as lock-in pixels (Lange and Seitz, 2001).

The time domain form of the received modulated signal with background offset is defined by a raised cosine function as given in Equation 2.7 which can also be expressed as a complex signal in a frequency domain as shown in Equation 2.8

$$s(t) = A \cdot \cos(2\pi f_o t - \varphi) + B \tag{2.7}$$

$$S(f) = \left[\frac{A}{2}\delta(f\text{-}f_o) + \frac{A}{2}\delta(f\text{+}f_o)\right] e^{i\varphi f} + B\delta(f) \tag{2.8}$$

where t and f are the time and frequency in time domain and frequency domain respectively for the continuous signal, and the δ is the delta or impulse function.

The DFT and inverse DFT (IDFT) of the signal, s(t) is given by Equations 2.9 and 2.10 respectively

$$S(\nu) = \frac{1}{N}\sum_{\tau=0}^{N-1} s(\tau) e^{i\frac{2\pi\nu\tau}{N}}. \tag{2.9}$$

$$s(\tau) = \sum_{\nu=0}^{N-1} S(\nu) e^{i\frac{2\pi\nu\tau}{N}}. \tag{2.10}$$

where τ and ν are the sampling interval in time domain and frequency domain for the discrete case. Equivalently, Equation 2.9 can be expressed as a complex sinusoid as shown in Equation 2.11.

$$S(\nu) = \frac{1}{N}\left[\sum_{\tau=0}^{N-1} s(\tau)\cos\left(2\pi\tau\frac{\nu}{N}\right) + i\sum_{\tau=0}^{N-1} s(\tau)\sin\left(-2\pi\tau\frac{\nu}{N}\right)\right] \tag{2.11}$$

The magnitude of the ν^{th} coefficient of the discrete signal (M_ν) is equal to the square root of the sum of squares of the real and imaginary parts of the complex signal of Equation 2.11, and corresponding amplitude of the harmonic component (A_ν) is equal to twice its magnitude as shown in Equation 2.13. The offset B which is measured at $\nu = 0$ is given by Equation 2.14. The phase of the signal is equal to the arc tangent of the ratio of the imaginary and real parts of the complex signal as given in Equation 2.15.

$$M_\nu = \frac{1}{N}\sqrt{\left[\sum_{\tau=0}^{N-1} s(\tau)\cos\left(2\pi\tau\frac{\nu}{N}\right)\right]^2 + \left[\sum_{\tau=0}^{N-1} s(\tau)\sin\left(-2\pi\tau\frac{\nu}{N}\right)\right]^2} \tag{2.12}$$

$$A_\nu = 2 \cdot M_\nu = \frac{2}{N}\sqrt{\left[\sum_{\tau=0}^{N-1} s(\tau)\cos\left(2\pi\tau\frac{\nu}{N}\right)\right]^2 + \left[\sum_{\tau=0}^{N-1} s(\tau)\sin\left(-2\pi\tau\frac{\nu}{N}\right)\right]^2} \tag{2.13}$$

$$B = A_{\nu=0} = \frac{1}{N}\sum_{\tau=0}^{N-1} s(\tau) \tag{2.14}$$

$$\varphi(\nu) = atan\left[-\frac{\sum_{\tau=0}^{N-1} s(\tau)\sin\left(2\pi\tau\frac{\nu}{N}\right)}{\sum_{\tau=0}^{N-1} s(\tau)\cos\left(-2\pi\tau\frac{\nu}{N}\right)}\right] \tag{2.15}$$

A generic version of above equations for the phase, amplitude and intensity offset of the modulated sinusoidal signal can be rewritten in the form of harmonic coefficients of the four sampling points with equal interval of Δt as follows,

$$A = \frac{\eta}{\Delta t \cdot sin(\eta)}\frac{\sqrt{[A_3 - A_1]^2 + [A_2 - A_0]^2}}{2} \tag{2.16}$$

$$\varphi = atan\left[\frac{A_3 - A_1}{A_2 - A_0}\right] \tag{2.17}$$

$$B = \frac{A_0 + A_1 + A_2 + A_3}{4 \cdot \Delta t} \tag{2.18}$$

where $\eta = \pi\Delta t/T$, T is the modulation period and $\frac{\eta}{\Delta t \cdot sin(\eta)}$ is the attenuation factor that dampens the measured amplitude to about 90% of the real amplitude. Figure 2.4 illustrates the parameters involved in measuring amplitude, phase and offset of the sinusoidal signal using DFT method.

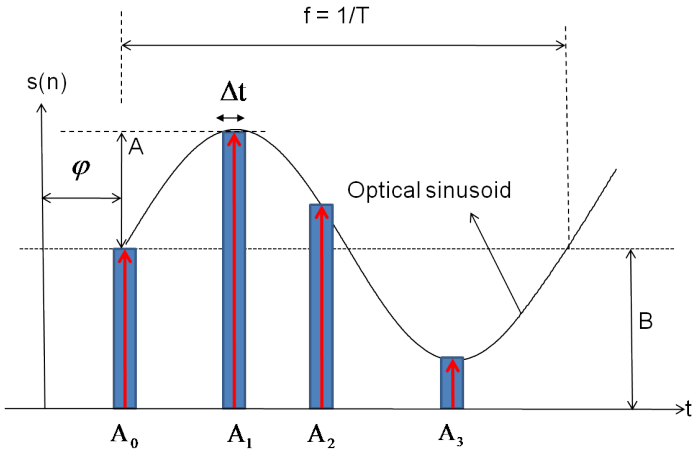

FIGURE 2.4: DFT method

The integration of charges at four phase locations per modulation period can be accumulated over many modulation periods within an integration time (Spirig and Seitz, 1995).

This means that the resultant signal charge over many modulation periods is equal to the product of the number of modulation periods and the charge packet per modulation period. The integration of charges over many modulation period helps to increase the SNR of the system by sharpening the sensitivity of the sensor, lowering the sensitivity to spurious frequency components and increasing the signal strength (Lange, 2000). Thus this integration process also enable to measure even the low intensity signals reflected from dimly illuminated surfaces.

The phase delay of the received signal is directly proportional to the distance of the object from the camera, which is computed according to Equation 2.19

$$R = R_u \cdot \frac{\varphi}{2 \cdot \pi}, \qquad R_u = \frac{c}{2 \cdot f_{mod}} \tag{2.19}$$

where R_u is the unambiguous range, f_{mod} is the modulation frequency and c is the speed of light. The unambiguous range of the camera is determined by the modulation frequency of the signal used. For a 20MHz modulation frequency, the non-ambiguous range is 7.5 metres. In the SR3000 and SR4000, the calculation of a meaningful range value from the 16 bit integer-valued range output is done as given in Equation 2.20. The division of the 16-bit unsigned integer range value, ρ_{int}, by four is needed since its two least significant bits must be ignored. Doing so scales the integer distance into the range 0 to 0x3FFF (16383). It can be easily accomplished with the right bitwise shift operator.

$$\rho = \frac{2^{-2}\rho_{int}}{0X3FFF} \cdot \frac{2}{f_{mod}} \tag{2.20}$$

2.4 Some Other Important Aspects of the RIM Cameras

Some other important aspects of the range cameras are briefly described in the following sections which will provide insight into the active lighting facility of the range camera, theoretical limit of the range measurement accuracy, effects of the background lighting and integration time, pinhole projective coordinate system, and random and systematic errors effecting the ranging accuracy.

2.4.1 Light Source

Three-dimensional range cameras are active sensors that emit its own light by using arrays of LEDs (light emitting diodes). LEDs are inexpensive emitter and the emitted light from such device can be modulated up to 100MHz with high linearity. The LEDs are available in wide range of wavelengths from blue light to mid-infra red spectrum with an optical power ranging up to few hundred milliwatts, which is sufficient for the phase-based ToF ranging system. Additionally the low power of LEDs facilitates safe operation of the camera as the emitted light power is within the eye safety limits. LEDs are only limited by the total power available, and therefore they are not used for pulse-based system where modulation is required up to several GHz.

The performance of the emitter is a function of its modulation frequency, the modulation contrast and the total power output. With higher modulation frequencies, the accuracy of the depth resolution is increased but at the cost of a shorter unambiguous range measurements. The visible and the invisible infra-red spectrum are the most suitable wavelengths for the silicon based sensors because of the high spectral sensitivity of the silicon detectors for these wavelengths. The quantum efficiency of the semiconductor is high for the visible and the infra-red spectrum. The range cameras which are based on the solid-state silicon sensors use wavelength in the near infra-red spectrum as it is more safe for human environments than the colour wavelengths. The carrier wavelength is modulated with a frequency up to few tens of megahertz. For instance, the SR4000 range cameras emits light with wavelength of 850 nm which can be modulated with different frequencies of 29/30/31 MHz for the standard FOV range camera and 14.5/15/15.5 MHz for the wide FOV range camera.

2.4.2 Range Resolution

The 3D ToF camera suffers from internal system noises such as photon shot noise, photon-charge conversion noise and quantization noise thereby limiting the range resolution of the system (Lange, 2000). Of the three noises, only shot noise cannot be reduced or eliminated either by software or hardware improvement. Thus photon shot noise is the ultimate theoretical range resolution limit. Shot noise is statistically defined as the Poisson distribution of the photons impinging on the photoactive area of the pixel. The standard deviation of the photon noise is equal to square root of the average number of photons or photoelectrons generated. The magnitude of the shot-noise increases with the intensity of the light, so the SNR of the system is very large for higher illumination levels. This indicates that

by increasing the power of transmitted light alone will not improve the performance of the system.

Oggier et al. (2004) have shown that the range error of the photon-shot noise is within 1 cm even for the impinging photon with the minimum amount of energy required for the generation of the electrons for reliable measurement of the range to the objects from the sensor. Their result indicates that the range accuracy of within 1 cm is achievable using the range cameras as the photon-shot noise is the theoretical limit for the range resolution of the RIM cameras. With more photons, even better performance of the range camera is realized. In accordance to Lange (2000), the range resolution limited by the shot-noise is given by Equation 2.21

$$\delta R = \frac{R_u}{\sqrt{8}} \cdot \frac{\sqrt{B}}{2 \cdot A} \tag{2.21}$$

where R_u is the unambiguous range, B is the intensity offset i.e. the number of photoelectrons per pixel and sampling points generated by the background light and the mean value of the modulated light reflected from the actual scene, and A is the demodulation amplitude i.e. the number of photoelectrons per pixel per sampling point generated by the modulated light source. The intensity offset is dependent on the background illumination as well as the RF-modulated light. Background illumination can be avoided by imaging in the dark or it can be reduced by using spectral filters that only transmit the modulated light, whereas the modulation amplitude is dependent on the total emitted optical power of the modulated light source, the modulation depth, demodulation contrast of the pixel, the distance to the target and the reflectivity of the target. It is important to note that the optical power density of the light decreases with increasing distance to the target, hence the range accuracy is greater for the small distance measurement which is crucial for application in navigation where short distance measurements are desired (Lange, 2000).

However Equation 2.21 is not the practical limit of the range resolution. There are other internal noise sources such as thermal noise, reset noise, 1/f noise, and quantization noise that need to be considered. By adding pseudo-electrons N_p to the offset B in Equation 2.21, a better measure of the range resolution is obtained as given in Equation 2.22. As per Equation 2.22, a distance confidence map can be obtained from the range camera.

$$\delta R = \frac{R_u}{\sqrt{8}} \cdot \frac{\sqrt{B + N_p}}{2 \cdot A} \tag{2.22}$$

2.4.3 Background Illumination

One big problem of a range camera is the effect of the background light thereby limiting its use for only indoor environments. This problem has not been able to be solved even for the SR4000 range camera which is evident from the fact sheet recommending only to be used for indoor purposes (MESA, 2010). Background light causes addition of electrons causing biased range measurement, or otherwise lead to the saturation of the pixels. The pixel saturation is curtailed to a certain extent by using an optical bandpass filter in the camera mount, which allows only the central wavelength of the emitted light to enter the lens. Yet, the background illumination still reaches two orders of magnitude higher than the actual signal (Buttgen et al., 2005). Other method such as modified circuitry has been implemented in the SR3000 to suppress the background light.

A pixel-level background light suppression method is implemented in the SR4000 to decrease the effect of the background illumination on the accuracy of the range measurements (MESA, 2010). Theoretically, it can be considered that the background illumination adds equal amount of electrons to all the samples. Which means that the differencing of A3-A1 and A2-A0 for the phase-shift measurement nullify the effect of additional electrons due to the background light (Buttgen et al., 2005). They have shown that the the accuracy of the real distance measurements closely agrees with the theoretical expectation predicted based on the physical limitation of the photon shot noise. Their experiment further suggests that the use of enhanced in-pixel background light suppression method has curtailed the problem of background lighting even while the background illuminations exceeds well over 150 times that of the actual signal strength.

However, as described in Section 2.4.2 the photon shot noise increases with the increase of photon-generated electrons thereby degrading the SNR of the system which leads to lower accuracy for the range measurements. The background light does add more photons to the process which lead to degrading the SNR of the system. That is why it is recommended to use the range cameras within indoor environments in order to obtain the best performance of the 3D range measurement system.

2.4.4 Integration Time

One important parameter of a RIM camera is the integration time. The integration time is the time allowed to integrate the photon-generated electrons per modulation period over many cycles. It typically ranges from 0 to 255 (8-bit integer value) which corresponds to 0.2 to 52.1 ms for the SR3000 and 0.2 to 28.4 ms for the SR4000 range cameras. It

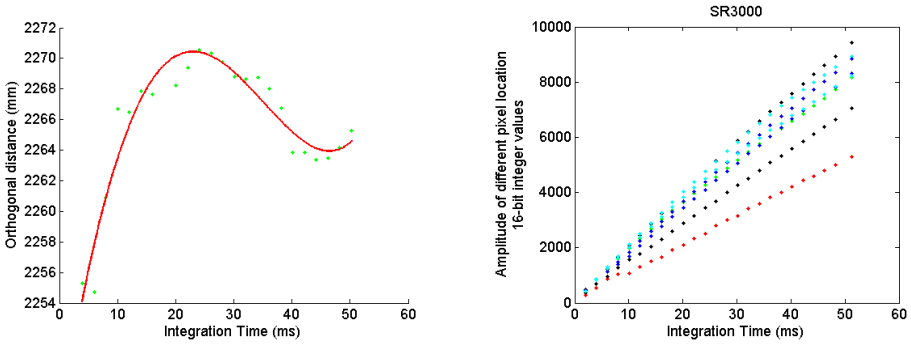

FIGURE 2.5: SR3000: Range (R) and amplitude (L) bias as a function of the integration time

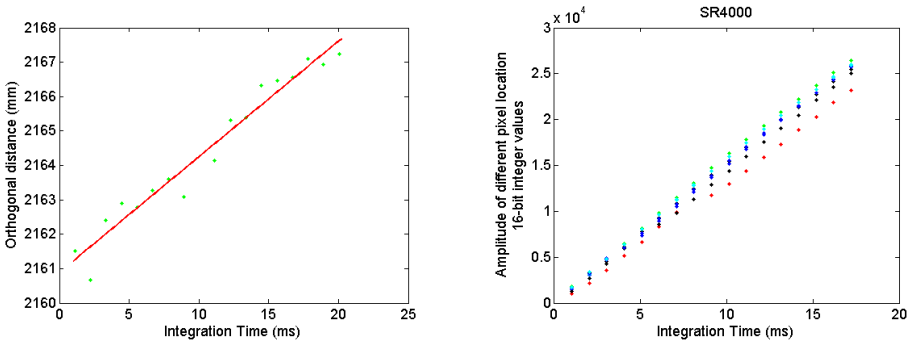

FIGURE 2.6: SR4000: Range (R) and amplitude (L) bias as a function of the integration time

is crucial to use the right integration time for a scene as a lower integration time would compromise the accuracy of the distance measurement while a higher integration time will lead to saturation of the pixels due to the increase in the amplitude of the measured signal. Generally, a higher integration time is recommended to be used to achieve a high distance measurement accuracy. On the other hand, a higher integration time will also decrease the data capture rate as the time of acquisition increases with the integration time. For dynamic scene capture, a lower integration time may have to be used depending on the nature of the dynamics.

A range and amplitude bias as a function of the integration time is mapped in Figures 2.5 and 2.6. A surface wall of uniform colour was imaged using SR3000 and SR4000 at different integration times. For the SR3000, the full integration time range was used as the saturation of pixels was not observed at the given distance for the imaged target. For the SR4000, a

shorter distance to the wall was used to accommodate the larger FOV of the camera and only integration time up to 180 16-bit integer values was used to avoid pixel saturation. The left images of both the figures show a plot of the orthogonal distance measured from the camera's perspective to the fitted plane against the integration times, whereas the right images show the plot of the amplitude values of the six different pixel locations (chosen at a few locations diagonally away from the center of the image towards the periphery of the image) against the integration times.

It can be clearly seen in both the figures that the range and amplitude monotonically increase with the integration time. However, the range measurement for the SR3000 increases rather erratically as a function of the integration times as oppose to a proportional increase observed in the case of the SR4000. Further, the decrease in amplitude from the central pixel towards the peripheral pixels for the SR3000 range camera is greater than the SR4000 camera which indicates that the power distribution of the LEDs in the SR4000 is more uniformly distributed across the field-of-view of the camera.

2.4.5 3D Coordinate Measurement

The output of the RIM cameras consists of many variables such as amplitude, intensity, range map, distance confidence map and Cartesian coordinates – X, Y and Z. It is important to know how the projected object coordinates are computed for metric use. Typically for a 3D measurement system, the X, Y and Z coordinates of the object points are computed based on a simple pinhole camera model as given in Figure 2.7 (Kahlmann, 2007).

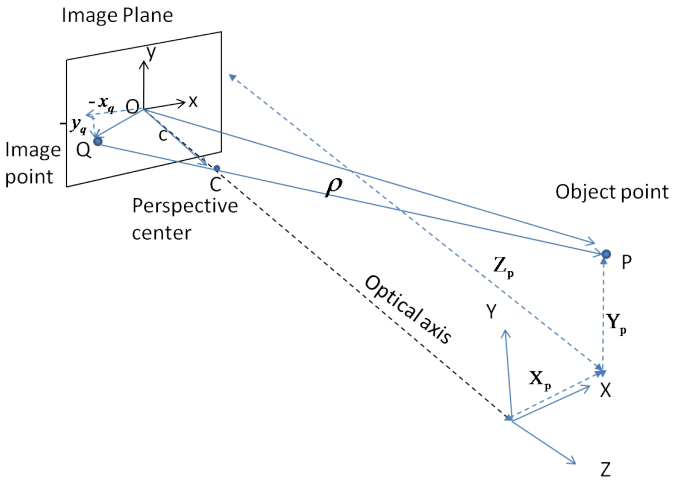

FIGURE 2.7: Pinhole Camera Model

The important parameter for the 3D system is the range value which is measured independently at every pixel in the sensor frame. The origin of image plane coordinate system, O is the intersection of the optical axis and the image plane which is commonly referred to as the principal point or image center. C $(0, 0, c)$ is the perspective center which is commonly assumed to be a focal length away from the origin of the image plane. The focal length is assumed to be equal to the principal distance (c). The inverted image of the point P (X_p,Y_p,Z_p) is formed on the image plane at Q $(-x_q, -y_q, 0)$. The image plane coordinate system is defined by x- and y- axes with z values equal to zero for all the image points. The object space coordinate system is defined by X-, Y- and Z-axes, with X- and Y- coordinate axes are assumed coincident with the image plane system and Z-axis runs along the optical axis. The measured range (ρ) is the distance from the image point (Q) towards the corresponding object (P) in the 3D space. Based on the pinhole camera model, the object point coordinates of P is calculated using known image coordinates of Q in accordance to Equation 2.23. The derivation of Equation 2.23 is as follows.

$$\vec{QC} = \vec{OC} - \vec{OQ}$$

$$\vec{QC} = \begin{bmatrix} 0 \\ 0 \\ c \end{bmatrix} - \begin{bmatrix} -x_q \\ -y_q \\ 0 \end{bmatrix} = \begin{bmatrix} x_q \\ y_q \\ c \end{bmatrix}$$

and

$$\vec{QP} = \left|\vec{QP}\right| \cdot \vec{QC} \cdot \frac{1}{\left|\vec{QC}\right|} = \rho \cdot \vec{QC} \cdot \frac{1}{\left|\vec{QC}\right|}$$

since $$\vec{OP} = \vec{OQ} + \vec{QP}$$

$$\Rightarrow \begin{bmatrix} X_p \\ Y_p \\ Z_p \end{bmatrix} = \begin{bmatrix} -x_q \\ -y_q \\ 0 \end{bmatrix} + \begin{bmatrix} x_q \\ y_q \\ c \end{bmatrix} \cdot \frac{\rho}{\sqrt{{x_q}^2 + {y_q}^2 + c^2}} \tag{2.23}$$

The mapping from 3D (object scene) to 2D coordinates (image) described by a pinhole camera is a perspective projection followed by a 180° rotation in the image plane. For a digital system the pixels are read in a different order so that it becomes rotated.

2.4.6 Systematic Errors

There are two kinds of systematic errors that affects the range camera observations, namely scene-independent and scene-dependent errors. The scene-independent errors of the the 3D range cameras range from standard camera distortions like radial and decentring distortions to more complicated range biases due to range-finder errors, which comprises of range-finder offset, scale factor error, cyclic and clock skew errors (Lichti, 2008). The scene-dependent errors which varies from one imaging scene to the other are due to scattering artefact (Mure-Dubois and Hugli, 2007), incidence angle error (Karel et al., 2007) and multipath effect (Guomundsson et al., 2007).

2.5 Comparison of the Stereo Vision and 3D Time-of-Flight Systems

The traditional photogrammetric method of 3D image acquisition is achieved by the principle of stereo vision where at least two cameras are used to capture a common object. This system of depth measurement is still in use for many ranging applications because it obtains high resolution range image. However, a stereo vision system is limited due to small FOV and the problem of correspondence (Hussmann et al., 2008). The FOV of the SV system refers to the overlapping region of the two images where range image can be obtained. A matching of point correspondences in an SV system is tedious and most times it is difficult to find the point correspondences for homogeneous surfaces.

With the advent of the 3D ToF system such as SwissRanger and PMD range cameras where 3D measurements are obtained directly, the problem of depth detection is nearing to an end. It has sparked renewed interests in the research community for various range-based applications using ToF imaging systems. Stereo vision systems may soon become outdated. However the RIM cameras are still in infancy as the system hardware and functionalities are not fully developed to provide desired range accuracy for most range-based applications. Nevertheless, the outlook of RIM cameras is promising with the rapid development of the semiconductor technology. With miniaturization of the semiconductor, the RIM cameras will only become more effective and accurate.

A common SV system consists of two cameras aligned in such a way to capture an object with desired overlap. A corresponding point in the two images is matched and intersected to obtain the depth information by the method of triangulation. Figure 2.8 (left) shows the SV method of obtaining the range information. For complex scenes, the processing may take

longer or even fail to find correspondences. The process of stereo measurement is tedious and time consuming. In the case of 3D ToF system, there is no requirement to search for point correspondences and the FOV of the range camera is larger than the SV system. Figure 2.8 (right) shows the schematic representation of ToF system where range measurement is achieved by measuring the two-way time-of-flight of the signal directly. The process of range measurement is instantaneous.

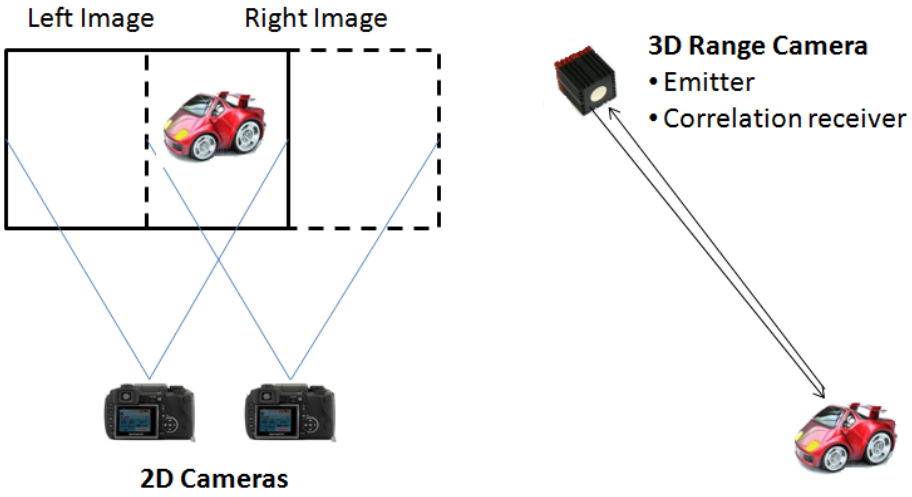

FIGURE 2.8: Principle of SV (Left) and 3D ToF (Right) systems

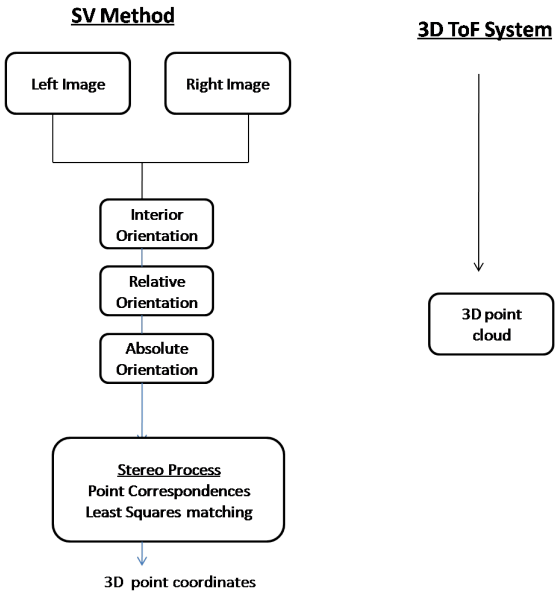

FIGURE 2.9: Processing steps of SV (Left) and 3D ToF (Right) systems

A comparison of the two systems for obtaining the 3D coordinates of the object is shown in Figure 2.9. Despite the fact that ToF system can obtain 3D point coordinates of the object instantaneously, yet the accuracy of the range measurement is lower than the SV system due to scene-dependent systematic biases. As for now, the stereo vision system is more developed than the 3D ToF system.

2.6 Comparison of RIM Cameras

Two cameras used in this project are SwissRanger SR3000 and SR4000 which are developed by Centre Suisse d'Electronique et de Microtechnique SA (CSEM) in Zurich. The SR4000 is the recent fourth generation range camera which has replaced the SR3000 model. Another range camera with similar working principle as the SwissRanger's is produced by PMDTec in Germany. PMD Camcube 3.0 is the recent generation of PMD models, which are photonic mixing device built completely in a CMOS process. The comparison of few characteristics of these cameras are provided in Table 2.1.

TABLE 2.1: Specifications of three RIM cameras

	SR4000	**SR3000**	**PMD Camcube 3.0**
Pixel Array Size	176 (h) x 144 (v)	176 (h) x 144 (v)	200 (h) x 200 (v)
Field of View	43.6° x 34.6°	47.5° x 39.6°	40° x 40°
Focal length	10 mm	8 mm	12, 8 mm
Illumination Wavelength	850nm	850nm	870nm
Modulation Frequency	29, 30, 31 MHz or 14.5, 15, 15.5 MHz	20MHz	20MHz
Measurement Range	0.3 to 5.0 meters	7.5m	0.3 to 7 m
Distance accuracy	$\pm 1cm$	1 % of range	
Absolute accuracy	± 10mm @ 100% reflectivity		
Repeatability	< 5mm within 2 m range		< 3mm at 4m distance, 75 % reflectivity
Frame rate	Up to 54 fps	25 fps	40 fps at 200x200 pixels, 60 fps at 176x144 pixels, 80 fps at 160x120 pixels
Communication interface	USB 2.0	USB 2.0	USB 2.0
Power consumption	0.8 A @ 12V	12 V	12V ± 10%
Camera Housing	65x65x68 (mm^3)	50x67x42.3 (mm^3)	60x60x60 (mm^3)
Illumination unit	24 LEDs	55 LEDs	LEDs

The image resolution of the PMD camera of 200 by 200 pixels is higher than the Swissranger cameras with 144 (rows) by 176 (columns) pixels. All three devices have a similar carrier frequency at NIR wavelength. The SR3000 and the PMD Camcube 3.0 operates at 20 MHz modulation frequency which provides an unambiguous range measurements up to 7.5 metres whereas the SR4000 provides two sets of modulation frequency groups with first set (29, 30 and 31 MHz) can measure unambiguous range up to 5 metres and the second set (14.5, 15 and 15.5 MHz) can measure up to 10 metres. However the longer the distance measured, the lower is the accuracy of the range measurements as described in Section 2.4.2.

While the SR4000 provides measurement precision and accuracy explicitly, the other two only states a general sense of measurement precision. For the SR3000, the accuracy of the range measurements is 1 percent of the range which means that the expected accuracy of the range measured at 4 m is about 4 cm. For the PMD Camcube, the expected measurement precision is about 3 mm at a distance of 4 m with a target having reflectivity greater than 75%. For the SR4000, the range measurement precision is less than 5 mm for a distance within 2 m. The distance accuracy of the SR4000 is ± 1 cm within the unambiguous range and the absolute accuracy achievable is also about ± 1 cm with 100% reflectivity. The SR3000, PMD Camcube and SR4000 can capture dynamic scenes with a maximum frame rate of 24, 60 and 54 frames per seconds (fps) respectively. Additionally, the PMD Camcube can capture up to 80 fps with image resolution of 160 by 120 pixels thus enabling 3D scene capture of higher dynamics than the other two devices. They all have a USB 2.0 and ethernet communication interfaces.

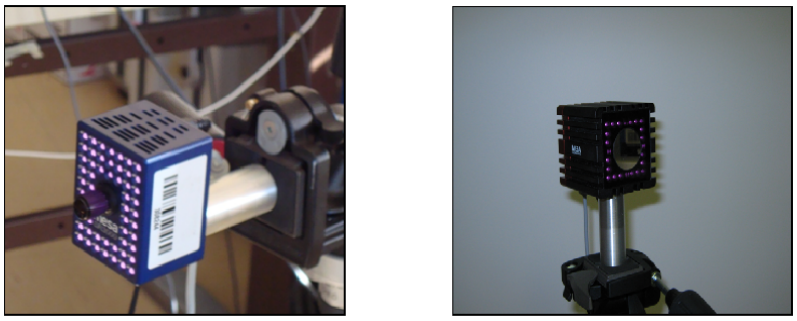

FIGURE 2.10: SR 3000 (Left) and SR4000 (Right) range cameras

Figure 2.10 shows the SR3000 and SR4000 range cameras exclusively used in this project.

2.7 Summary

The RIM cameras are the state-of-the art imaging technology where 3D information of the scene is captured without the use of any rotating system like used in the terrestrial laser scanners. Such a technology is possible because of the miniaturization of the semiconductor technology and the evolvement of the CCD/CMOS processes that can be implemented independently for each pixel where range to the target is measured by a phase-shift time-of-flight method. Such camera can not only capture static scene but is also able to capture dynamic scene at video rate which has been not possible with the laser scanning system. With such range measurement system, it is possible to achieve various static and dynamic range-based applications which were not possible with the 2D imaging system or at least it proves to be a simple and direct alternative to using the conventional stereo-vision system for 3D imaging applications. However these cameras suffers from significant geometric and radiometric distortions due to the presence of noises and scene-dependent errors thereby limiting their use so far to only for low accuracy metric applications. Nonetheless the future of the RIM cameras looks brighter due to further progress in the semiconductor technology and ever increasing research interest with respect to these cameras. Few calibration methods are available for dealing with the geometric errors of the range cameras which will be explored in further details exclusively in Chapter 3.

Chapter 3

Calibration of the Range Camera

The 3D range cameras suffer from geometric and radiometric distortions. Most importantly, the range observations of the range cameras are biased by the scene-dependent errors which makes it difficult to calibrate the rangefinder system. Often the range measurement biases are plausibly modelled using a rangefinder error model or often simply modelled by using an empirically based high-order polynomial or splines.

Sections 3.1 to 3.3 describe the theoretical and mathematical estimation aspects of the the self-calibration free-network bundle adjustment with respect to the RIM cameras. Section 3.4 describes the optimal design of the calibration experiment and the extraction of the target points using intensity based edge detection algorithm respectively. A range camera calibration can be achieved either in one-step self-calibration approach or two-step photogrammetric adjustment which is described in Section 3.5 and 3.6 respectively. In a self-calibration adjustment, there are a large number of model parameters involved which leads to the problem of model identification. Section 3.5.1 proposes the use of Akaike Information Criterion to resolve the ambiguity caused by over-parametrization.

3.1 Mathematical Models

The collinearity equation is the basis of the functional model used in the self-calibration of the range cameras where the parameters comprise the interior orientation parameters (IOPs), the exterior orientation parameters (EOPs), and the coordinates of the 3D features in the object space. The self-calibration bundle adjustment is achieved by a free network adjustment which solves the problem of network datum deficiency minimally. The stochastic

model is defined based on the Gauss-Markov assumption of no correlation between the observation errors having a mean zero and a unit a-priori variance factor.

3.1.1 Functional Model

The collinearity equations are modified to accommodate the systematic error terms of the camera lens as defined by the standard camera lens systematic errors of the digital cameras (Fraser, 1997). The range equation augmented with the rangefinder error terms defines the range observation equation. Thus for every point of observation, there are two collinearity observation equations (Equations 3.1 and 3.2) and one range observation equation (Equation 3.3)

$$x_{ij} = x_{p_j} - c_j \frac{U_{ij}}{W_{ij}} + \Delta x \tag{3.1}$$

$$y_{ij} = y_{p_j} - c_j \frac{V_{ij}}{W_{ij}} + \Delta y \tag{3.2}$$

$$\rho_{ij} = \sqrt{[X_i - X_j^\circ]^2 + [Y_i - Y_j^\circ]^2 + [Z_i - Z_j^\circ]^2} + \Delta\rho \tag{3.3}$$

where,

$[x, y, \rho]_{ij}$ are the observables

$[x_p, y_p, c]_j$ are the basic IOP parameters

$U_{ij} = r_{11}(X_i - X_j^\circ) + r_{21}(Y_i - Y_j^\circ) + r_{31}(Z_i - Z_j^\circ)$

$V_{ij} = r_{12}(X_i - X_j^\circ) + r_{22}(Y_i - Y_j^\circ) + r_{32}(Z_i - Z_j^\circ)$

$W_{ij} = r_{13}(X_i - X_j^\circ) + r_{23}(Y_i - Y_j^\circ) + r_{33}(Z_i - Z_j^\circ)$

$\Delta x, \Delta y, \Delta\rho$ are the systematic error terms

r's are the elements of the rotation matrix, R

$[\omega, \phi, \kappa, X^\circ, Y^\circ, Z^\circ]_j$ are the EOPs

$$R = \begin{pmatrix} cos(\phi)cos(\kappa) & -cos(\phi)sin(\kappa) & sin(\phi) \\ cos(\omega)sin(\kappa) + sin(\omega)sin(\phi)cos(\kappa) & cos(\omega)cos(\kappa) - sin(\omega)sin(\phi)sin(\kappa) & -sin(\omega)cos(\phi) \\ sin(\omega)sin(\kappa) - cos(\omega)sin(\phi)cos(\kappa) & sin(\omega)cos(\kappa) + cos(\omega)sin(\phi)sin(\kappa) & cos(\omega)cos(\phi) \end{pmatrix}$$

The systematic error terms for x and y are described by the standard camera model parameters consisting of radial, decentring and affinity distortion terms in accordance to Equation 3.4.

$$\left.\begin{aligned}\Delta x &= \overline{x}(K_1 r^2 + K_2 r^4 + K_3 r^6) + P_1(r^2 + 2\overline{x}^2) + 2P_2\overline{xy} + A_1\overline{x} + A_2\overline{y} \\ \Delta y &= \overline{y}(K_1 r^2 + K_2 r^4 + K_3 r^6) + P_2(r^2 + 2\overline{y}^2) + 2P_1\overline{xy}\end{aligned}\right\} \tag{3.4}$$

where,

$\overline{x} = x_{ij} - x_{p_j}$

$\overline{y} = y_{ij} - y_{p_j}$

$r^2 = \overline{x}^2 + \overline{y}^2$

(K_1, K_2, K_3) are the radial lens distortion terms

(P_1, P_2) are the decentring distortion terms

(A_1, A_2) are the affinity terms

The range bias term, $\Delta\rho$ consists of offset term (D_0), scale error(D_1), cyclic components $(D_2, .., D_7)$, clock-skew errors (E_1 and E_2) and empirical terms $(E_3, ..., E_{11})$ as defined in Equation 3.5.

$$\Delta\rho = D_0 + D_1\rho + \sum_{k=0}^{3}\left[D_{2k}\sin\left(\frac{2^k\pi}{R_u}\rho\right) + D_{2k+1}\cos\left(\frac{2^k\pi}{R_u}\rho\right)\right] + E_1\overline{x} + E_2\overline{y} + E_3 r + E_4 r^2 + \sum_{m=2}^{3}\sum_{n=0}^{m} E_{3m+n-1}\overline{x}^{m-n}\overline{y}^{n} \tag{3.5}$$

Scale is implicitly defined by the range observations. However spatial distances can be used as an additional observations to determine the scale error (D_1) explicitly. For every distance observation between the two points (d_{pq}), one equation is obtained as in Equation 3.6

$$d_{pq} = \sqrt{[X_q - X_p]^2 + [Y_q - Y_p]^2 + [Z_q - Z_p]^2} \tag{3.6}$$

where p and q are the two different points.

In all, there are 26 additional model parameters involved in the functional model defined above. Most of the terms are pertaining to the systematic bias of the range observations. However the significance of majority of model parameters are negligible in the context of this camera system as observed by Lichti (2008), so only few of the model parameters will be considered in this project which shall be determined empirically or statistically using the AIC method.

3.1.2 Stochastic Model

Based on the Gauss-Markov theorem, the observation errors are assumed to be uncorrelated with a mean of zero and a-priori variance factor greater than zero and less than infinity (Luhmann et al., 2006). An a-priori variance factor (σ_0^2) of 1 for the observational errors is implicitly assumed. The stochastic model is explicitly defined by the measurement precision of the observations. For instance, in the self-calibration experiment performed in this project the precision of the edge detection and the ellipse fitting method is used as the standard deviation of the image coordinates observations. A more detailed description of the edge detection and ellipse fitting measurement technique is given in Section 3.4.2. For the range observations, the manufacturer's quote of the range measurement precision is used. Hence, the error of observation is given by $\hat{e} \sim (0, \sigma_0^2 \sum^{-1})$, with the variance-covariance matrix ($\sum$) defined as:

$$\sum = \begin{pmatrix} \sigma_{1,1}^2 & 0 & \cdots & 0 \\ 0 & \sigma_{2,2}^2 & \cdots & 0 \\ \vdots & \vdots & \ddots & \vdots \\ 0 & 0 & \cdots & \sigma_{n,n} \end{pmatrix}$$

where $\sigma_{i,j}$ are the standard deviations of the observations and n is the number of observations. This error model is implemented in the estimation method using a weighted parametric least squares adjustment. Thus the noise of the range camera system is stochastically modelled in the least squares estimation method which is described in Section 3.3.

3.2 Free Network Adjustment

The datum of a network is the minimum number of parameters needed to define the position, orientation and scale of a network within the given space. For instance, in a 3D network

there are seven parameters needed to define a datum (three for position, three for orientation and the scale factor). The datum problem arises because the image point co-ordinates are arbitrarily defined without any information about the object space datum. The image point co-ordinates are basically direction observations which only defines general shape of the object network but not scale, position or orientation. So there is a datum defect in the network which causes singularity in the normal equations matrix. Mathematically, the rank deficiency of the normal matrix, N is given by Equation 3.7, where u and d are the number of unknown parameters and datum defect respectively.

$$rank(N) = u - d \tag{3.7}$$

Generally in a photogrammetric adjustment, the datum problem is solved by using fixed or weighted control points. The minimally constrained adjustment is achieved by providing minimum amount of datum information in the adjustment: such as for the 3D adjustment, two full control point and one coordinate of the third point is used. Extra datum information results into an over constrained adjustment, which is undesirable for the close-range photogrammetric network adjustment.

There is another method of achieving minimal constraint adjustment without using the control points where only image information and the intersection condition are used to reconstruct the bundles of rays from multi-image orientation (Luhmann et al., 2006). There are no control points required to define the datum of the network explicitly. Such a method of adjustment is called free-network adjustment. In a free-network adjustment the datum defect is removed by simply transforming the arbitrarily defined network of the image point cloud to object space network using a similarity or Helmert transformation which is given in Equation 3.8. As the initial point coordinates of the targets form a network of point cloud, the similarity transformation will neither change the shape of the point cloud, nor affect its geometry. This method is implemented in self-calibrating bundle adjustment by imposing a set of inner constraints on the object point parameters only. For the range camera adjustment where additional range observations are available, the datum defect is six as the scale parameter is defined implicitly by the range observation.

$$\begin{bmatrix} X_i \\ Y_i \\ Z_i \end{bmatrix} = R \begin{bmatrix} X_i^0 \\ Y_i^0 \\ Z_i^0 \end{bmatrix} + \begin{bmatrix} T_x \\ T_y \\ T_z \end{bmatrix} \tag{3.8}$$

By taking the partial derivatives of the linearized form of the Equation 3.8 with respect to six parameters, an inner constraint design matrix for the object points is obtained, i.e.

$$G^T_{o_{(d,u_o)}} = \begin{pmatrix} 1 & 0 & 0 & 1 & 0 & 0 & \dots \\ 0 & 1 & 0 & 0 & 1 & 0 & \dots \\ 0 & 0 & 1 & 0 & 0 & 1 & \dots \\ 0 & Z^0_1 & -Y^0_1 & 0 & -Z^0_2 & -Y^0_2 & \dots \\ -Z^0_1 & 0 & X^0_1 & -Z^0_2 & 0 & X^0_2 & \dots \\ Y^0_1 & -X^0_1 & 0 & Y^0_2 & -X^0_2 & 0 & \dots \end{pmatrix}$$

where d is the number of datum defects and u_o is the number of unknown object points. This constraint is imposed on all the object points such that there is no change to the network position and orientation.

The EOP inner constraint design matrix is given below, where u_e is the number of EOP parameters.

$$G^T_{e_{(d,u_e)}} = \begin{pmatrix} 1 & 0 & 0 & 0 & 0 & 0 & \dots \\ 0 & 1 & 0 & 0 & 0 & 0 & \dots \\ 0 & 0 & 1 & 0 & 0 & 0 & \dots \\ 0 & Z^0_{c_1} & -Y^0_{c_1} & 1 & 0 & 0 & \dots \\ -Z^0_{c_1} & 0 & X^0_{c_1} & sin(\omega)^0_1 tan(\phi)^0_1 & cos(\omega)^0_1 & -sin(\omega)^0_1 sec(\phi)^0_1 & \dots \\ Y^0_{c_1} & -X^o_{c_1} & 0 & -cos(\omega)^0_1 tan(\phi)^0_1 & sin(\omega)^0_1 & cos(\omega)^0_1 sec(\phi)^0_1 & \dots \end{pmatrix}$$

So the full inner constraint takes the form as shown in Equation 3.9

$$\begin{bmatrix} G^T_{e_{(d,u_e)}} & G^T_{o_{(d,u_o)}} \end{bmatrix} \begin{bmatrix} \hat{\delta}_e \\ \hat{\delta}_o \end{bmatrix} = 0 \tag{3.9}$$

where $\hat{\delta}_e$ and $\hat{\delta}_o$ are the correction vectors for the EOP and object point parameters.

3.3 Parametric Least Squares Adjustment

The parametric least squares functional model is shown in Equation 3.10

$$l = f(x) + \hat{e} \tag{3.10}$$

where l is the vector of n observations, f is the vector of m functions, x is the vector of u unknowns and $\hat{e}$ is error of the observations. The linearised form of the least squares observation equation (3.10) is given in Equation 3.11,

$$A_{n,u}\hat{\delta}_{u,1} + \hat{w}_{n,1} = \hat{r}_{n,1} \tag{3.11}$$

which can be equivalently represented in hyper-matrix form as shown in Equation 3.12 by including all the observations that are described in Section 3.1.1

$$\begin{bmatrix} A_{xe} & A_{xa} & A_{xo} \\ A_{ye} & A_{ya} & A_{yo} \\ A_{\rho e} & A_{\rho a} & A_{\rho o} \\ 0 & 0 & A_{do} \end{bmatrix} \begin{bmatrix} \hat{\delta}_e \\ \hat{\delta}_a \\ \hat{\delta}_o \end{bmatrix} + \begin{bmatrix} \hat{w}_x \\ \hat{w}_y \\ \hat{w}_\rho \\ \hat{w}_d \end{bmatrix} = \begin{bmatrix} \hat{r}_x \\ \hat{r}_y \\ \hat{r}_\rho \\ \hat{r}_d \end{bmatrix} \tag{3.12}$$

where A_{ij} is the Jacobian matrix of partial derivatives taken for i observation group w.r.t the j set of unknown parameters, $\hat{w}_i$ is the misclosure vector of the observations and the $\hat{r}_i$ is the residual vector of the observations, and δ_e, δ_a and δ_o are the correction vectors for the EOPs, IOPs and object points parameters respectively.

Subject to the full inner constraints, the least squares objective function is obtained by combining Equations 3.11 and 3.9 and is given in Equation 3.13

$$\phi = \hat{r}^T P \hat{r} + 2\hat{k}^T G^T \hat{\delta} \tag{3.13}$$

where P is the weight matrix ($\sum^{-1}$) and $\hat{k}$ is the Lagrange multipliers. Lagrange multipliers are commonly used as a strategy to find the solution of the optimization problem in the presence of constraints by introducing the same number of Lagrange variables as the number of constraints involved in the system.

In the case of a free-network adjustment where the datum defect is solved by imposing inner constraints on the EOP and object points parameters, the pseudo-inverse (which is most commonly referred as the Moore-Penrose inverse) of the rank deficient normal matrix is sought rather than the Cayley inverse (Kuang, 1996). Equation 3.14 shows the solution vector for the bordered normal equations

$$\begin{bmatrix} \hat{\delta} \\ \hat{k} \end{bmatrix} = \begin{bmatrix} (A^T P A)^+ & G(G^T G)^{-1} \\ (G^T G)^{-1} G^T & 0 \end{bmatrix} \begin{bmatrix} A^T P \hat{w} \\ 0 \end{bmatrix} \tag{3.14}$$

where $(A^T PA)^+$ is the pseudo-inverse. The pseudo-inverse can be computed in many ways: by singular value decomposition (SVD) method (Gill and King, 2004); by eigenvalue-eigenvector decomposition method (Layton, 1997); and directly or indirectly as given in Equations 3.15 and 3.16 respectively (Kuang, 1996).

$$\begin{aligned}(A^T PA)^+ &= (A^T PA + GG^T)^{-1} - G(G^T GG^T G)^{-1} G^T \\ &= (A^T PA + GG^T)^{-1} - G(G^T G)^{-1}(G^T G)^{-1} G^T \end{aligned} \tag{3.15}$$

$$(A^T PA)^+ = (A^T PA + GG^T)^{-1} A^T PA (A^T PA + GG^T)^{-1} \tag{3.16}$$

Additionally, two important points is noted below for optimal processing of the least squares method in a free-network adjustment.

- Reduction of the network co-ordinates to the centroid as given in Equation 3.17

$$\left.\begin{aligned}\overline{X}_i^o &= X_i^o - \overline{X} \\ \overline{Y}_i^o &= Y_i^o - \overline{Y} \\ \overline{Z}_i^o &= Z_i^o - \overline{Z}\end{aligned}\right\} \tag{3.17}$$

  where $(\overline{X}, \overline{Y}, \overline{Z})$ are centroid of the approximate coordinates of m datum points calculated as follows.

  $\overline{X} = \frac{1}{m}\sum_{i=1}^{m} X_i^o$, $\overline{Y} = \frac{1}{m}\sum_{i=1}^{m} Y_i^o$ and $\overline{Z} = \frac{1}{m}\sum_{i=1}^{m} Z_i^o$

- The bordered normal equations matrix is not positive-definite, so the use of Cholesky decomposition is not possible but the Crout reduction method (Kraus, 1987) can be used to solve the system of linear equations.

3.4 Calibration Experiment

3.4.1 Data Collection

Optimal design of the calibration experiment is necessary to accurately obtain the calibration parameters from the bundle adjustment. Some factors of considerations for the quality assurance of the calibration experiment are test field design, image configuration, target design and data redundancy.

An indoor planar test field, a large surface wall of dimension 6.40 m by 4.57 m inside a squash court in the Kinesiology complex was used for this experiment. High contrast circular targets (white circle on black background) as proposed by (Lichti et al., 2010) were rigidly fixed on the surface wall. The circular targets with three different diameters (45, 150 and 280 mm) were used so that the targets at different distances can be resolved unambiguously to facilitate the intensity based extraction of the target coordinates. Figure 3.1 shows the test field of the calibration experiment.

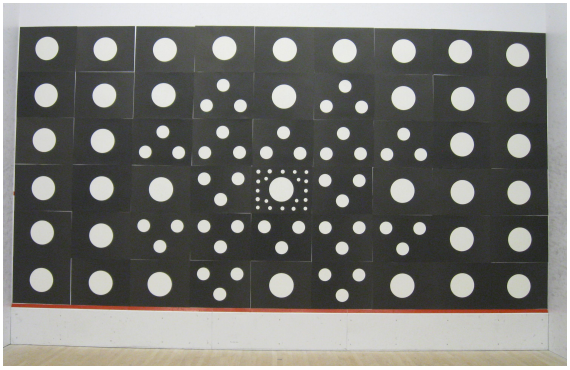

FIGURE 3.1: Target Field

In order to avoid scattering and multipath induced errors, the imaging network is carefully framed only to image the planar test field. There were two sets of images captured – the normal and the convergent images. Normal images were captured from locations perpendicular to the centre of the target field whereas the convergent images were captured from either side of the normal line. The use of convergent images in a calibration network assist in de-correlation of the IOPs from the EOPs (Lichti et al., 2010). The imaging geometry of the calibration experiment is shown in Figure 3.2. In total there were 27 images for the SR3000 network and 20 images for the SR4000 network. Additionally, 4 extra images for the SR3000 and 6 for the SR4000 were captured for evaluating the accuracy of the self-calibration, which are also shown in Figure 3.2.

The camera's optical axis corresponds to the Y-axis of the local coordinate system, which is aligned perpendicular to the planar target field. At each camera location for the convergent imaging, two images were captured: a landscape image with $\kappa = 0^\circ$ and a portrait image with $\kappa = 90^\circ$, where κ is the rotation angle about the Z-axis. It was not completely possible to avoid imaging the floor for the portrait format imaging from the convergent imaging locations as the targets at the lower part of the test field were quite close to the floor. So only the image point co-ordinate observations made from these images were included in the self-calibration adjustment. The convergent images were captured from 1 m up to the limit

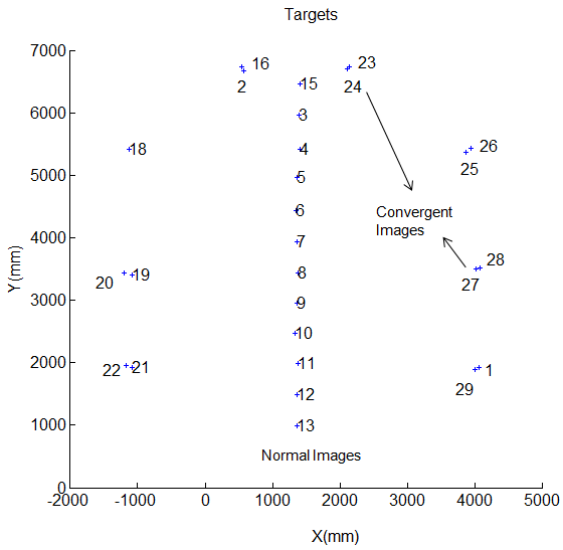

FIGURE 3.2: Geometry of the imaging network

of the side wall at a 0.5 m interval. As for the normal imaging, the images were acquired every 0.5 m starting at 1.0 m from the target field to 6.5 m.

The selection of integration time is crucial for data acquisition because of proportional dependency between the accuracy of the range measurements and the saturation of the pixels with the integration time. For the SR3000, pixel saturation is not observed even at the highest integration time because of the built-in bandpass filter in the optical system of the camera which cuts off the background lighting. However, in the SR4000 the saturation of the pixels is observed for high reflective targets at short distance for high integration times. A high integration time is desired to achieve high accuracy range measurements, but the saturation of the pixels needs to be avoided thus requiring to compromise between pixel saturation and the achievable accuracy of the range measurements. An integration time of 51.2 ms and 4.3 ms was used for the SR3000 and SR4000 range cameras respectively. Furthermore, both the cameras were warmed up for about an hour prior to the experimentation in order to attain optimal operating internal temperature of the device.

3.4.2 Target Extraction

Automatic extraction of image space coordinates of the targets is necessary to determine the 3D coordinates precisely from the range and amplitude images. The measurement of the image co-ordinates of the target is performed in three steps (Lichti et al., 2010). Firstly, the edge of the ellipse (circular targets are projected as ellipse in a perspective projection)

is identified in the amplitude imagery using the Canny edge detection operator (Gonzalez and Woods, 2008). Secondly, a least squares ellipse fitting is used to determine the center of the ellipse, which is then corrected for biases due to ellipse eccentricity (Ahn et al., 1999). Thirdly, the range measurement of the center of the target is computed from those of the four neighbouring pixels using bi-linear interpolation method. MATLAB edge detection and ellipse fitting algorithm written by Denis Rouzaud (Rouzaud, 2008) which is based on the above steps was used to obtain the target coordinates as shown in Figures 3.3(a) and 3.3(b).

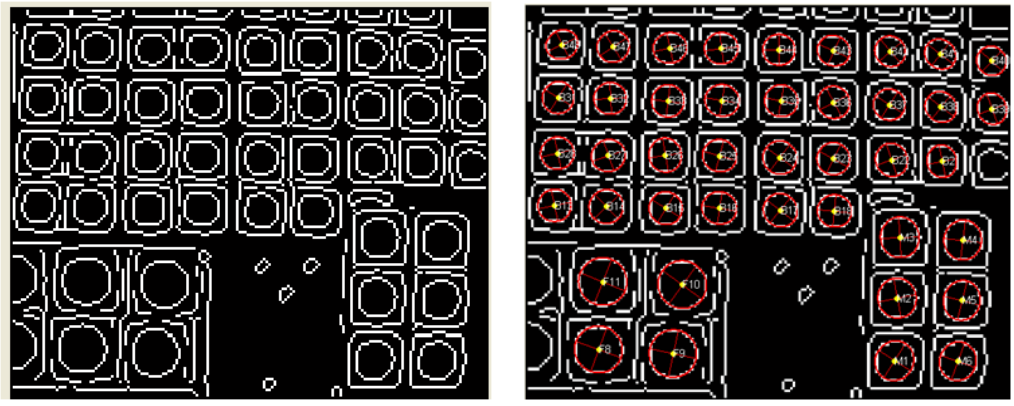

(a) Edge detection (b) Ellipse fitting

FIGURE 3.3: Extraction of the target coordinates

3.5 Integrated Bundle Adjustment

An integrated self-calibration bundle adjustment of the range camera has been proposed by Lichti et al. (2010), Robbins et al. (2009), Westfeld et al. (2009), Lichti (2008) and Karel (2008). For the integrated approach, one-step calibration is used to determine both standard camera calibration parameters and rangefinder systematic error terms. Such a method account for the functional dependencies between the parameters in the system concerning with different components of the measuring device. The aforementioned research has indicated the need for an integrated approach in order to accommodate the combined effects of different components involved in an imaging device. In this project, an integrated self calibration bundle adjustment approach proposed by Lichti et al. (2010) is used for calibration of the SR3000 and SR4000 range cameras. The FEMBUN program by Dr. Derek Lichit was used for the calibration of the range cameras.

3.5.1 Model Identification

Any physical laws and principles are defined through mathematical models which are expressed as a function of parameters that can be estimated using least squares (LS) or maximum likelihood estimation (MLE) methods. The math model may be too cumbersome in some cases such as in the photogrammetric self-calibration bundle adjustment, where for instance the functional model for the 3D range camera calibration is plausibly defined with twenty-six additional parameters. In such case, the fundamental problem lies in the model identification.

3.5.1.1 What is Model Identification?

Many parameters are involved in the self-calibration model, some of which may or may not define the governing principle of the range camera at a particular time of experimentation. It is a complicated process to identify the exact number of parameters that builds the structure of the model, which as of now has been primarily achieved through subjective judgement and hypothesis testing on the significance of the estimated parameters. However, such a procedure of model identification is quite inconclusive. Thus model identification is still the most daunting task in mathematical estimation.

This project proposes to use the statistical inference criterion of Akaike (1974), a statistician who proposed the well known model selection method called the Akaike Information Criterion which is based upon the principle of maximum likelihood estimation method. An AIC model consists of two parts. The first component defines the loss function of the estimated parameters given by a log likelihood term. The second component defines the penalty term defined by the number of parameters used in the model. The AIC is quite elegant in the sense that it is simple to implement and has been successfully used as statistical model fitting criteria such as from regression analysis to the autoregressive model fitting in various fields of engineering and scientific applications (Akaike, 1974; Schwarz, 1978; Blais, 1981).

3.5.1.2 Theory of AIC

The observables obtained through experimentation are a subset of a population which exhibits a unique probability density function (pdf), $f(X/\theta)$, where X is the observable and θ is the parameter (Myung, 2003). Each probability distribution is associated with a certain number of parameters involved in the system model. A set of different parameters will produce a different probability distribution. So any physical or empirical model is defined as

the family of probability density functions each with their own set of parameters. Therefore the goal of parameter estimation is to find the parameters that best describe the desired probability distribution. One way of achieving this is to seek for the value of the parameter vector that maximizes the likelihood function, $L(\theta/X)$. Often the log of likelihood, $\ln L(\theta/X)$, is used over the likelihood as the two functions are related monotonically. The parameter vector obtained by maximizing the log-likelihood function is commonly called as the Maximum Likelihood Estimate.

It has been shown by Akaike (1974) that the problem of identification is closely related to the maximum likelihood estimation because of the fact that the "MLE estimates are, under certain regularity conditions, asymptotically efficient shows that the likelihood function tends to be a quantity which is most sensitive to the small variations of the parameters around the true values". This deduction leads to the formulation of AIC model with two terms - one which is a loss function of the estimated parameters that is equivalent to the goodness of fit of the model in terms of the error variance and the other is a penalty term for the complexity of the model (Blais, 1981) as given in Equation 3.18

$$AIC = -2 \ln \frac{\hat{\theta}}{X} + 2K \tag{3.18}$$

where K is the number of model parameters and $\hat{\theta}$ is the estimated parameter.

An AIC is a criterion of fit of the model. That is, the AIC is not an indicator of the absolute correctness of the model, but only provides the relative strength among the candidate models in consideration. Increasing the number of free parameters to be estimated improves the goodness of fit, regardless of the true number of free parameters involved in generating the observations (Blais, 1981). Nevertheless, the AIC not only rewards goodness of fit but also includes a penalty that is an increasing function of the number of estimated parameters which discourages over-parameterization. The model that has the minimum AIC value is the most likely model.

The other way of seeking the value of parameter vector is by least squares estimation approach which, unlike the MLE method does not have a strong statistical basis. Nonetheless, the least squares method is practically efficient and proven equivalent to MLE estimate for the most symmetric distribution case such as the normal distribution, which is the most commonly encountered problem. Hence Equation 3.18 is reduced to 3.19 with the likelihood term of Equation 3.18 replaced by the error variance or root of the sum of squared residuals (RSS).

$$AIC = n \ln \frac{RSS}{n} + 2K \tag{3.19}$$

Although the AIC method produces a relatively optimal model in the sense of an information theoretic aspect, it is not always practical when dealing with a finite set of observations (Schwarz, 1978). Due to this complication involved in finite dimensional models, the original AIC model has been modified by many others to suit different aspects of model identification by altering the penalty term. Equations 3.20 and 3.21 show the AIC biased criterion (AIC_c) and Bayesian Information Criterion (BIC) respectively. For this project, the AIC method given by Equation 3.19 is used for model selection in self-calibration bundle adjustment of the 3D range camera because even the AIC_c method produced similar results as the AIC method.

$$AIC_c = n \ln \frac{RSS}{n} + 2K + \frac{2K(K+1)}{n-K-1} \tag{3.20}$$

$$BIC = n \ln \frac{RSS}{n} + K \ln n \tag{3.21}$$

3.5.1.3 Candidate Models and AIC computation

The huge number of parameters involved in the self-calibration model of the 3D range camera poses a problem in identifying even the candidate models comprising of finite number of likely parameters. Several combinations of parameters are grouped together to form the candidate models whose relative strength in a group is tested based on the AIC weighting method. It is impossible to test all the combinations of the model parameters, therefore, the group formation is selectively focussed on certain significant parameters. Table 3.1 and 3.2 shows the candidate models with 10 and 30 models for the SR4000 and the SR3000 range camera respectively.

TABLE 3.1: SR4000: Candidate Models

Model No	Candidate Models	No. of APs
B1	$K_1\ K_2\ D_0\ D_2\ D_3\ D_4\ D_5\ D_6\ D_7\ E_1\ E_2\ E_3\ E_4$	13
B2	$K_1\ K_2\ D_0\ D_3\ D_4\ D_5\ D_6\ D_7\ E_1\ E_2\ E_3\ E_4$	12
B3	$K_1\ K_2\ D_0\ D_3\ D_4\ D_5\ D_6\ D_7\ E_1\ E_2\ E_3$	11
B4	$K_1\ K_2\ D_0\ D_2\ D_3\ D_4\ D_5\ D_6\ D_7\ E_1\ E_2$	11
B5	$K_1\ K_2\ D_0\ D_2\ D_3\ D_4\ D_5\ D_6\ D_7$	9
B6	$K_1\ K_2\ A_1\ A_2\ P_1\ P_2\ D_0\ D_2\ E_1$	9
B7	$K_1\ K_2\ A_1\ A_2\ P_1\ P_2\ D_0$	7
B8	$K_1\ K_2\ P_1\ P_2\ D_0\ D_2\ E_1$	7
B9	$K_1\ P_1\ P_2\ E_1\ E_2$	5
B10	$K_1\ K_2\ P_1\ P_2\ D_0$	5

A special set of observation points is used for the self-calibration bundle adjustment in order to optimize the accuracy of the calibration method. This set of observation comprises of

TABLE 3.2: SR3000: Candidate Models

Model No	Candidate Models	No. of APs
A1	$K_1\ K_2\ K3\ P_1\ P_2\ A_1\ A_2\ D_0\ D_2\ D_3\ D_4\ D_5\ D_6\ D_7\ E_1\ E_2\ E_3\ E_4$	18
A2	$K_1\ K_2\ K3\ P_1\ P_2\ A_1\ A_2\ D_0\ D_2\ D_3\ D_4\ D_5\ D_6\ D_7\ E_1\ E_2$	16
A3	$K_1\ K_2\ K3\ P_1\ P_2\ A_1\ A_2\ D_0\ D_2\ D_3\ D_4\ D_5\ D_6\ D_7\ E_1\ E_3$	16
A4	$K_1\ K_2\ K3\ P_1\ P_2\ A_1\ A_2\ D_0\ D_2\ D_3\ D_4\ D_5\ D_6\ D_7\ E_2\ E_4$	16
A5	$K_1\ K_2\ K3\ P_1\ P_2\ A_1\ A_2\ D_0\ D_2\ D_3\ D_4\ D_5\ D_6\ D_7\ E_2$	15
A6	$K_1\ K_2\ D_0\ D_2\ D_3\ D_4\ D_5\ D_6\ D_7\ E_1\ E_2\ E_3\ E_4$	13
A7	$K_1\ K_2\ D_0\ D_2\ D_3\ D_4\ D_5\ D_6\ D_7\ E_1\ E_2\ E_3$	12
A8	$K_1\ K_2\ D_0\ D_2\ D_3\ D_4\ D_5\ D_6\ D_7\ E_1\ E_2\ E_4$	12
A9	$K_1\ K_2\ D_0\ D_2\ D_3\ D_4\ D_5\ D_6\ D_7\ E_1\ E_4$	11
A10	$K_1\ K_2\ D_0\ D_2\ D_3\ D_4\ D_5\ D_6\ D_7\ E_2\ E_3$	11
A11	$K_1\ K_2\ D_0\ D_2\ D_3\ D_4\ D_5\ D_6\ D_7\ E_1\ E_3$	11
A12	$K_1\ D_0\ D_2\ D_3\ D_4\ D_5\ D_6\ D_7\ E_2\ E_3$	10
A13	$K_1\ D_0\ D_2\ D_3\ D_4\ D_5\ D_6\ D_7\ E_1\ E_2$	10
A14	$K_1\ D_0\ D_3\ D_4\ D_5\ D_6\ D_7\ E_2\ E_3$	9
A15	$K_1\ K_2\ D_0\ D_4\ D_5\ D_6\ D_7\ E_2\ E_3$	9
A16	$K_1\ K_2\ D_0\ D_3\ D_5\ D_6\ D_7\ E_2\ E_3$	9
A17	$K_1\ D_0\ D_2\ D_4\ D_5\ D_6\ D_7\ E_2\ E_3$	9
A18	$K_1\ K_2\ D_0\ D_2\ D_3\ D_4\ D_5\ D_6\ D_7$	9
A19	$K_1\ D_0\ D_3\ D_5\ D_6\ D_7\ E_1\ E_2$	8
A20	$K_1\ D_0\ D_4\ D_5\ D_6\ D_7\ E_2\ E_3$	8
A21	$K_1\ D_0\ D_3\ D_4\ D_6\ D_7\ E_2\ E_3$	8
A22	$K_1\ D_0\ D_2\ D_5\ D_6\ D_7\ E_2\ E_3$	8
A23	$K_1\ K_2\ D_0\ D_3\ D_5\ D_7\ E_2\ E_3$	8
A24	$K_1\ D_0\ D_2\ D_4\ D_6\ D_7\ E_2\ E_3$	8
A25	$K_1\ D_0\ D_2\ D_5\ D_6\ D_7\ E_2\ E_3$	8
A26	$K_1\ D_0\ D_3\ D_5\ D_6\ D_7\ E_2\ E_3$	8
A27	$K_1\ D_0\ D_4\ D_6\ D_7\ E_2\ E_3$	7
A28	$K_1\ D_0\ D_3\ D_5\ D_6\ E_2\ E_3$	7
A29	$K_1\ D_0\ D_3\ D_5\ D_6\ D_7\ E_2$	7
A30	$K_1\ D_0\ D_4\ D_5\ D_6\ D_7$	6

3D coordinates (x,y and ρ) of orthogonally- oriented images and only 2D coordinates (x and y) of non-orthogonal images as per the findings of Lichti et al. (2010). Such a set of observations minimizes error due to scattering effect and incidence angle of the reflected light from the scene thus improving the accuracy of the modelling. The sum of squares of the residuals obtained from the bundle adjustment is used to compute the AIC value of each candidate models which is then used to compute Akaike weights as per Equation 3.22,

$$w_i = \frac{\exp(-0.5 * \Delta_i)}{\sum_{i=1}^{R} \exp(-0.5 * \Delta_i)} \tag{3.22}$$

where $\Delta_i = AIC_i - AIC_{min}$,the numerator term is the relative likelihood of the given model i, the denominator term is the sum of the relative likelihoods of all the candidate models, and R is the number of candidate models. The Akaike weights indicate the relative strength of the candidate model within a group. The w_i is interpreted as the probability that model i is the best model, given the data and set of the candidate models (Burnham and Anderson, 2002).

3.5.1.4 RMSE computation

In order to assess the accuracy of each model the RMSE values are computed based on the differences in coordinates of the check points obtain from the range image and the total station survey. The absolute coordinates of the target points are calculated from the range image in accordance to Equation 3.23,

$$\begin{bmatrix} X \\ Y \\ Z \end{bmatrix}_i = \frac{\rho_{ij} - \Delta\rho}{\sqrt{u_{ij}^2 + v_{ij}^2 + w_{ij}^2}} R \begin{bmatrix} u \\ v \\ w \end{bmatrix}_{ij} + \begin{bmatrix} X^o \\ Y^o \\ Z^o \end{bmatrix}_j \tag{3.23}$$

where

$$\begin{bmatrix} u \\ v \\ w \end{bmatrix}_{ij} = \begin{bmatrix} x_{ij} - x_p - \Delta x \\ y_{ij} - y_p - \Delta y \\ -c \end{bmatrix} \tag{3.24}$$

and R is the rotation matrix and the other parameters involved in the above equation is described in Section 3.1.1. The second component of the right hand side of Equation 3.23 is the EOPs of the j^{th} image which are calculated from the set of independent images by resection method using the interior orientation and additional parameters obtained from the self-calibration bundle adjustment. The independent images are the set of extra images that were captured for the purpose of accuracy assessment.

3.5.1.5 Selection of the Most Likely Model for the SR3000

The 30 candidate models shown in Table 3.2 have been used for self-calibration adjustment of the SR3000 range camera. The relative strength of every candidate model has been assessed by computing the Akaike weights from their AIC values. Plus, the RMSE of the check points are computed for all the models in consideration. Table A.2 in Appendix A shows the AIC parameters and the RMSE values for all the candidate models in the SR3000 case. For instance the Akaike weights in Table A.2 indicate that Model A12 is (0.652/0.184) = 3.5 times more likely to be the best model than the Model A26. Generally, the consensus set of candidate models include models with Akaike weights that are within 10% of the highest value. Model A12, A26 and A14 with 10, 8 and 9 APs respectively are selected as the likely models based on AIC criterion as their Akaike weights are above ten percent of

the highest value of Model A12 i.e. 0.065 (0.652 *0.1). Remaining models can be excluded from further analysis as their Akaike weights are outside the threshold.

TABLE 3.3: Estimated parameters and standard errors for SR3000

	Model A12 (in mm)		**Model A14 (in mm)**		**Model A26 (in mm)**	
Parameters	**Values**	**Std. Errors**	**Values**	**Std. Errors**	**Values**	**Std. Errors**
x_p	0.0277	0.0072	0.0274	0.0072	0.0274	0.0072
y_p	-0.0621	0.0077	-0.0624	0.0077	-0.0626	0.0077
c	8.1656	0.0086	8.1656	0.0086	8.1657	0.0086
K_1	-0.0018	0.0000373	-0.0018	0.0000372	-0.0018	0.0000372
D_0	109.1273	10.8566	88.7268	3.3883	88.6345	3.3834
D_2	-11.6723	6.0249	NA	NA	NA	NA
D_3	9.3256	2.1071	7.4271	1.8735	7.0715	1.7448
D_4	-3.2702	2.3653	0.643	1.2309	NA	NA
D_5	-23.4628	1.8482	-25.361	1.5239	-25.4994	1.5008
D_6	9.8731	1.1927	10.2775	1.1707	10.1406	1.1407
D_7	26.2166	1.1808	26.4361	1.1681	26.4083	1.1668
E_2	-4.1488	0.7363	-4.1463	0.7393	-4.1406	0.7392
E_3	4.5687	0.9556	4.5603	0.957	4.5854	0.9558

Table 3.3 shows the estimated parameters and their standard errors of the three selected models. These three models are equally valid as per the AIC model selection method. One way to solve this uncertainty is to use AIC weighting method to compute the new parameter estimates and variances (i.e., standard errors) where a contribution is made from each model according to their relative Akaike weights. Model-weighted parameter estimates are only calculated for those parameters that are included in the likely models. For the three likely models selected in this case, there are 10 unique model parameters which has to be considered. An example of computing the combined model parameter and standard error of one parameter, x_p by Akaike weighting method is illustrated in Tables 3.4 and 3.5 respectively. The weighted value of the x_p is the sum of the individual weighted values of each model(entries of the column "New Parameter Contribution"),which are obtained by multiplying their corresponding weights (w_i) and the actual parameter values (entries of the column "Actual Parameter").

TABLE 3.4: Akaike estimate of the parameter (x_p)

Model	**AIC**	$\mathbf{exp(0.5 * \Delta_i)}$	$\mathbf{w_i = \frac{exp(0.5*\Delta_i)}{\sum_{i=1}^{3} exp(0.5*\Delta_i)}}$	**Actual Parameter**	**New Parameter Contribution**
A12	-177.953	1	0.709	0.0277	0.01964
A14	-175.426	0.283	0.200	0.0274	0.00548
A26	-173.849	0.128	0.091	0.0274	0.00249
				New Value =	**0.027613**

The Model Selection Variance in Table 3.5 is the square of the difference between the combined estimated parameter (0.027613) and the least squares estimate (entries of column

TABLE 3.5: Akaike estimate of the standard errors for x_p

Model	Actual Parameter	Conditional Variance	Model Selection Variance	$\sqrt{CV + MSV}$	w_i	Unconditional Weighted Parameter
A12	0.0277	0.0072	7.63721E-09	0.00720053	0.709	0.005102989
A14	0.0274	0.0072	4.52025E-08	0.007203138	0.200	0.001442444
A26	0.0274	0.0072	4.52025E-08	0.007203138	0.091	0.000655858
					New value =	**0.007201**

TABLE 3.6: Combined estimated parameters and their standard errors for the SR3000 range camera

Model Parameters	Values (mm)	Standard Errors (mm)
x_p	0.027613	0.007201
y_p	-0.06221	0.007702
c	8.165609	0.0086
K_1	-0.00183	3.7E-005
D_0	103.1762	13.10557
D_2	-8.27212	7.312559
D_3	8.740182	2.227826
D_4	-2.18882	2.660787
D_5	-24.0284	1.966502
D_6	9.978438	1.195423
D_7	26.27801	1.180906
E_2	-4.14755	0.737169
E_3	4.568538	0.955919

"Actual Parameter"). The new standard error value is the sum of the individual weighted values contributed by each model (entries of the column "Unconditional Weighted Parameter") which are obtained by multiplying their weights (w_i) and the corresponding entries of the column "$\sqrt{CV + MSV}$". Table 3.6 shows the combined estimates of the parameters and their standard errors computed using Akaike weighting method.

3.5.1.6 Selection of the Most Likely Model for the SR4000

The 10 candidate models shown in Table 3.1 has been used for self-calibration adjustment of the SR4000 range camera. Table A.1 in Appendix A shows the AIC variables and RMSE of the check points for all the models used for the SR4000 calibration tests.

Model B8 and B6 with 7 and 9 APs respectively are selected as the most likely models based on their relative AIC value as their Akaike weights are above 10% of the minimum AIC value. Table 3.7 shows the least squares estimates of the two likely models for the SR4000 range camera. Like in the case for the SR3000, the two likely models for the SR4000 is combined using Akaike averaging method to obtain a combined estimates of the parameters

TABLE 3.7: Estimated parameters and standard errors of two likely models for the SR4000 range camera

	Model B6 (in mm)		**Model B8 (in mm)**	
Parameters	**Values**	**Std. Errors**	**Values**	**Std. Errors**
x_p	0.0651	0.0312	0.0968	0.0308
y_p	0.2324	0.0304	0.2204	0.0292
c	10.0175	0.017	10.0188	0.0124
A_1	0.000076	0.000669	NA	NA
A_2	0.001025	0.000575	NA	NA
K_1	-0.007835	0.000141	-0.00790	0.000139
K_2	-0.000273	0.000008	-0.00027	7.5E-006
P_1	0.000003	0.000145	-0.00030	0.000144
P_2	-0.000438	0.000138	-0.00033	0.000136
D_0	-18.3333	5.8234	-18.2746	5.8102
D_2	7.9651	2.9639	8.092	2.9611
E_1	1.4125	0.5102	1.5422	0.5075

TABLE 3.8: Combined estimated parameters and their standard errors for the SR4000 range camera

Model Parameters	**Values (mm)**	**Standard Errors (mm)**
x_p	0.0837	0.0346444
y_p	0.2253	0.030271
c	10.0183	0.014308
A_1	0.00003	0.000295
A_2	0.0004	0.000591
K_1	-0.0079	0.000143
K_2	-0.0003	0.000008
P_1	-0.0002	0.000206
P_2	-0.0004	0.000147
D_0	-18.2988	5.815708
D_2	8.0397	2.962911
E_1	1.4888	0.512596

and their standard errors. Table 3.8 shows the combined estimates of the parameters and their standard errors computed from the least squares estimates of the Model B6 and B8.

3.5.2 Results and Analysis

The mathematical models presented in Section 3.1 are the basis of the integrated approach. However, only few significant parameters are considered in the functional model as most of the error terms involved in the full model has been observed to be trivial. An Akaike Information Criteria has been used to select the significant parameters to avoid the problem

of over-parameterization. Based on the Akaike model selection method, three likely models are selected as the most likely models with 8, 9 and 10 APs for the SR3000. The high accuracy of these models is proven by their low RMSE values of the check points

The 10-parameters model have the highest Akaike weight and also the highest RMSE accuracy, but 9- and 8- parameters model have one and two parameters respectively less, plus RMSE accuracy is very similar to the 10-parameters model. This uncertainty is best solved by averaging the model parameter by using Akaike weights as described in Section 3.5.1.5. Thus the optimal SR3000 additional parameter set includes first term of the radial lens distortion model (K_1), the rangefinder offset (D_0), five cyclic-error terms (D_2, D_3, D_4, D_5, D_6 and D_7) and two clock-skew error terms(E_2 and E_3). Table 3.9 shows the RMSE of the checkpoints computed based on the combined model which indicate a slight improvement in accuracy when compared to the RMSE values of the three likely models shown in Table A.2.

TABLE 3.9: RMSE of the checkpoints using combined model for the SR3000

RMSEx (mm)	**RMSEy (mm)**	**RMSEz (mm)**
7.9	20.4	5.0

For the SR4000 case, two candidate models are selected as the most likely models as per the Akaike criterion. The optimal APs of the SR4000 comprises of first two terms of the radial lens distortion terms (K_1 and K_2), two affinity terms (A_1 and A_2), decentring distortion terms (P_1 and P_2), the rangefinder offset (D_0), one cyclic error term (D_2) and a clock skew error term (E_1). Table 3.10 shows the RMSE of the checkpoints computed using combined model parameters which does not indicate any improvement in accuracy when compared with the RMSE values of the two parent models shown in Table A.1.

Generally, the accuracy in X- and Y- coordinates are lower than the Z-coordinate because of the scale factor error, which is discussed in Section 5.10. The lower accuracy in Y-axis for the SR3000 range camera may have been caused by the small depth variation of the targets in this direction as targets were located on a planar surface.

TABLE 3.10: RMSE of the checkpoints using combined model for the SR4000

RMSEx (mm)	**RMSEy (mm)**	**RMSEz (mm)**
18.4	14.1	4.9

3.6 Two Step Photogrammetric Calibration

Unlike the one step self-calibration bundle adjustment, the two-step photogrammetric calibration of the range camera is done by firstly performing the standard digital camera calibration using bundle adjustment and then correcting separately for the systematic bias in the range observations using empirical or physical model. This method avoids the problem of correlation between the parameters which is the sole disadvantage of the one step self-calibration adjustment. Figure 3.4 shows the correlation values between the rangefinder offset term (D_0) and the perspective center y-coordinate ($Y°$) of 11 images obtained from self-calibration of the SR3000 range camera. The high correlation values between these parameters questions the numerical integrity of the self-calibration approach as high correlation indicates that the two values are highly dependent on each other which is practically not the case as these two parameters are involved in two different models as described in Section 3.1.1. In order to avoid the aforementioned correlation problems between the parameters, the calibration for the range camera can be done in two separate steps.

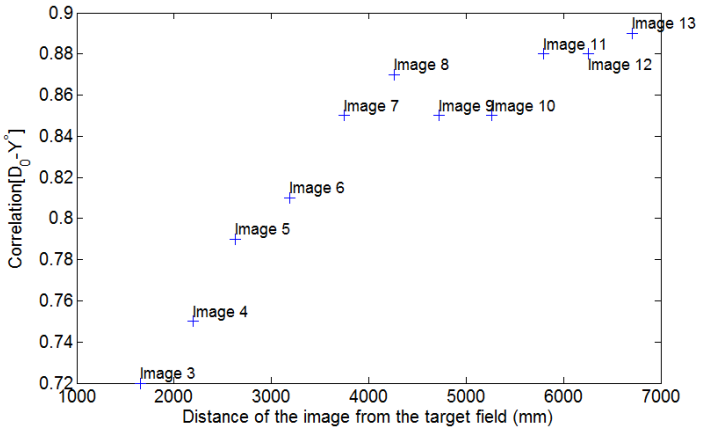

FIGURE 3.4: Correlation between D_0 and $Y°$

The two-step method is a kind of bootstrapping process similar to the one used by Boehm and Pattinson (2010). The processing involves two steps: firstly, the Euclidean distance of each of the targets for all the images are computed from the target coordinates and the camera's perspective center which are determined from the standard camera calibration; secondly, the differences between the Euclidean distances and the measured distances obtain from the cameras range image are modelled using a high-order polynomial. Instead of a physical model defining the range error, an empirical high order polynomial function is used to model the scene dependent range bias. The high order polynomial is chosen because

the range observations of the range cameras are significantly affected by unmodelled scene-dependent errors which causes deviations from the perceived physical model such as the rangefinder error model used in the integrated self-calibration method.

Only SR3000 observations are used for analysis because the range observations from this camera portray high order range bias than the SR4000. Both the normal and convergent images were used for this calibration. Two sets of model parameters were used for comparing between the one step self-calibration method and the two step photogrammetric adjustment. Table 3.11 shows the two models used for the two step calibration method. Figures 3.5(a) and 3.5(b) show the range correction using 10^{th} order polynomial.

TABLE 3.11: Two-step calibration method

Model No	**2D Calibration: Standard Lens Distortion Parameters**	**Range Calibration**
C1	K_1 K_2 K_3 A_1 A_2 P_1 P_2	10^{th} order polynomial
C2	K_1	10^{th} order polynomial

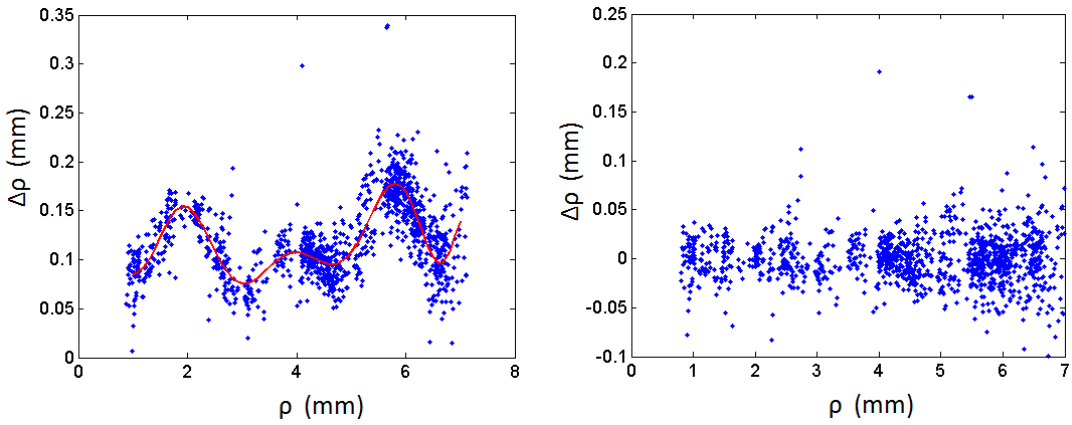

(a) Before range error correction

(b) After range error correction

FIGURE 3.5: Modelling of range error using 10^{th} order polynomial

Table 3.12 shows the two models used for the one step self-calibration method. The test data for the one step self-calibration method comprises of 3D coordinates (x,y and ρ) of target points from both orthogonally oriented images and convergent images.

Table 3.13 shows the RMSE comparison of the one- and two-step calibration methods. This result indicates that the two methods are not significantly different from each other. For

TABLE 3.12: One-step self-calibration method

Model No	**Model Parameters**	**No. of Range error terms**
C1	K_1 K_2 K_3 A_1 A_2 P_1 P_2 D_0 D_2 D_3 D_4 D_5 D_6 D_7 E_1 E_2 E_3 E_4	11
C2	K_1 D_0 D_2 D_3 D_4 D_5 D_6 D_7 E_1 E_2 E_3 E_4	11

the modelling of the scattering distortion which is discussed in Chapter 4, the two-step calibration is used as only independent range calibration is necessary.

TABLE 3.13: RMSE comparison of the one-step and two-step calibration

	One-step calibration (in mm)			**Two-step calibration (in mm)**		
Model No	**RMSEx**	**RMSEy**	**RMSEz**	**RMSEx**	**RMSEy**	**RMSEz**
C1	8.9	25.3	5.4	8.7	22.9	5.3
C2	9.0	25.5	5.5	8.8	23.0	5.3

3.7 Summary

The calibration of the range camera is still a hot topic in the research community because of the infancy of the RIM cameras and its huge potential for many close-range photogrammetric applications. The range camera suffers from various systematic and random biases, which comprises of scene-independent and scene-dependent errors. The standard camera lens distortions can be easily modelled using photogrammetric bundle adjustment, however the range measurement biases are difficult to accurately model because of the presence of the scene-dependent errors. Nonetheless some range finder biases like the rangefinder offset, cyclic and clock skew errors can be modelled using a physical model or empirically based high-order polynomial. Numerous researches are underway for developing a RIM camera calibration model either using a one step self-calibration approach or a two-step photogrammetric adjustment. This chapter has successfully shown that both methods can produce similar accuracy for the calibration of the range camera in spite of the fact that the correlation between the model parameters are a cause of concern for estimation of parameters in the integrated self-calibration method. Additionally, an AIC method is proposed for model identification in the integrated self-calibration bundle adjustment where a large number of model parameters are involved in the physical model that causes ambiguity in the selection of the model parameters.

Chapter 4

Modelling Scattering Distortion

In Chapter 3, the calibration of the range cameras was presented where some aspects of the geometric errors that are defined by a prevailing physical model such as the standard digital camera lens distortions and the rangefinder error models were incorporated in the self-calibration method. This integrated calibration model does not include other systematic range errors reported by Kavli et al. (2008) and Mure-Dubois and Hugli (2007), specifically the scattering artefact that is the main cause of the scene-dependent errors observed in the range cameras. It is important to investigate the nature of the scattering distortions in depth in order to understand the systematic behaviour of the scene-variant errors which are quite difficult to model with a general physical model because of their highly dependence on the imaging environment. This chapter is limited to only investigating the effects of the scattering bias on the range and amplitude observations in a simple two planar-objects imaging environment.

The outline of this chapter is as follows. Section 4.1 presents a brief description of the principle of the scattering effect in the 3D range cameras. Section 4.2 discusses the limitation of the shift-invariant linear system model for compensating the scattering distortion errors. Section 4.3 describes the experiments used for measuring scene-dependent scattering errors using a two-planar objects experiment and also presents some important results of the scattering-induced range and amplitude bias as a function of different parameters for the SR3000 and SR4000 range cameras. Sections 4.4 and 4.5 presents the methodology of the scattering compensation model using an analytical curve-fitting approach and the results of the two compensation models respectively.

4.1 Principle of the Scattering Effect

In the time-of-flight cameras, the range information is obtained from measuring the time delay of the modulated received signal. The phase-shift of the amplitude-modulated signal corresponds to a time delay of the signal received by the sensor. The range of the object from the sensor is calculated using Equation 4.1, where ρ is the range for a given pixel, λ is the modulation frequency, φ is the phase delay of the received signal, and i, j is the pixel location.

$$\rho(i,j) = \frac{\lambda}{4\pi} \cdot \varphi(i,j) \tag{4.1}$$

The phase-shift for the closer objects will be smaller than the phase-shift for the farther objects as shown in Figure 4.1, where A, B and C are the angular phase offsets, and the ρ_Q , $\rho_{Q'}$ and ρ_O are the corresponding ranges of the point Q, Q' and O respectively. The

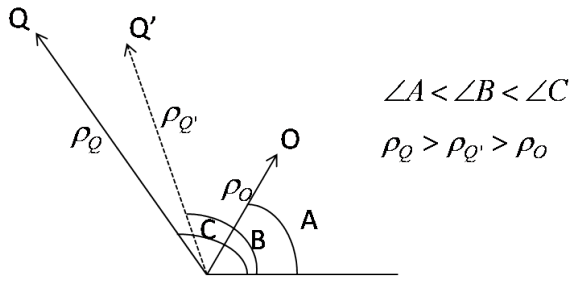

FIGURE 4.1: Angular phase-shift and range measurement

point Q' is the displaced point Q when a brighter closer object O is present in the imaging scene which causes range bias on the background object point due to the scattering artefact. The scattering effect is caused by the occurrence of multiple internal reflections between the optical lens system and the image plane where the early-arrival signals from the foreground object attenuate the late-arrival weak signal from the background object thus lowering its angular phase offset causing a shortened range measurement. However, the exact nature of multiple internal reflections of the signals is difficult to describe with a physical model because of the scattering phenomenon is highly scene dependent.

Figure 4.2 shows a schematic representation of how multiple internal light reflections from the closer object attenuates the actual signal from the farther object. For instance, a point P can be attenuated with multiple signals due to internal reflections. The difficulty of measuring the signal attenuation by an unknown number of internal reflections poses a limitation on any perceived physical model of the scattering artefact.

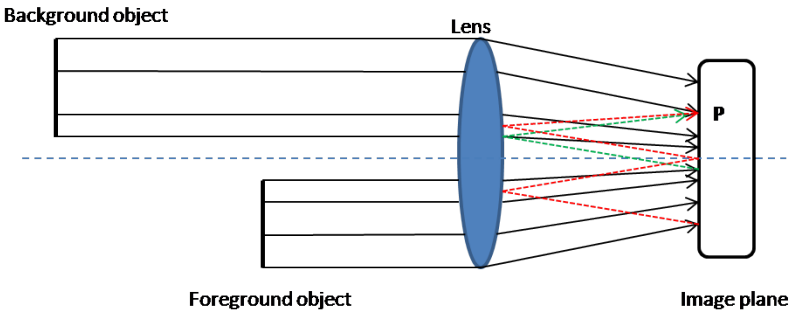

FIGURE 4.2: Internal light reflection

4.2 The Linear System Model and its Limitations

According to Mure-Dubois and Hugli (2007), the scattering problem is expressed as a convolution of the input signal with the impulse response of the system in the presence of the scattering bias. For the scattering phenomenon occurring in the 3D range cameras, the measured signal, $g(i,j)$ in every pixel is equal to the convolution of the input signal, $f(i,j)$ and the PSF of the camera including the scattering bias, $h(i,j)$ as given in Equation 4.2.

$$g(i,j) = f(i,j) * *h(i,j) \tag{4.2}$$

The solution to this problem explicitly requires modelling of the scattering PSF of the camera so that deconvolution can be employed to undo the effect of the scattering. The linear system model typically requires defining or measuring the PSF accurately in order to successfully undo the filtering operation. They define the point-spread function of the camera including scattering bias plausibly by a trial and error method using a Gaussian approximation. They reported correcting scattering errors in the range image from 30% to 90% using their method.

The main problem of the linear system model is that the direct measurement of the scattering PSF is impossible because of the non-idealization of a point scattering object. Often the line spread function (LSF) or the edge spread function (ESF) is measured to deduce the PSF indirectly which is equal to the derivative of the scattering ESF. An experiment using two planar objects was conducted to measure the ESF of the scattering effect. The range camera was placed at 1 m from the scattering object (plane board) and 2.5 m from the background object (wall). Multiple image frames were captured with and without the presence of the scattering object.

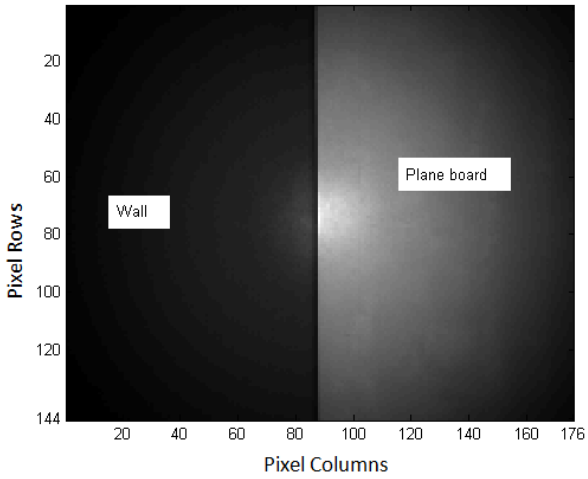

(a) Intensity image

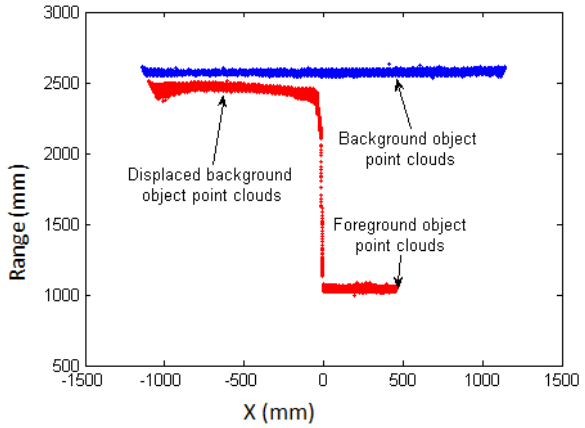

(b) Superimposed point clouds of with and without the scattering object

FIGURE 4.3: Measurement of the scattering ESF

Figure 4.3(a) shows the intensity image of the ESF experiment and Figure 4.3(b) shows the superimposed point clouds of the scattering scene with and without the presence of the foreground scattering object. The long linear band of points is the point cloud of only the background object when the scattering object is not present, whereas the step-like band of points is the point cloud of both the background and the scattering object. The displacement of the background wall towards the camera due to the presence of the foreground object is caused by the scattering phenomenon.

Figure 4.4 shows the superimposed theoretical and measured ESF obtained from the scattering experiment. The dotted line represents expected theoretical ESF, whereas the solid line represents the measured ESF obtained by fitting a curve on one row of pixels of the step-like band of points shown in Figure 4.3(b). The measured ESF does not conform to the

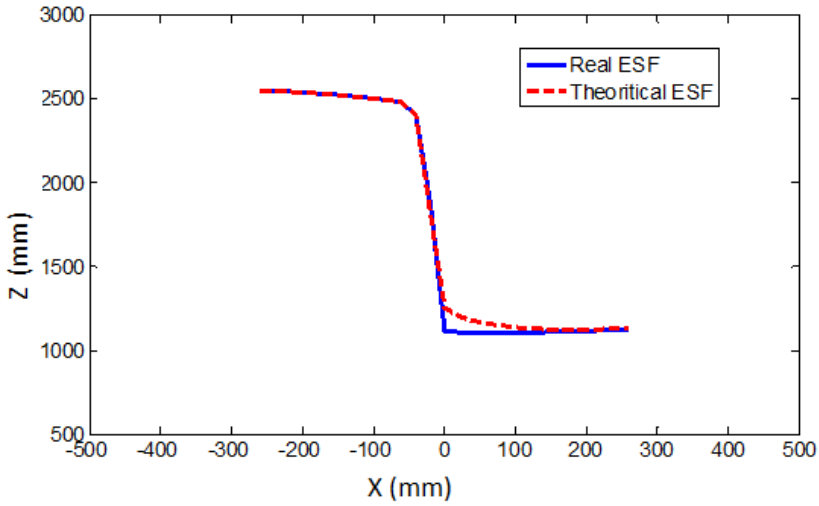

FIGURE 4.4: ESF profile of a scattering distortion

expected theoretical ESF of the scattering distortion profile. This indicates that the scattering range bias deviates from the linearity assumption of the linear shift-invariant system. It is shown in the following section that the scattering effect is non shift-invariant because the scattering bias is highly dependent on the position of the foreground scattering object. Perhaps the linear system model does not accurately describe the scattering phenomenon in a 3D range camera. In the absence of a concrete physical scattering model, it is imperative to explore the empirical methods of modelling scattering distortion through exhaustive experimentation, which is the subject of this chapter.

4.3 Measurement of the Scattering Effect

4.3.1 Two Planar Objects Experiment

The SR3000 and SR4000 range cameras were used for modeling the scattering artefact. A planar wall was imaged with and without the presence of another highly reflective foreground planar object. A white projector screen of size 2.4 m by 2.4 m was used as a foreground scattering object. Figure 4.5 shows the experimental set up for the scattering imaging scene.

FIGURE 4.5: Set up for the scattering experiment

Five forward distance (longitudinal) positions were chosen at 1.4 m to 3.8 m with a 0.4 m interval from the range camera. Nine lateral positions were chosen at each forward distance location where images were taken with different percentage of surface area of the foreground object from 10% to 90% at a 10% intervals. The 10% occlusion means that the only 10% of the surface area of the scattering object is within the field-of-view of the camera thus 90% of the surface area of the background object is in the field-of-view of the camera. The scattering edge is defined as the location of the edge of the foreground object, where the edge of the foreground object overlaps with the background object. Figure 4.6 shows the schematic representation of the 10% and 90% occlusion states of the scattering imaging scene.

The experiment was conducted only up to 3.8 m of the camera's range because of the unavailability of a sufficiently large foreground planar object which is required to cover the whole sensor frame with the foreground object. Figure 4.7 shows the geometry of the scattering scene captured at all longitudinal and lateral positions of the foreground scattering object. At each imaging location, 20 frames were captured to average out the random noise of the system. Images were captured at four different integration times at 50, 120, 180 and 255 8-bit quantized values, which correspond to 10.2 ms, 24.2 ms, 36.2 ms and 51.2 ms respectively for the SR3000 and 5.3 ms, 12.3 ms, 18.3 ms and 25.8 ms respectively for the SR4000.

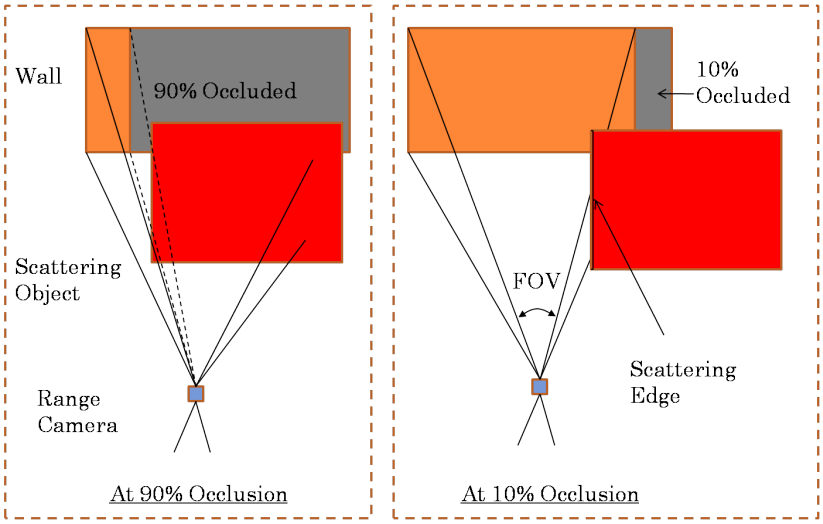

FIGURE 4.6: Field-of-view coverage at 10% and 90% occlusion

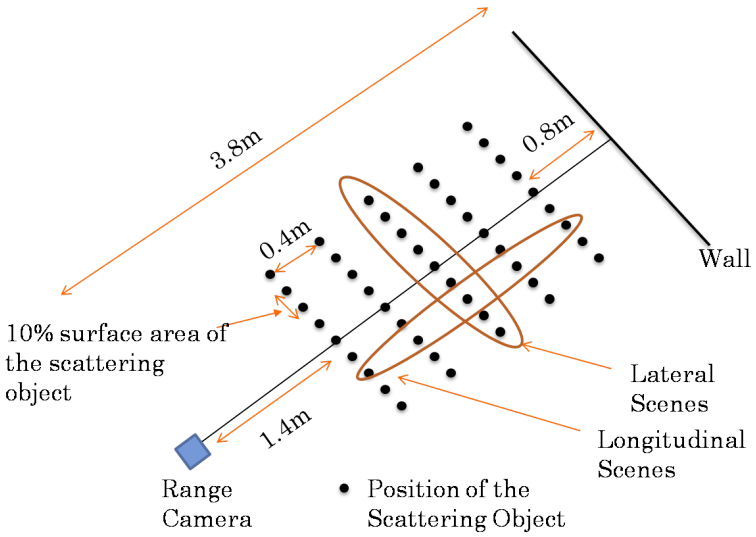

FIGURE 4.7: Geometry of the scattering experiment

4.3.2 Scattering Effect on the Range and Amplitude Observation

4.3.2.1 SR3000 SwissRanger Camera

The scattering artefact in the range cameras is portrayed in the form of range and amplitude biases on the background object. The measured range and amplitude for the background objects in the presence of a scattering foreground object are lower than the measurements without the presence of a scattering object. Hereafter, the x-coordinate refers to the image

space of the camera. Figure 4.8 shows the range and amplitude bias of one central row of pixels as a function of the surface area of the scattering object.

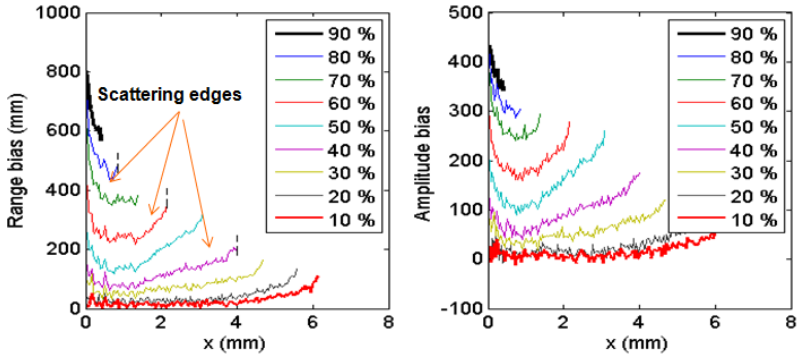

FIGURE 4.8: Range and amplitude biases as a function of surface area of the scattering object

The camera and the background object were fixed at 3.8 m with the scattering object placed at different lateral positions at a distance of 1.8 m from the camera. The trend is clearly visible where the range and amplitude bias are increasing monotonically as a function of the surface area of the scattering object. This is expected because when the surface area of the scattering object is larger, more scattering is occurring inside the camera causing greater attenuation of the signals from the background object. It is also observed that the range bias gradually decreases from the scattering edge towards the center of the image and then exponentially increases towards the periphery of the image. The scattering edge is located at the right end of the curves. Some portion of this additional bias at the periphery can be attributed to the power loss due to the vignetting effect of the lens. However, the range biases at the edges are not homogenous throughout the image frame, which indicates that there are other system errors influencing the scattering distortion.

Further observation exposed the proportional dependence between the range and amplitude bias. It has been reported by Mure-Dubois and Hugli (2007) that the phase-shift due to the scattering effect is proportional to the ratio $\Delta A/A$. From Equation 4.1, it can be seen that the range bias is proportional to the phase-shift, therefore the range bias is also proportional to the ratio $\Delta A/A$. Figure 4.9 is the range and amplitude bias dependency plot using un-normalized and normalized amplitude bias. The amplitude bias(ΔA) is normalized with the amplitude (A) of the signal from the background object.

The left image of Figure 4.9 is a linear fit of individual data of corresponding range and amplitude bias and the right image is the superimposed of linear and polynomial fits of all data at different surface area of scattering object seen in Figure 4.9. It can be observed that the proportional dependency of range and amplitude bias is true for the lower range

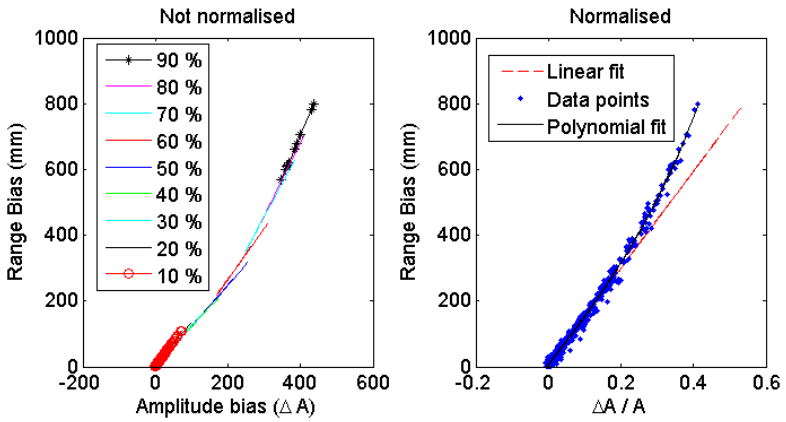

FIGURE 4.9: Amplitude and range bias dependency plots

biases but exhibits a monotonically increasing low-order polynomial relationship for the larger range biases.

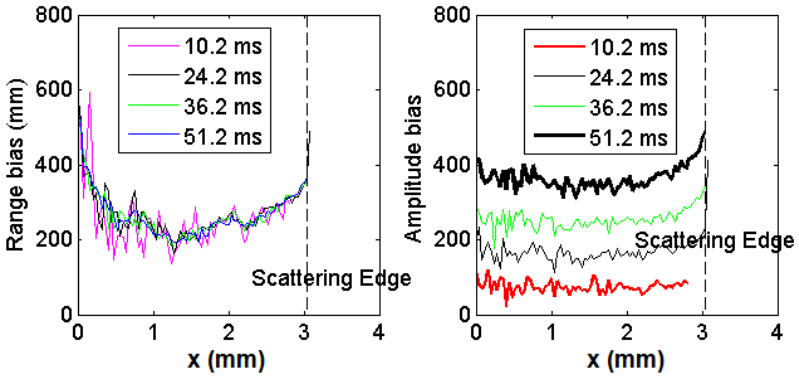

FIGURE 4.10: Range and amplitude biases as a function of the integration time

Figure 4.10 shows the range and amplitude bias as a function of the integration time. This image is taken with a range camera placed at 1.8 m and 3.8 m from the scattering and background object respectively with 50% occlusion of the background object. All four different integration times for the same scattering scene show a very similar range biases. This suggests that the scattering effect on range measurements is invariant to the integration time. However, the amplitude bias due to scattering is dependent on the integration time. The monotonic relationship between the integration time and the scattering-induced amplitude bias is because a greater number of photons impinge on the sensor at higher integration times.

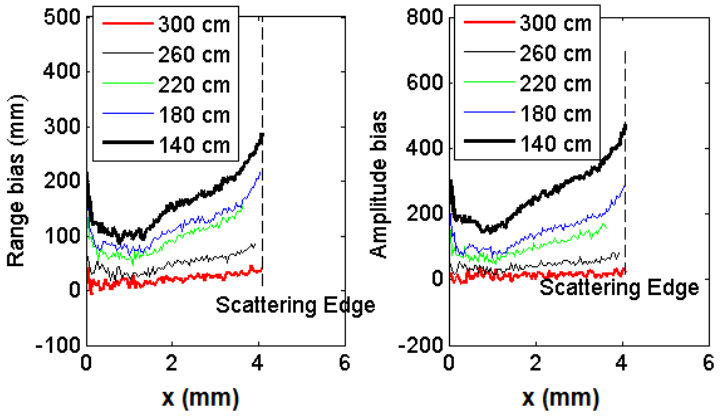

FIGURE 4.11: Range and amplitude biases as a function of distance of the scattering object from the camera

Figure 4.11 portrays the range and amplitude bias as a function of the distance of the scattering object from the camera. These images were taken with the camera placed at 3.8 m from the background object and the scattering object placed at four different locations at 0.4 m increments starting at 1.4 m from the camera. It has been observed that the range and amplitude biases monotonically increase with the distance of the scattering object from the camera. This is expected because the power density of the signal decays as the inverse square of the distance. When the scattering object is closer to the camera relative to the background object, the reflected light from the scattering object has more power than the reflected light from the background object causing greater signal attenuation resulting in proportional scattering bias.

Figures 4.12(a) and 4.12(b) show the variation in range bias at different scattering scene environments. In both the figures, it is clearly visible that the scattering induced range bias is more in the periphery than the inside portion of the image plane. This is due to a greater power loss of the reflected signal at the periphery than in the middle portion of the imaging scene. The additional power loss of the SR3000 range camera at the periphery besides the cosine-fourth power loss observed in standard optical systems has been reported by Jaakkola et al. (2008).

Kavli et al. (2008) and Mure-Dubois and Hugli (2007) reported a maximum of 400 mm of range bias due to scattering based on their experiment. On the contrary, this study has shown that the scattering-induced range bias could reach up to 2500 mm in the presence of a highly reflective large surface area scattering object when the scattering and the background objects are separated at an appreciable distance.

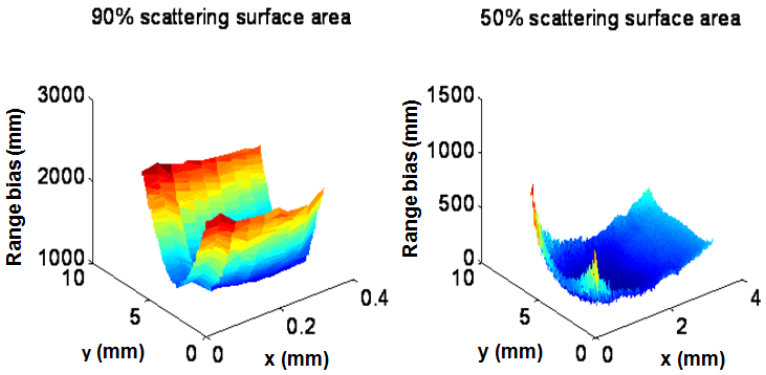

(a) Camera at 140cm and 380 cm from the scattering and background object respectively

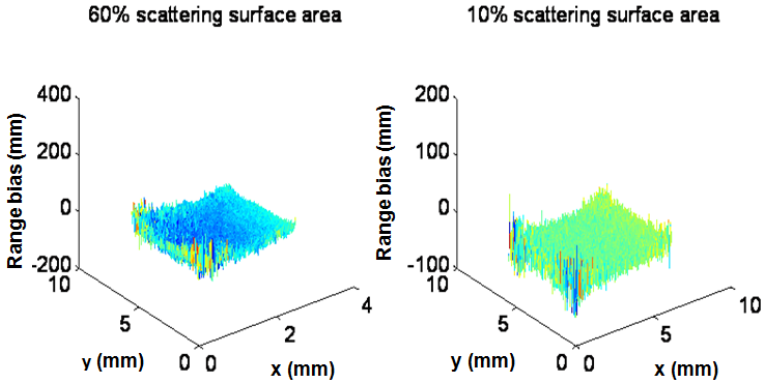

(b) Camera at 240cm and 380 cm from the scattering and background object respectively

FIGURE 4.12: Scattering induced 3D range bias

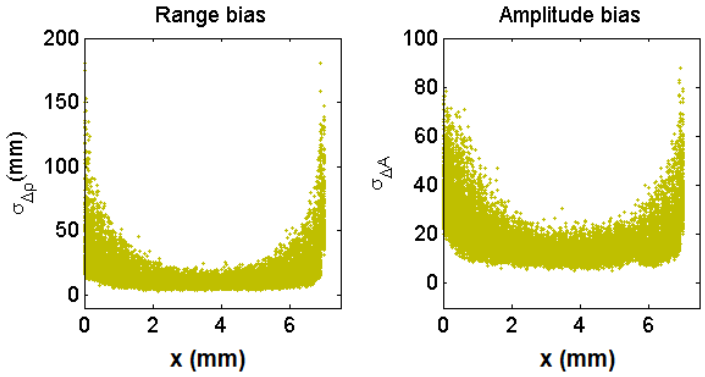

FIGURE 4.13: SR3000 noise for consecutive images

Figure 4.13 is the standard deviation plot of the range and amplitude bias for twenty consecutive images of a planar wall. The range noise is within 200 mm and amplitude noise is within 100 16-bit quantized values. Figures 4.12(a) show that the scattering induced bias is greater than the inherent system noise thus requiring modelling and compensation of the scattering induced biases for SR3000 range camera.

4.3.2.2 SR4000 SwissRanger Camera

Chiabrando et al. (2009) have reported the absence of scattering distortions in the SR4000, which is the fourth generation range camera. However, it has been observed in this study that the scattering-induced biases exist but are not as significant as in the SR3000.

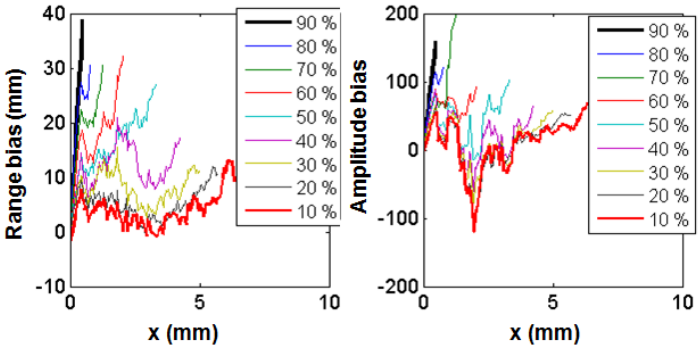

(a) Range and amplitude biases as a function of the surface area of the scattering object

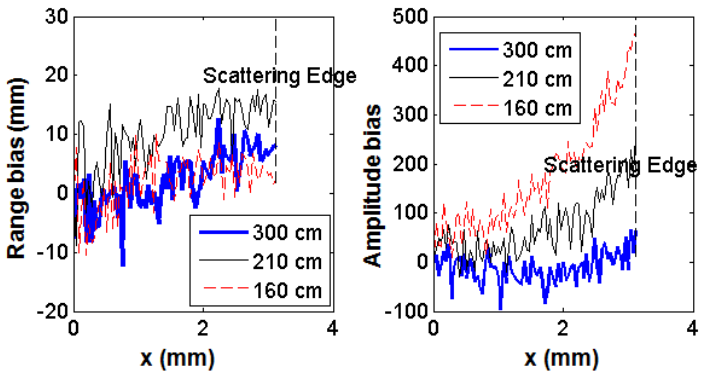

(b) Range and amplitude biases as a function of the distance of the scattering object from the camera

FIGURE 4.14: Scattering induced range and amplitude bias for SR4000

Figure 4.14(a) shows the ten-point moving average plot of the range and amplitude bias of one central row of pixels as a function of the surface area of the scattering object. The images were captured with a camera at 3.8 m from the background object with the scattering object positioned at nine lateral positions at 2.2 m from the camera. Figure 4.14(b) shows the scattering induced range and amplitude bias as a function of the distance of the foreground scattering object from the camera. These images were taken with the camera at 4.2 m from the background object with 50% surface area of the scattering object positioned at different distances from the camera. The maximum scattering-induced range bias in the SR4000 is observed to be 80 mm, which is an order of magnitude less than the range bias observed in the SR3000. This shows that the scattering artefact in this camera is greatly reduced or eliminated as compared to the scattering bias observed in SR3000. However it is not known how the scattering artefact in SR4000 is rectified by the manufacturer, either through software implementation or hardware consolidation.

The standard deviation plot of the range and amplitude biases for twenty consecutive images of a planar wall is shown in Figure 4.15. The range noise is within 50 mm and the amplitude noise is within 300 16-bit quantized values. Interestingly, it is observed that the amplitude bias of the SR4000 is three times more than the amplitude bias of the SR3000 camera, though range bias has been improved by a factor of two.

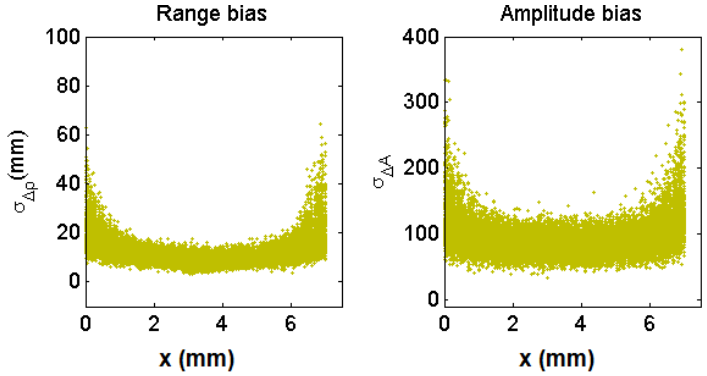

FIGURE 4.15: SR4000 noise for consecutive images

4.4 Methodology for the Scattering Compensation

A 3D surface-fitting algorithm is used to smooth the noisy 3D point cloud of the scattering scene. The smoothed surface is then used for scattering compensation using a cubic spline

interpolation method. The three-step process for scattering compensation is discussed in the following sub sections.

4.4.1 Removing the Mixed Pixels

The raw data from the scattering scene contain mixed pixels at the scattering edge, which is the overlap region between the foreground and the background surfaces. The mixed pixels are caused by ambiguity in range measurement of the signals received from the foreground and background objects at the same pixel. An automatic process of removing all the pixel columns containing mixed pixels in the foreground scattering scene is achieved using linear and polynomial regression of the pixel columns based on a mean square error threshold.

Because the imaging surfaces are planar objects, the pixel columns appear as either a linear or low order curvature band of points. The presence of the mixed pixels in the scattering edge causes deviations of the point cloud from the linear or polynomial trend which is easily determined by the sum of the squared errors (SSE) of the curve fitting. Any pixel columns that have SSE above a certain threshold are removed from the dataset. Figures 4.16(a), 4.16(b), 4.17(a) and 4.17(b) show the robust line fitting and polynomial fitting methods used for isolating the mixed pixels which are the most undesirable noise present in the scattering data.

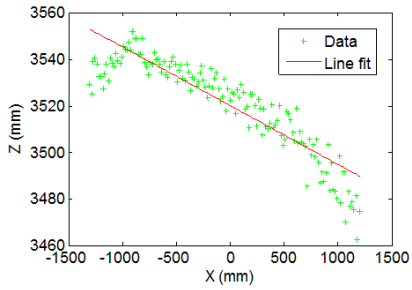

(a) Absence of mixed pixel leads to good fit of a line

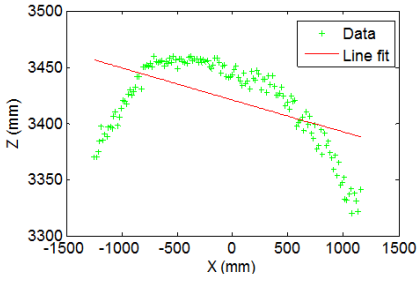

(b) Presence of mixed pixel causes large deviations from the best-fit line

FIGURE 4.16: Robust line fitting method to isolate the mixed pixels

Figure 4.18 shows the uncleaned and cleaned point clouds of the foreground scattering scene superimposed on the background scene point clouds.

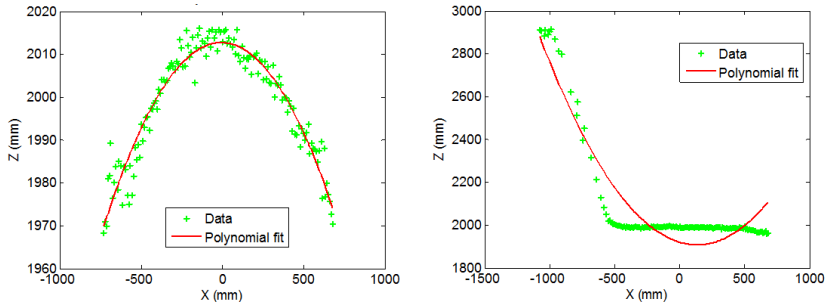

(a) Absence of mixed pixel leads to good fit of a polynomial

(b) Presence of mixed pixel causes large deviations from the polynomial fit

FIGURE 4.17: Polynomial fitting method to isolate the mixed pixels

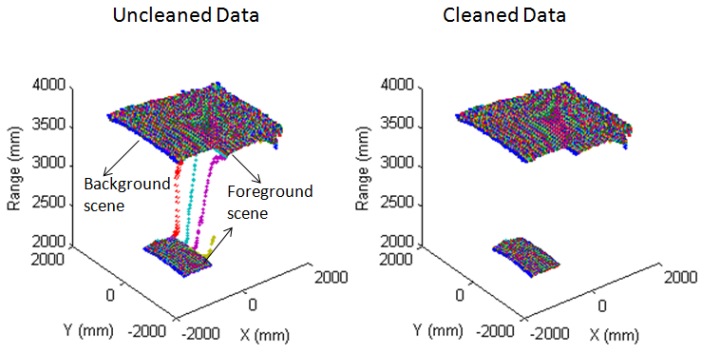

FIGURE 4.18: Cleaning mixed pixels

4.4.2 Smoothing: 3D Surface Fitting

A generalized ridge estimator is used to fit a smooth surface to 3D grided data points. The choice of this algorithm over other polynomial surface fitting is because this method robustly fits a surface as closely as possible by accommodating the noise in the data by a user-defined smoothing or fairing parameter. This algorithm is not merely an interpolating function but more of an approximating function where an interpolating function is coupled with an absolute constraint, which is scaled with a fairing parameter for controlling the smoothness of the estimated surface (D'Errico, 2005).

The objective of this method is to estimate the curved surface Z = f(X,Y) values at the rectangular grid nodes using a 3D point cloud of the range camera. Figure 4.19 shows the grid nodes and the known data points used for the surface fitting. A surface is estimated basically by approximating the Z values of all the nodal points in the rectangular mesh. This

is achieved by using a local interpolating function such as linear triangular interpolation method given in Equation 4.3 and schematically shown in Figure 4.20

$$Z = Z_1 + u * \overrightarrow{Z_1 Z_3} + t * \overrightarrow{Z_1 Z_2} \tag{4.3}$$

where Z_1, Z_2 and Z_3 are the Z-coordinates at the three vertices of a triangle, and t and u are the scalars in X- and Y-direction respectively.

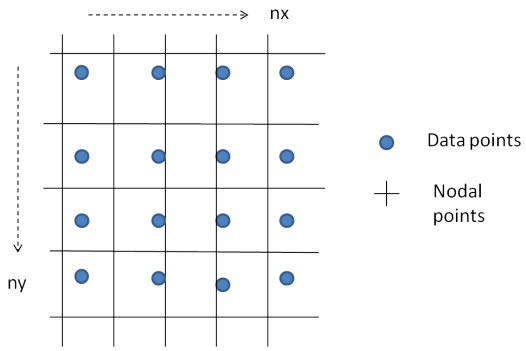

FIGURE 4.19: Known data points and unknown nodal points

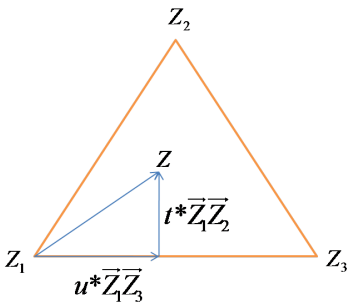

FIGURE 4.20: Linear interpolation in a triangle

Mathematically, the interpolation at any point in the gridded mesh is simply a linear combination of the function values at the nodal points which can be represented by a linear algebra problem as given in Equation 4.4

$$Ax = y \tag{4.4}$$

where A is a Jacobian matrix of partial derivatives w.r.t unknown parameter, the vector x is the parameter unknowns of length nx $\times$ ny (nx and ny are the number of nodes in the X- and Y- direction respectively) and y is the vector of known observations. Thus A has n

(number of observations) rows, i.e the number of data point supplied by the user, and nx × ny columns. In such case of estimation it is very likely to have more number of columns than rows because a user may choose to build a dense gridded surface. Hence, the regression problem becomes highly underdetermined where the unknowns exceeds the known values. For instance, Figure 4.19 shows 25 nodal points where Z values at each nodal point have to be determined from a total of only 16 available data points. A least squares solution to such underdetermined regression problem is highly unreliable. However, the plate-bending mechanism used in the ridge estimator solves this underdetermined problem by imposing an absolute constraint where the gradient of the surface in the neighboring cells are forced to be equal. This results in a second set of linear equations of the form shown in Equation 4.5

$$Bx = 0 \tag{4.5}$$

where B is the constraint matrix with gradient values approximated using finite differences of the surface at the neighboring nodes. Hence, the objective function of the least squares is to minimize the L2 norm of the joint function of the interpolating function, Equation 4.4 and the regularization function, Equation 4.5. The minimization function is shown in Equation 4.6

$$\phi_{min} = \|(Ax - y)\|^2 + J\|Bx\|^2 \tag{4.6}$$

where J is the fairing parameter that defines the amount of rigidity of the bending plate. As J approaches zero, the plate becomes very flexible. A higher fairing parameter will produce a smoother surface but the approximated surface will be less accurate, and vice-versa. More on bending plate mechanism is discussed in Yamada et al. (1999), Greiner et al. (1996) and D'Errico (2005).

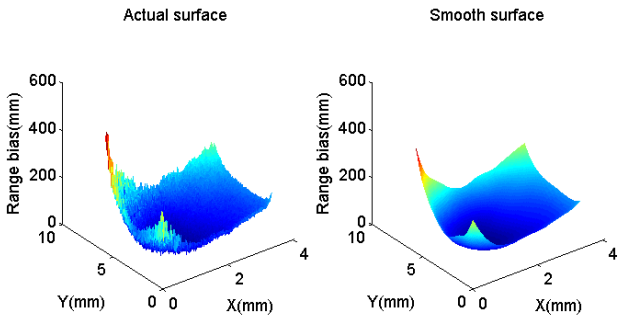

FIGURE 4.21: Actual surface (Left) and smooth surface (Right)

Figure 4.21 shows the result of the 3D surface fitting algorithm on the point cloud of the range camera.

4.4.3 Interpolation: Not-a-Knot Cubic Spline

Using the surface fitting algorithm, smooth range bias surfaces are obtained for different positions of the scattering object. Then a piecewise cubic polynomial interpolation is used to approximate the value for the required lateral or longitudinal distance using the corresponding pixel values from all the available smoothed surfaces.

Mathematically, the cubic spline is defined by the cubic polynomial in Equation 4.7 which is defined for each sub-interval $[x_i,x_{i+1}]$, where i = 1, 2,$\cdots$, N-1. For N number of points, there are N-1 cubic polynomials with 4(N-1) parameters.

$$F_i(x) = a_i + b_i(x - x_i) + c_i(x - x_i)^2 + d_i(x - x_i)^3 \tag{4.7}$$

Constraining Equation 4.7 with the following four conditions gives a unique solution. The detail description of the spline estimation is presented in Section B.1 in Appendix B.

- The spline pass through all data points.
- The first derivative is continuous at all interior points.
- The second derivative is continuous at all interior points.
- The boundary conditions at the end points are defined.

When the boundary conditions at the end points are defined as in Equation 4.8, the spline is called not-a-knot spline and when the first derivatives of the end points are set to a predefined value then it is called a clamped spline.

$$\left.\begin{aligned} {F_1}'''(x_2) &= {F_2}'''(x_2) \\ F'''_{N-2}(x_{N-1}) &= F'''_{N-1}(x_{N-1}) \end{aligned}\right\} \tag{4.8}$$

The not-a-knot and clamped splines has been tested for the interpolation of the scattering surface, of which the not-a-knot spline fitted the scattering data better than the clamped spline. Figure 4.22 shows the fitting result of the two splines.

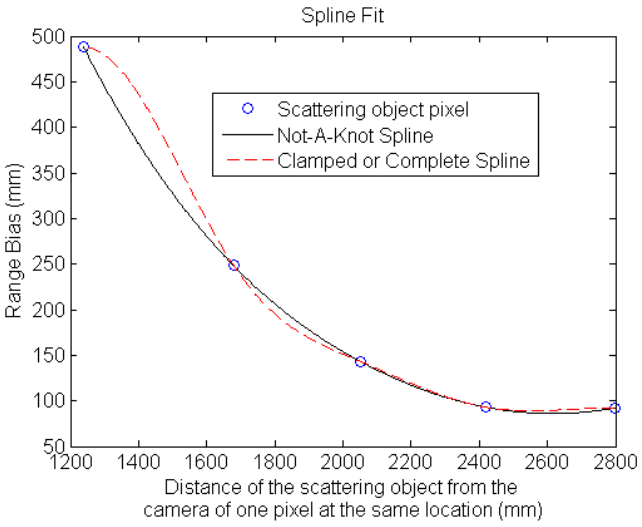

FIGURE 4.22: Two method of spline interpolation

4.5 Scattering Compensation Model

The range bias due to scattering is the subject of interest in this study. A range bias scattering compensation model based on the analytical curve-fitting method is proposed. Two different models have been tested to compensate for the scattering-induced range bias on the background object. The flowchart shown in Figure 4.23 describes the two models.

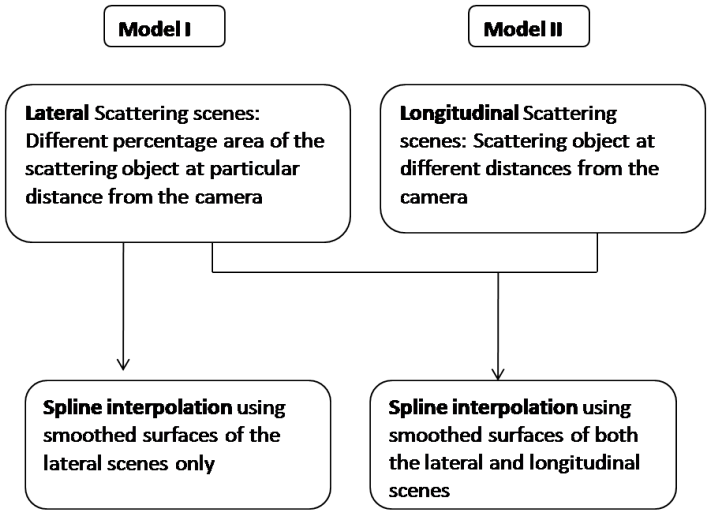

FIGURE 4.23: Flow diagram of the empirical scattering compensation models

4.5.1 Compensation Model I

Model I is a local compensation model defined only for a scattering object located at a particular distance from the camera where ancillary data of lateral scattering scenes are available for different percentage surface areas of the scattering object. The approximation of the required surface at a particular surface area of the scattering object is achieved by calculating values at each pixel location using the corresponding pixels values of the smoothed surfaces available at different locations of the scattering object. The not-a-knot spline interpolation is used to estimate the approximate correction surface.

Figure 4.24 shows the superimposed actual and approximated surfaces and the success rate of the scattering compensation for Model I. The scattering compensation is tested for 55.7% surface area of the scattering object, when the scattering object and the background object are at 2.2 m and 3.8 m from the camera respectively. The success rate is calculated by computing the percentage difference of range bias between the actual and approximated range bias surfaces for all pixels independently. The achievement of this scattering compensation model is more than 80%, which corresponds to a maximum error of 21 mm. The high success rate for this model is due to the availability of dense data set for the lateral positions.

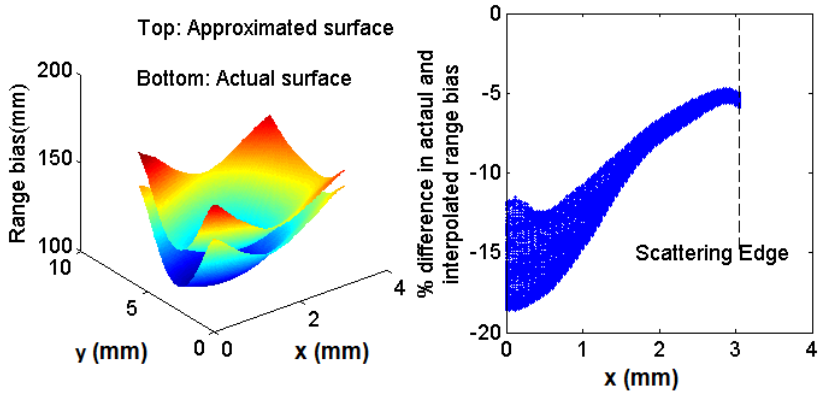

FIGURE 4.24: Scattering compensation for scattering object at 220 cm from the camera for Model I

4.5.2 Compensation Model II

Model II is a general compensation model defined at all distances for all percentage surface areas of the scattering object from the camera where ancillary data of both the lateral and longitudinal scattering scenes are available. The approximation of the surface at the required distance from the camera for a particular surface area of the scattering object is achieved

in two steps. Firstly, an intermediary surface at the required percentage surface area of the scattering object is computed using the lateral scenes. Secondly, from the intermediary surfaces obtained at the desired percentage surface area of the scattering object, a new surface is interpolated at the required longitudinal distance of the scattering object from the camera.

Figure 4.25 shows the superimposed of actual and approximated surfaces, and the success rate of the scattering compensation at 53.4% surface area of the scattering object when the scattering and background objects are at 2.2 m and 3.8 m from the camera respectively. This compensation model has accounted for more than 60% of the scattering distortion which corresponds to a maximum error of 43 mm. The lower success rate of this compensation model relative to Model I is because only sparse ancillary data are available for interpolation, which has biased the spline model.

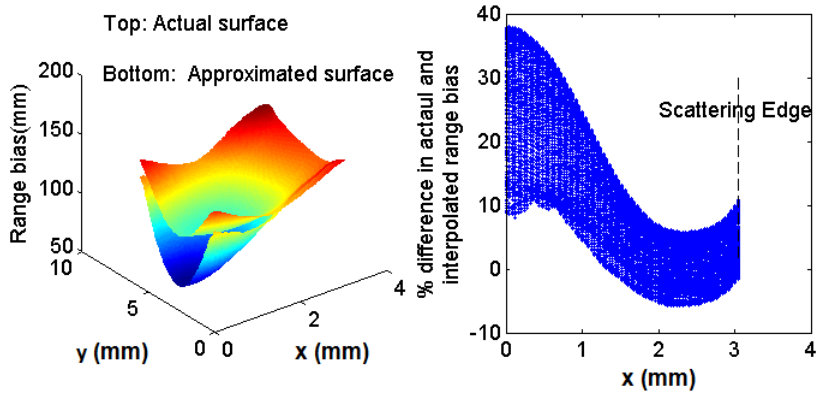

FIGURE 4.25: Scattering compensation for scattering object at 220 cm from the camera for Model II

4.6 Summary

By using a two planar-objects experiment, the effects of the scattering errors on the range and amplitude observation have been quantified for both the SR3000 and SR4000 range cameras. It has been explicitly shown that the scattering induced biases are scene-variant and non-linear, unlike the linearity and the invariance assumption of the liner system model. The scattering errors depends on the position and size of the scattering objects. In the presence of the large foreground objects at a closer distance, the scattering-induced range bias may reach up to 2500 mm on the range measurement of the background objects. The proposed empirical compensation model successfully accounted for about 60% scattering errors using Model I and about 80% using Model II. However, these corrections models are

only valid for scattering scenes having planar surfaces because the scattering effect is highly scene-dependent. In a complex scenes where multiple objects of different shapes and forms are present, the scattering effect is more complicated as it is additionally compounded by the effect of the multipath. Therefore, the scattering errors of the range cameras are difficult to compensate with a general physical model.

On the other hand, it has been observed that the SR4000, which is the current generation range camera is more resistant to the scattering errors. This improvement of the range camera may have been achieved by hardware and software improvements in the lock-in-pixel technology. For a small surface foreground object, the scattering errors observed in the SR4000 are within the noise of the system. Therefore, the SR4000 range camera is used in Chapter 5 to investigate the potential application of the RIM cameras for structural deformation measurements. The deformation measurement requires sub-millimetre accuracy to accurately sense the deflection of the structure under external loading conditions which can only be met by the SR4000, which is less susceptible to scene-dependent errors.

Chapter 5

Application of the SR4000 Range Camera for Structural Deformation Measurements

In Chapter 4, the scene-dependent scattering effect in the SR3000 and the SR4000 was presented. It was observed that the SR3000 range cameras are severely effected by the scattering errors which poses a limitation on the use of this range camera for precise measurement applications. On the other hand the SR4000 range cameras are very resistant to the scattering induced range biases thus making this latest generation range camera capable of using for precise engineering applications such as structural deformation measurements. This chapter investigates the use of the SR4000 range camera for precisely measuring deformation of structural beams under external loading conditions in a laboratory test field.

Section 5.1 states the advantages of using a range camera for structural deformation measurement. Section 5.2 presents the theoretical and mathematical aspects of the beam deflection phenomenon. Section 5.3 presents the design of the experiment and the method of data collection. Sections 5.4 and 5.5 discuss the method of data preparation and processing of the range camera and the terrestrial laser scanner data respectively. Section 5.6 presents the repeatability test of the range camera measurements. Sections 5.7 and 5.8 elaborately present the quantitative and qualitative analysis of the three phases of experiments conducted on two concrete beams with and without the steel-reinforced polymer sheets respectively. Section 5.9 discusses the measurement precision and accuracy of the range camera for beam deflection measurements. This chapter concludes with Section 5.10, where some of the limitations of the range camera are discussed.

5.1 Why a Range Camera?

Structural deformation tests are carried out in an indoor facility to study the characteristics of the structural members under different stress conditions. Traditionally this had been achieved by using contact sensors such as dial gauges and linear-variable differential transducers (LVDTs) which are highly accurate measuring devices. However these devices are limited owing to the need for placing the sensors in contact with the structure thus prohibiting measurement of the deflection at the moment of the final destruction. Additionally, these devices are only capable of measuring the changes in one direction.

So to mitigate the deficiencies of the traditional deflection measuring devices, photogrammetric methods using close-range cameras are now commonly employed for the structural deformation measurements with millimetre level accuracy (Fraser and Riedel, 2000; Whiteman et al., 2002). But the camera system requires multi-oriented images in order to obtain a stereo geometry for computing three dimensional coordinates of the targets. This process of determining the 3D coordinates is tedious and time consuming, and at times is even unsuccessful if the point correspondences are not found. Camera use is also limited by the requirement of numerous targets in the object scene, either paper targets or a virtual patterns which can be projected using a projector. On the contrary, the range cameras obtain 3D information of the scene directly as an output of the camera which eases the processing task. For the range cameras, even the requirement of a reflective targets can be eliminated completely.

In recent years, terrestrial laser scanners have been used for measuring structural beam deflection in both indoor and outdoor deformation studies (Ronnholm et al., 2009; Lovas et al., 2008; Park and Lee, 2007; Gordon and Lichti, 2007). The TLS system is more efficient than the traditional photogrammetric systems as it does not require special targets in the imaging network. Plus, only one exposure station is required to measure the deflection of the structure. Though it is limited by the coarse accuracy of the point clouds, the high density of point clouds facilitates accurate surface modelling thereby achieving sub-millimetre accuracy. But these devices are not capable of capturing dynamic scenes in order to map the dynamic profiles of structural deformation. Therefore the three-dimensional range camera could be employed similarly like TLS for the deformation measurements with the added benefit of providing video rate scene capture for dynamic scene reconstruction. Despite this potential, this project will only investigate the measurements of static deformation as an initial research activity which will eventually set course for the dynamic deformation studies in the future, if the static measurements are reasonably validated. Additionally, the 3D range cameras are smaller thus it can be used in congested environment and operate with greater ease

of freedom. The range camera system is also cheaper than the TLS system which is too expensive for many users.

In Chapter 4 it has been shown that the range cameras are severely affected by the scene-dependent biases such as the scattering artefact thus making it's use inappropriate for many high-precision metric applications. However, it has been observed that the fourth generation range cameras, SR4000 are less affected by the scattering effect by an order of magnitude less than the SR3000. So the use of the SR3000 for high-precision application such as beam deflection measurement is out of the question. Therefore only SR4000 range camera is investigated for its use in measuring the static deformation of the structural beam.

5.2 Mathematical Model of the Beam Deflection

Figure 5.1 shows the schematic representation of the deformation experiment of the simply supported beam at the zero load state. A beam that is subjected to a downward force will bend as depicted in Figure 5.2.

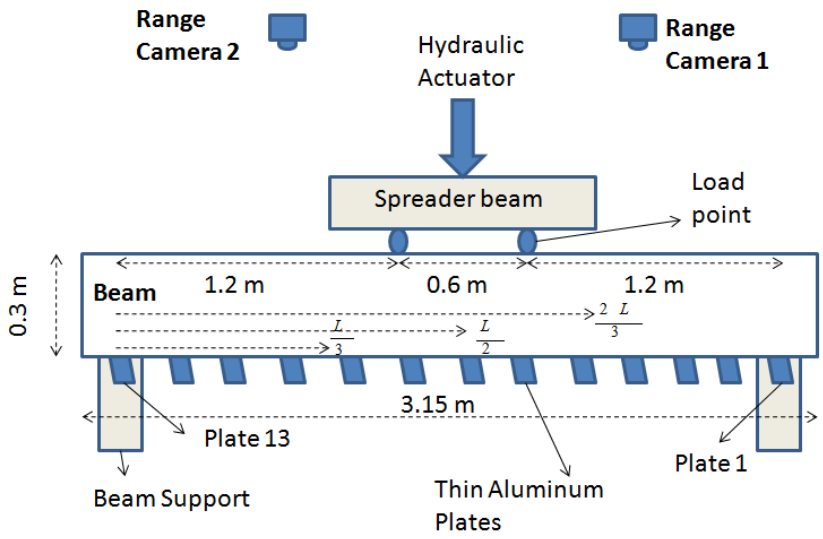

FIGURE 5.1: Beam at the zero load state

The deflection of the beam due to the load can be defined by the second-order differential equation as given in Equation 5.1 (Beer and Johnston, 1992)

$$\frac{\partial^2 z}{\partial x^2} = \frac{M(x)}{EI} \tag{5.1}$$

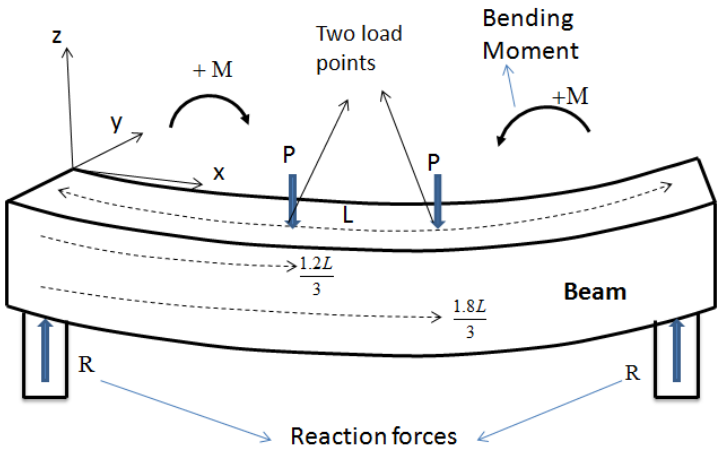

FIGURE 5.2: Beam at the loading state

where M is the bending moment which is a function of x, E is the modulus of elasticity, I is the cross sectional moment of inertia and z is the vertical deflection. Equation 5.1 is solved by the method of integration where the first integration yields gradient function and the second integration gives the deflection in the vertical direction which is the quantity of interests for the beam deflection measurements.

A physical model as similar to the one derived in Gordon and Lichti (2007) will be used to derive the deflection model. Consider a simply supported beam of length L (3 m) with downward concentrated force (P) acting at two points which are symmetrically placed about the centre of the beam. The load points are approximately located at 1.2 m and 1.8 m from one end of the beam. Since there are two load points the beam is divided into three sections i.e. $0 \leq x < \frac{1.2L}{3}$, $\frac{1.2L}{3} \leq x \leq \frac{1.8L}{3}$ and $\frac{1.8L}{3} < x \leq L$. The R is the reaction forces at the left and right supports of the beam. At the state of the equilibrium, the downward force and the upward reaction forces at the two support ends are equal. The unsupported portion of the middle section of the beam experiences a positive internal bending moment (+M) which depends on the location of the point along the beam. This bending moment cause the sagging of the beam by bending the beam concave upward (Hibbeler, 2008). The bending moments for the three sections are formulated as shown in Equation 5.2.

$$M(x) = \begin{cases} Px, & 0 \leq x \leq \frac{1.2L}{3} \\ Px - P(x-1.2), & \frac{1.2L}{3} \leq x \leq \frac{1.8L}{3} \\ Px - P(x-1.2) - P(x-1.8), & \frac{1.8L}{3} \leq x \leq L \end{cases} \tag{5.2}$$

With the E and I terms in the differential equation (Equation 5.1) are assumed to be constant, Equation 5.2 reduces to the beam deflection equation (Equation 5.3) after two integration operations, where the C terms are the constants of integration that can be determined from the boundary conditions.

$$EIz = \begin{cases} \frac{Px^3}{6} + C_1x + C_2, & 0 \leq x \leq \frac{1.2L}{3} \\ \frac{1.2Px^2}{2} + C_3x + C_4, & \frac{1.2L}{3} \leq x \leq \frac{1.8L}{3} \\ \frac{-Px^3}{6} + \frac{3Px^2}{2} + C_5x + C_6, & \frac{1.8L}{3} \leq x \leq L \end{cases} \tag{5.3}$$

By generalizing the coefficients, Equation 5.3 reduces to the simple analytical form given in Equation 5.4, which can be used to measure the beam displacement. Equation 5.4 is a problem of curve fitting of low-order polynomial which can be achieved through constrained least squares adjustment.

$$z(x) = \begin{cases} a_3x^3 + a_1x + a_0, & 0 \leq x \leq \frac{1.2L}{3} \\ b_2x^2 + b_1x + b_0, & \frac{1.2L}{3} \leq x \leq \frac{1.8L}{3} \\ c_3x^3 + c_2x^2 + c_1x + c_0, & \frac{1.8L}{3} \leq x \leq L \end{cases} \tag{5.4}$$

However, instead of using the three piece low-order polynomial functions for modelling the deflection curves, a cubic spline is a better alternative model because the thin plates used as the reference for the measurements in this experiment are not aligned and levelled perfectly. The non-alignment of the beam is caused by the sagging of the beam due to its own weight as it is supported only at the two ends, and by the use of unequal amount of glue to attach the plates from the bottom surface of the beam. The thin plates which are shown in Figure 5.1 are the reference points which are used for measuring deflection of the beam at different measurement epochs. This unevenness of the thin plates causes unnecessary smoothing of the polynomial regression which is not sought for in this estimation. The cubic spline conforms with the polynomial function because of the use of cubic function in the piece wise modelling of the spline. Additionally, the spline curve can be greatly localized to fit the observation data. Thus the estimation of the deflection values at different measurement epochs is done by the cubic spline interpolation method. A detailed mathematical derivation on the modelling of the cubic spline is described in Section B.1 in Appendix B.

The x and z values needed for the measurement of the beam displacement in Equation 5.4 are obtained from the range camera observations. The range observation (ρ) is the critical parameter in defining the z value which is the main parameter for quantifying the

displacement of the beam. Therefore it is crucial to investigate the systematic and random biases effecting the range observations.

$$\Delta\rho = \begin{cases} D_0 + D_2 \sin\left(\frac{2\pi}{R_u}\rho\right) + E_1\overline{x} & modelled \\ \quad + & \\ \Delta S_\rho + \Delta I_\rho + \Delta M_\rho + \epsilon & unmodelled \end{cases} \tag{5.5}$$

Equation 5.5 shows the modelled and unmodelled systematic and random biases effecting the range observations. The modelled parameters refer to the rangefinder biases that are quantified in the self calibration adjustment and the unmodelled parameters such as scattering bias (ΔS_ρ), incidence angle error (ΔI_ρ), multipath effect (ΔM_ρ), noise of the sensor (ϵ) are the ones which are difficult to model due to their high dependence on the imaging environment. Nevertheless the problem of unmodelled biases is solved numerically because of the need for differencing the two measurements in order to obtain the displacement of the beam. All the measurements at the subsequent epochs are subtracted from the measurement at the zero load state to obtain the deflection of the beam at that particular epoch, which is expressed in Equation 5.6

$$\begin{aligned} \Delta\rho_{0i} =& \rho_0 + \Delta\rho_0 + \epsilon_0 - \rho_i - \Delta\rho_i - \epsilon_i. \\ =& \rho_0 - \rho_i + \Delta\epsilon \end{aligned} \tag{5.6}$$

where ρ_0 and ρ_i are the range observations at the zero load and the i loading state respectively, $\Delta\rho_0$ and $\Delta\rho_i$ are the systematic biases at the zero and i states respectively and ϵ_0 and ϵ_i are the system noise at the two states respectively. It is assumed explicitly that the scene-dependent systematic biases for all other measurement epochs remain constant and is equal to the biases occurring at the zero state loading condition. Thus the first difference method of computing the deflection values by subtracting the measurements of the subsequent epochs from the zero load state cancels out the systematic biases occurring at all measurement epochs. However, the system noise is not eliminated by the differencing method due to the stochastic nature of the noise. The noise is modelled stochastically in the calibration of the range observation as discussed in Section 3.1.2.

5.3 Data Collection

The experiment was conducted in a controlled indoor testing facility in the Department of Civil Engineering laboratory at the University of Calgary. A white-washed structural beam

of length 3 m supported at its two ends was used. The load was applied by a hydraulic-actuator having maximum force capacity of 250 kN, on a spreader beam contacting at two points of the beam which are located 300 mm on either side of the center of the beam. The surface of interest for the range cameras and the laser scanners is the top surface of the beam. However, the spreader beam occluded almost half of the beam thereby hindering the capture of full span of the beam. As an alternative method to measuring the top surface of the beam, thirteen white-washed thin aluminum plates of size 2 by 6 inches were firmly attached from the bottom surface of the beam at equal interval of 250 mm.

Four different types of sensors were used for measuring the beam deflection, namely:

- Three 1D laser transducers
- Seven Canon digital cameras (photogrammetric system)
- Two terrestrial laser scanners (Leica HDS6100 and Trimble GS200)
- Two SR4000 range cameras

Each system operates differently. The one-dimensional laser transducers measures the range between the target and the sensor with sub-millimetre accuracy providing real time deflection values. The photogrammetric system composed of multiple medium format digital cameras captures stereoscopic images of the whole span of the beam simultaneously which can be processed using a stereo-vision method to obtain the depth measurement of the target points. The terrestrial laser scanner produces the 3D point cloud of the imaging scene by scanning mechanisms and laser rangefinding. Because the laser scanner technology is a well established method of measuring the structural deformation (Tsakiri et al., 2006; Gordon and Lichti, 2007; Park and Lee, 2007; Lovas et al., 2008; Ronnholm et al., 2009), the TLS measurements will be used as the true measurement for the comparison of the beam deflection measurements from the range cameras. Finally, the range cameras capture 3D information of the scene by ranging and imaging technology.

Figure 5.3 shows the actual structural deformation scene for the first experiment with all the sensors at the zero load position. Laser transducers were placed under the beam at three locations, L/3 (Strip 5), L/2 (Strip 7) and 2L/3 (Strip 9) respectively which are shown in Figure 5.1. A special steel housing frame was built to support the digital cameras and the range cameras. The position of the two range cameras are shown in Figure 5.1. The seven digital cameras were attached to the horizontal steel tubes looking vertically down with four cameras on the left side and three cameras on the right side of the actuator. The two laser scanners were positioned with one at the extreme left end of the beam and the other located

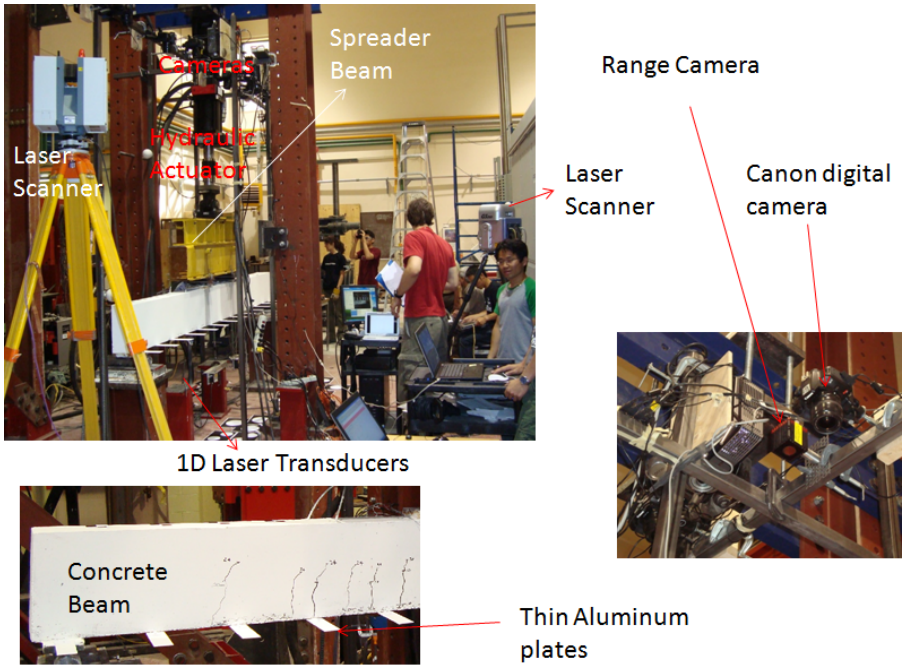

FIGURE 5.3: Structural beam deformation experiment

perpendicular to the center of the beam. The two locations were chosen to optimally capture the whole surface of the beam and the thin plates. The two range cameras were centrally located on either side of the actuator such that the images of the two cameras encompasses the whole length of the beam. Circular targets of diameter 50 and 75 mm were fixed on the floor surface covering the whole FOV of the two range cameras which is to be used for the registration of their point clouds.

The range camera is the interest of this thesis, so only the field operation of the range camera is elaborated further. The integration time was optimally set at 17.2 ms because at this setting the problem of saturated pixels was observed to be minimum for that particular imaging scene. The pixel saturation depends on the distance of the imaging objects from the camera and the reflectivity of the surface. Unlike the SR3000 measurements, the SR4000 outputs null values for the saturated pixels which is not usable for any metric evaluation. So it is important to avoid saturated pixels for the SR4000 as much as possible. Additionally to improve the measurement precision of the range cameras, twenty frames were simultaneously captured for every loading epoch. By averaging the observation of multiple range images the random noise of the range camera is substantially reduced.

The light interference test was performed to investigate the effect of the two similar cameras operating with same modulation frequency of 30 MHz. The location of the cameras were

chosen to capture the full span of the beam with each camera capturing about 50 to 60 % of the beam span. The close proximity of the two range cameras will cause the light from one camera be detected by the other camera and vice-versa. Such detection of additional light will affect the range measurements. This test was conducted on RC 2 because of the unavailability of the operating mechanism during the time of experiment to operate two range cameras simultaneously. When both the cameras are operating at the same time, the light interference bias is prevalent. To avoid the light interference bias, Range Camera 1 (RC 1), which is positioned over the right side of the beam was turned on only during the imaging period of the loading epoch that lasted for less than 10 seconds. Range Camera 2 (RC 2), which is positioned over the left side of the beam was operating continuously. So only RC 2 was able to record measurements without light interference from RC 1.

There were three phases in this experiment. In Phase 1, the load was applied to the beam at the rate of 1 mm stroke of the actuator per minute up to a 3 mm stroke. Then the load was retracted at the same rate to the zero load position. This cycle was repeated for two times in order to test the elasticity of the beam due to small load and deflection. Phase 2 was the main deflection test where the actuator exerted steady force on the beam at the rate of 1 mm stroke per minute up to the point of the failure of the beam. A two minute halt of the actuator after every 5 mm stroke was made to allow for data capture using other sensors besides the laser transducers that were continuously operating. The failure of the beam was observed at the stroke value of 65 mm. Phase 3 was the process of unloading of the applied force to zero after the maximum force was reached during the phase 2 process. This test will indicate the permanent damage caused by the static loading of the phase 2 process. Figure 5.4 shows the three phases of the actual experiment of the concrete beam which took about 2 hours and 10 minutes to complete the test. Two experiments were conducted with

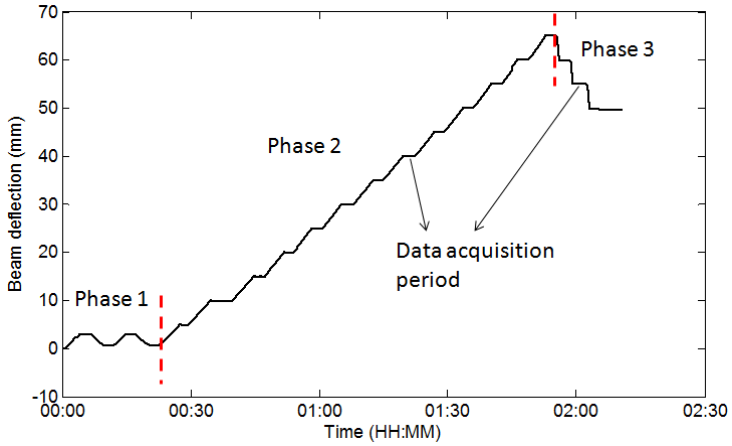

FIGURE 5.4: Concrete beam experiment showing three phases

a similar environment setting and loading procedure. The first experiment was conducted for the concrete beam without the SRP sheets on 21^{st} July and the second experiment was conducted for the concrete beam with the SRP sheets on 22^{nd} July.

5.4 Range Camera Data Processing

This section discusses the data preparation and the image processing techniques used for extracting the point clouds of the thin plates from the point-cloud of the deformation scene. An additional step is introduced to measure the scalar quantity of interest, z-value in the direction of the gravity vector which corresponds to the beam deflection measurement. Since the range cameras do not have in-built levelling mechanisms like the laser scanners, it is difficult to exactly level the range camera during the data capture. The transformation of the range camera point clouds into a levelled surface coordinate system ensures that the measurement of the beam deflection is made along the direction of the gravity vector.

5.4.1 Thin plates point cloud extraction

The range camera produces a collocated range and amplitude image. From the range image, the 3D coordinates of the captured scene can be calculated. Figure 5.5(a) shows the amplitude image captured by the range camera and the Figure 5.5(b) shows the corresponding 3D point cloud of the structural deformation scene.

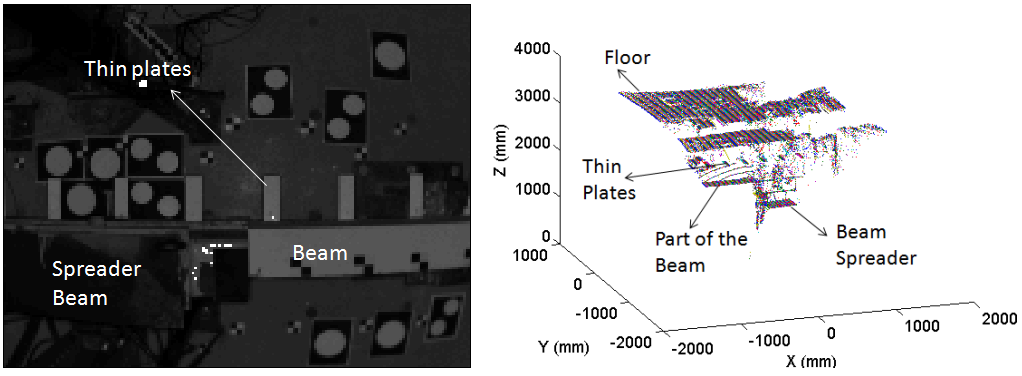

(a) Amplitude image of the deformation scene

(b) Point cloud of the deformation scene

FIGURE 5.5: Image and point cloud of the beam deformation scene

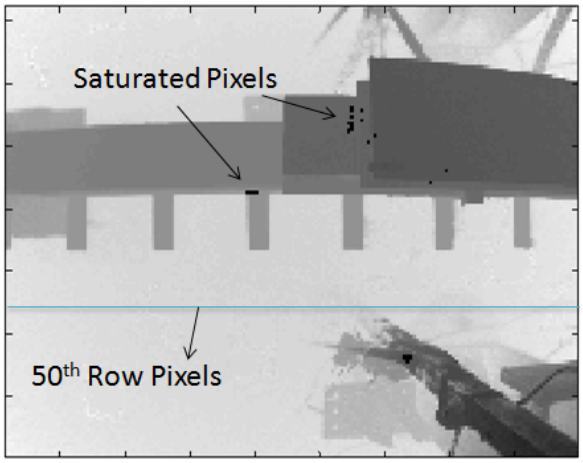

(a) Range image showing 50^{th} row pixels

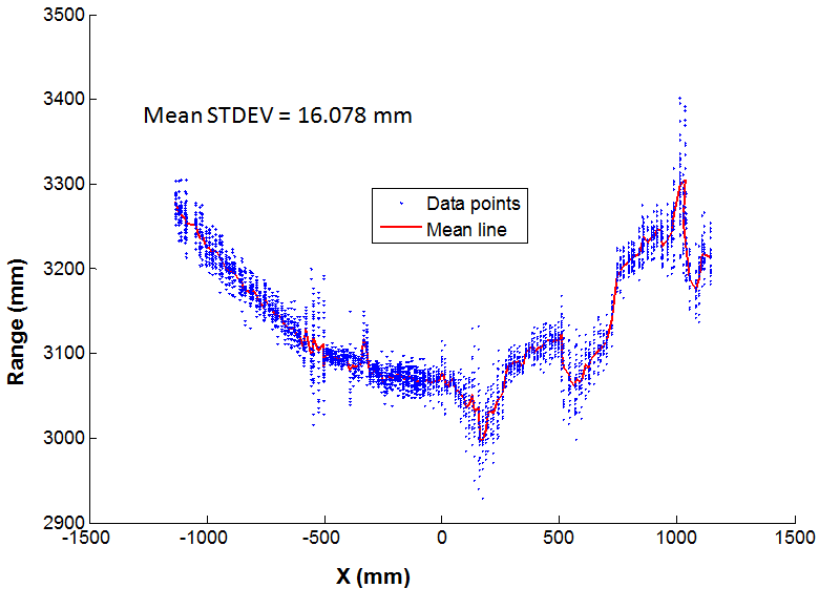

(b) Mean range measurements of the 50^{th} row pixels

FIGURE 5.6: Averaging measurements of twenty images

Figure 5.6(a) shows the range image of the deformation scene with a few saturated pixels and the line marker indicating the 50^{th} row pixels. The saturated pixels are caused by over exposure of the pixels and are recorded as null values in the SR4000 range cameras. These pixels are not usable. That is why the integration time is carefully set to an optimum value during the data capture in order to reduce such nuisance pixels. For simplicity sake, only one row of pixels is analysed to indicate the variation of the range measurements for twenty

consecutively captured images of the same scene. Figure 5.6(b) shows the twenty range measurements of each pixel appearing as a vertical profile of dots and their mean values depicted as a mean line. The mean of the standard deviations of all 176 pixels in the 50^{th} row is 16.078 mm which suggests that the single range image is significantly corrupted by the noise of the sensor. By averaging the measurements of multiple range images, this system noise is considerably reduced and thereby improving the measurement precision of the range cameras. This is an important process towards achieving sub-millimetre precision required for deformation measurements. The bumps in the mean line observed in the left portion of the Figure 5.6(b) are because of the random biases due to multipath and scattering errors caused by the iron pillar located in that side of the imaging scene.

The subjects of interest in the point cloud of the range cameras for measuring beam deflection are the top surface of the beam and the thin plates that are attached to the bottom surface of the beam. Of the two targets of interest, the processing of the thin plates is the most important because of its un-occluded view from the range cameras thereby allowing displacement measurement of the beam at all critical points along the beam span. The top surface of the beam is only visible for a quarter of the beam span at the two ends of the beam from the two range cameras respectively, which is not sufficient to accurately model the deflection of the beam.

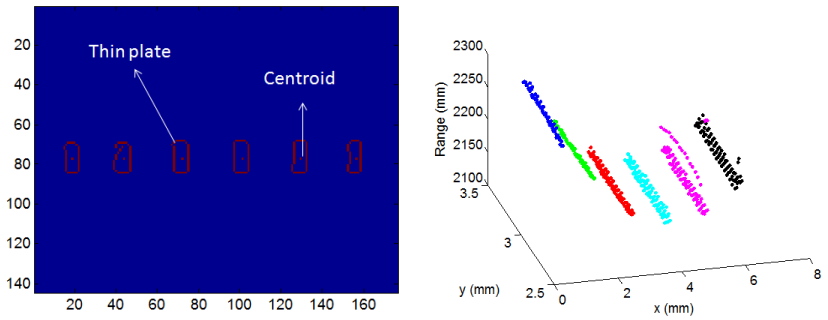

(a) Edge detection of the thin plates

(b) Point cloud of the thin plates

FIGURE 5.7: Edge detection and point cloud extraction of the thin plates

The Canny edge detection operator is used to detect the edges in the amplitude image of Figure 5.5(a). The result of the Canny operator produces a binary image with all the edge information present in the amplitude image. Further removal of the unwanted edges that are not the part of the thin plates is achieved by using a threshold on the eccentricity and the area of the Canny detected regions. Since the detected edges of the thin plates have a similar shape and size, the eccentricity and the area of these desired regions have almost

similar values within close proximity. This similarity of the region of the thin plates is used to segment the desired regions from the unwanted regions. Figure 5.7(a) shows the binary image of the detected edges of the thin plates. Section C.1 of Appendix C shows the MATLAB code used for segmentation of the thin plates using the amplitude image. Using the detected boundary of the thin plates, the point cloud of the thin plates is easily extracted by computing the pixel indices of the inside of the polygon, formed by the detected edge boundary. Figure 5.7(b) shows the corresponding inside point clouds of the respective thin plates.

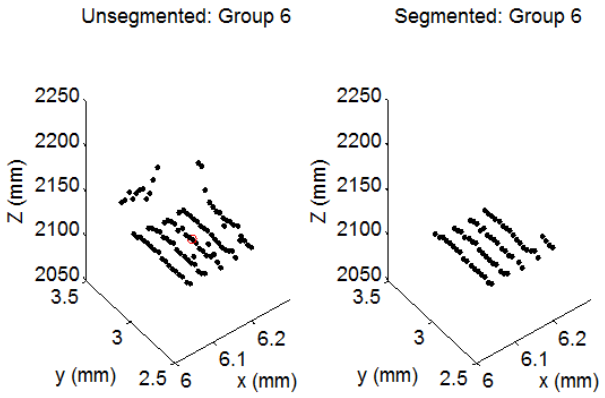

FIGURE 5.8: Further refinement of thin plate point cloud

The extracted point clouds of the thin plates consist of noisy points besides actual points as shown in Figure 5.8 (Left). This noisy points are the mixed pixels occurring at the edges of the thin plates which are caused by the uncertainty in range measurement of the backscattered signals from the foreground and the background targets. The removal of the unwanted noisy points from the thin plate point clouds is achieved by depth based segmentation of the point cloud. The centroid of the clusters is computed which is indicated with a circular mark in the left part of the Figure 5.8. Depth based segmentation is done by computing the lower and upper threshold values in Z from the mean value of the extracted thin plate point cloud. Any points lying outside these thresholds are removed from the cluster to produce a new cluster without noise as shown in the right side of the Figure 5.8.

It is expected for a flat thin plate to have a point cloud with less variation in the Z values, however, it is not the case for the range camera because of the random noise of the system. Normally the point cloud of a small flat surface appears as a cluster with Z value varying within 1 cm or less if no other systematic range biases are present. This refined point clouds of the thin plates are then used to compute the centroid of the plates which is the reference point of interest for measuring the displacement of the beam at each successive measurement epochs.

5.4.2 Alignment of the Z-axis to the gravity vector

The measurement of the deflection of the beam has to be made in the direction of the gravity vector which means that the Z-axis for the range camera has to be aligned as close to the gravity vector as possible. Because the range cameras do not have a built-in leveling system, they were only approximately levelled during the operation. Therefore the coordinate system of the camera needs to be transformed to a levelled surface so that the vertical axis of the camera coordinate system aligns as close to the direction of the gravity vector as possible. This process can be achieved in this test by transforming the range camera coordinates to the locally defined floor surface coordinate system whose perpendicular axis is a better approximation of the gravity vector.

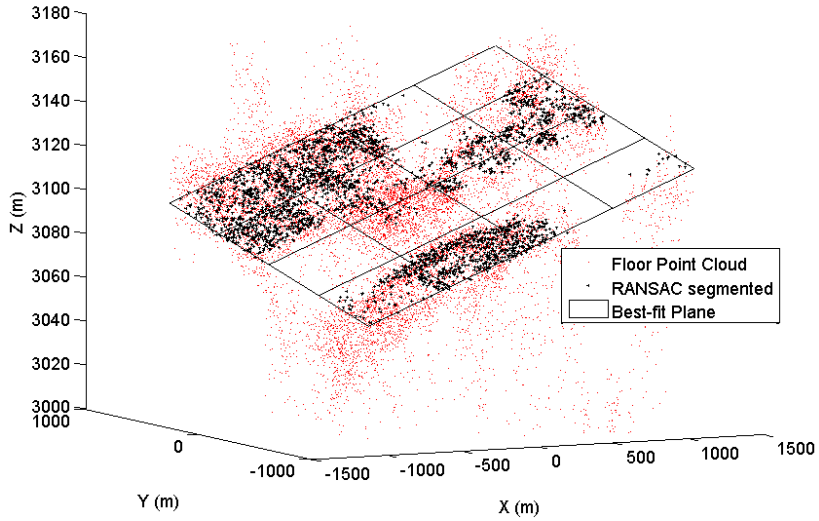

FIGURE 5.9: RANSAC best-fit plane

A simple validation of the parallel alignment of the Z vector of the range camera coordinate system with the gravity vector is done by computing the rotation angles between the range camera coordinate system and the floor coordinate system whose normal vector should approximately represent the gravity vector. This process requires segmenting the point clouds of the floor surface and then fitting a best-fit plane to it. RANSAC (Random Sample Consensus) based segmentation is used for segmenting the point cloud of the planar floor surface. According to Fischler and Bolles (1981), RANSAC is a method for estimating model parameters on a consensus set of inliers which are modified and selected iteratively based on a statistical test thereby effectively removing the data outliers in the process.

Figure 5.9 shows the best-fit plane on the RANSAC based segmented floor points. The floor surface is shown in Figure 5.5(b). It is clearly visible that the actual floor surface of the

point cloud shown in red dots in Figure 5.9 is greatly biased with scene-dependent errors. The biases can be attributed to the systematic errors due to multipath, incidence angle of the reflected light and the scattering artefact which are difficult to model because of the complexities involved in the imaging scene. In the absence of systematic error correction model, it is prudent to use the RANSAC based segmentation method to extract the points of the most likely planar floor surface. The RANSAC algorithm for segmenting a planar patch is discussed briefly in Section C.2 of Appendix C.

The method of eigenvalue decomposition is used to obtain the rotation matrix which can transform the range camera coordinate system to the planar floor coordinate system. The equation of a plane is shown in Equation 5.7, where a, b and c are the coefficients of x-, y- and z-coordinate respectively and d is the orthogonal distance of the plane from the origin.

$$ax + by + cz = d \tag{5.7}$$

The plane fitting can be achieved by the method of orthogonal regression where the minimization function is the sum of the squares of the orthogonal distances to the plane from the data points. That is,

$$\phi_{min} = \sum_{i=1}^{k} [\vec{n}^T (\vec{r_i} - \vec{\bar{r}})]^T \tag{5.8}$$

where $\vec{n} = \langle a, b, c \rangle$ (normal vector), $\vec{r_i}$ is the observation point reduced to the centroid of the set of the planar points, and $\vec{\bar{r}}$ is the point on the plane.

The solution to this minimization function is a problem of eigenvalue-eigenvector decomposition, which requires computing the eigenvalues and the eigenvectors of the covariance matrix (Shakarji, 1998). The covariance matrix of the given set of points is calculated using Equation 5.9

$$C_{3,3} = \frac{1}{k} \sum_{i=1}^{k} (\vec{r_i} - \vec{\bar{r_c}})(\vec{r_i} - \vec{\bar{r_c}})^T \tag{5.9}$$

where $\vec{\bar{r_c}}$ is the centroid of the set of points. The problem of the eigenvalue decomposition of the symmetric, positive-semi-definite covariance matrix, C is given in Equation 5.10

$$C\vec{n} = \lambda\vec{n} \tag{5.10}$$

where λ is a set of eigenvalues. Numerically, the eigenvalues and the eigenvectors can be obtain by decomposing C into two orthogonal matrices, V and D as shown in Equation 5.11

$$C = VDV^T \tag{5.11}$$

where the diagonal entries of the matrix D is the eigenvalues and the column entries of the matrix V are the respective eigenvectors of the corresponding eigenvalue in matrix D arranged in ascending order. The normalized eigenvector corresponding to the smallest eigenvalue is the coefficients of the normal vector. The three column entries of the eigenvector matrix also represents the three cardinal axes of the fitted plane. Further, the entries of the eigenvector matrix are also the direction cosines of the rotation matrix which is also the transformation matrix.

TABLE 5.1: Rotation angles between the range camera and the floor coordinate system

Image No	$\omega(^\circ)$	$\phi(^\circ)$	$\kappa(^\circ)$
Image 1	0.3234	2.0455	-45.2059
Image 2	0.5586	2.022	-53.0919
Image 3	0.2404	2.0022	-44.7819
Image 4	0.3249	2.0599	-46.2763
Image 5	0.2435	2.0203	-43.8161
Image 6	0.2414	2.1093	-43.8016
Image 7	0.4214	2.11	-48.4108
Image 8	0.3263	2.0846	-45.5369
Image 9	0.2517	1.9503	-43.6314
Image 10	0.495	2.0154	-51.6892
Image 11	0.2736	2.0022	-44.6068
Image 12	0.2149	1.9838	-42.4368
Image 13	0.2837	2.1325	-45.2425
Image 14	0.1254	2.0114	-41.762

Table 5.1 shows an example of the three cardinal angles computed from the transformation matrix obtained from the eigenvalue decomposition method for all the fourteen images of the range camera for Experiment 1 Phase 2 experiment of the RC 2. The rotation angles about the X and Y axes indicates the deviations of the range camera coordinate system from the level surface.

5.5 Terrestrial Laser Scanner Data Processing and Accuracy Assessment

The point cloud of the beam and thin plates was manually segmented from the full scanned point cloud. Figure 5.10(a) shows the segmented point cloud of the beam and the thin plates. Using Y and Z value thresholds, the thin plates were segmented from the cluster which is shown in Figure 5.10(b). For each plate, the centroid of the point cloud was computed as the reference point for measuring the beam deflection at the particular instant of the loading epoch. Plates 1 and 13 are marked in Figure 5.10(b) and the other plates are located serially in between the first and the last plates. Unlike the range camera point clouds of the thin plates, the variation in the Z-value of the laser scanner point clouds of the planar thin plates was within 3 mm, which indicates the high point measurement precision of the laser scanner.

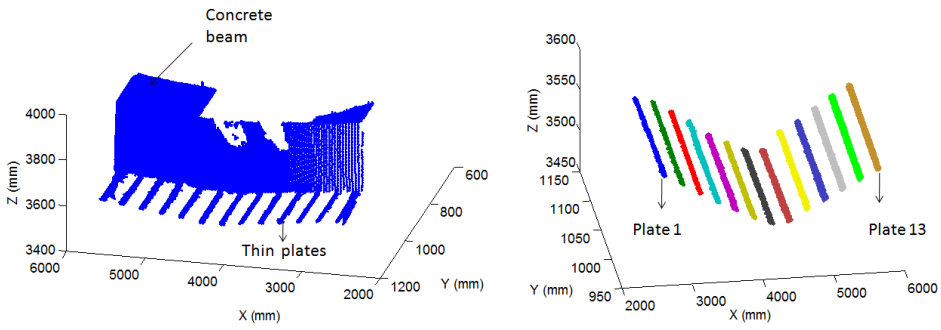

(a) TLS point cloud of the beam (b) Extracted thin plates point cloud

FIGURE 5.10: Automatic extraction of the thin plates from the TLS point clouds

The legend entries are the stroke measurement of the hydraulic actuator. There are 14 loading epochs where the measurement of the beam was done, starting from zero load to the maximum load at the 65 mm stroke with an interval of 5 mm stroke. The laser scanner centroid-based spline-fit deflection curves for the concrete beam experiment are shown graphically in Figure 5.11 whose values are given in Table C.10 in Appendix C. The deflection value (δ Z) at any given measurement epoch is the difference between the actual Z value of the centroid at that measurement epoch and the Z value of the corresponding centroid at the zero load state. The actual Z values of the centroid are given in Table C.9 in Appendix C. The TLS deflection errors along with their standard deviation and RMSE values are given in Table 5.2. These deflection errors are the difference between the deflection measurements of the 1D laser transducer and the TLS whose deflection values are given in Tables C.1 and C.2 respectively in Appendix C. The laser transducer at Strip 5 was placed

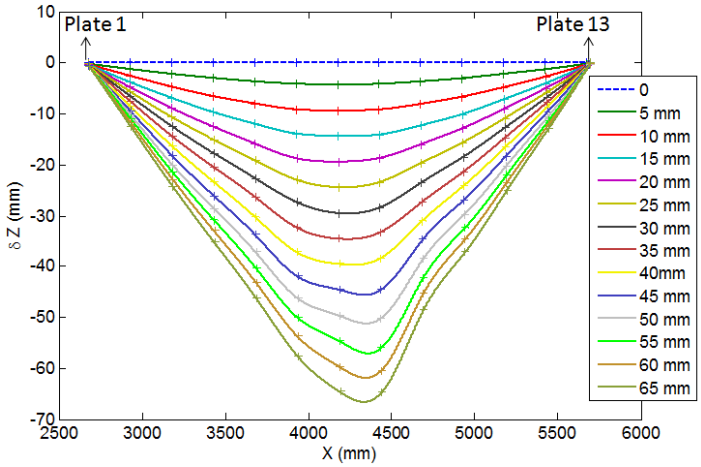

FIGURE 5.11: Centroid-based TLS beam deflection measurement

at short range from the bottom surface of the beam, so it could not measure deflection values after 35 mm stroke for the concrete beam experiment (El-Badry, 2010).

TABLE 5.2: Deflection errors of the TLS

	Concrete Beam			**Polymer Sheet Beam**		
	Strip 5	**Strip 7**	**Strip 9**	**Strip 5**	**Strip 7**	**Strip 9**
5 mm	0.65	0.72	0.64	0.73	0.65	0.51
10 mm	0.69	0.64	0.53	0.82	0.61	0.60
15 mm	1.14	0.70	0.39	0.92	0.52	0.41
20 mm	1.00	0.65	0.56	1.07	0.51	0.56
25 mm	1.54	0.62	0.22	1.26	0.47	0.80
30 mm	-0.42	0.58	-0.17	0.81	0.72	-2.54
35 mm	NA	0.53	-0.36	0.82	0.83	-2.40
40 mm	NA	0.61	-0.35	0.93	0.94	-0.38
45 mm	NA	0.62	-0.51	0.82	0.76	-2.05
50 mm	NA	0.58	-1.04	1.62	1.38	-1.06
55 mm	NA	0.67	-1.72	0.92	1.11	-2.47
60 mm	NA	0.65	-1.94	0.97	1.07	-2.52
65 mm	NA	0.81	-2.04	1.08	1.26	-2.63
Mean	0.77	0.64	-0.44	0.98	0.83	-1.01
STDEV	0.67	**0.07**	0.96	0.24	0.30	1.46
RMSE	0.98	**0.65**	1.03	1.01	0.88	1.73

The point-based comparison is made at three different points (Strips 5, 7 and 9). The Strip 7 is exactly located at the Plate 7 of the TLS data so the deflection errors for this point is a better estimate of the measurement precision and the accuracy of the TLS. For the concrete beam experiment, the TLS measurement precision is 0.07 mm and the RMSE accuracy is 0.65 mm whereas for the polymer sheet beam the measurement precision is 0.30 mm and RMSE accuracy is 0.88 mm. The result for concrete beam is comparably better than the

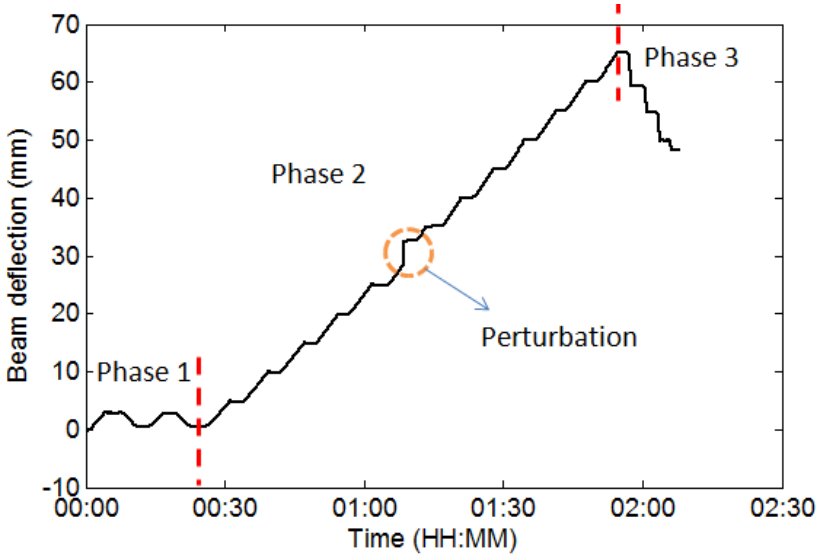

FIGURE 5.12: Polymer beam experiment profile

polymer sheet beam both in terms of precision and accuracy of the TLS measurements because the beam for the second experiment appears to have been moving during the data acquisition period. Figure 5.12 shows the time series plot of the polymer beam experiment where loading perturbation is clearly visible. The perturbation observed at the 30 mm stroke is caused by the separation of the concrete beam from the polymer sheets.

5.6 Zero Load: Repeatability Test

The zero load test was conducted to assess the beam deflection measurement repeatability of the various sensors used for the deformation test. The test was conducted during the Experiment 2. Though two different beams were used for the deformation experiment, one repeatability test is sufficient to analyse the measuring consistency of the range cameras. Three successive scans were captured using the laser scanner. Table 5.3 shows the actual measurement and the differences of the centroid measurement of the three scans along with the standard deviation of the measurement differences of the three epochs. The differences were obtained by subtracting the measurements from one another. The standard deviation of 0.04 mm of the differences between the successive scans indicates a high repeatability of the TLS sensor.

As for the range cameras, three successive images of 20 frames each were captured using the RC 1 and RC 2 at the zero load position of the beam. Tables 5.4 and 5.5 show the

TABLE 5.3: Centroid measurement of the TLS zero load test

	Test1: No Load	**Test2: No Load**	**Test3: No Load**	**Test1-Test3**	**Test2-Test1**	**Test3-Test2**
Plate 1	3550.904	3550.902	3550.884	0.020	-0.003	-0.018
Plate 2	3549.595	3549.616	3549.609	-0.013	0.021	-0.007
Plate 3	3546.917	3546.927	3546.895	0.023	0.009	-0.032
Plate 4	3546.199	3546.228	3546.219	-0.021	0.029	-0.009
Plate 5	3545.721	3545.704	3545.710	0.011	-0.017	0.005
Plate 6	3545.593	3545.566	3545.585	0.008	-0.027	0.019
Plate 7	3537.437	3537.450	3537.431	0.005	0.013	-0.018
Plate 8	3544.146	3544.204	3544.137	0.009	0.058	-0.066
Plate 9	3544.445	3544.443	3544.371	0.074	-0.002	-0.072
Plate 10	3543.898	3543.924	3543.996	-0.098	0.026	0.072
Plate 11	3544.424	3544.483	3544.460	-0.036	0.059	-0.023
Plate 12	3543.800	3543.805	3543.858	-0.058	0.005	0.054
Plate 13	3541.933	3541.921	3541.972	-0.039	-0.012	0.051
				$\sigma =$ **0.038 mm**		

TABLE 5.4: Centroid measurement of the RC 1 zero load test

	Test1: No Load	**Test2: No Load**	**Test3: No Load**	**Test1-Test3**	**Test2-Test1**	**Test3-Test2**
Plate 1	2166.543	2166.313	2166.186	0.357	-0.230	-0.127
Plate 2	2162.004	2162.294	2161.838	0.166	0.289	-0.455
Plate 3	2160.409	2160.188	2159.806	0.602	-0.220	-0.382
Plate 4	2156.767	2156.822	2156.443	0.323	0.055	-0.379
Plate 5	2152.039	2152.228	2152.103	-0.064	0.189	-0.125
Plate 6	2147.807	2148.003	2148.123	-0.316	0.196	0.121
Plate 7	2149.941	2150.346	2150.951	-1.011	0.405	0.605
				$\sigma =$ **0.39 mm**		

actual measurements of the centroid of the thin plates and the measurement differences of the same centroid between two different epochs. The standard deviation for RC 1 and RC 2 are 0.39 and 0.21 mm respectively, which is in the order of magnitude more than the laser scanner. This is expected because of the coarse precision of the range cameras. However the values are less than a millimetre, which is sufficient to meet the accuracy needed for the deformation measurement. Comparatively, the standard deviation of the RC 1 is worse than the RC 2 because of the sub-optimal operation of the RC 1 as it was switched on and off frequently in order to avoid the interference of the two light sources.

TABLE 5.5: Centroid measurement of RC 2 zero load test

	Test1: No Load	**Test2: No Load**	**Test3: No Load**	**Test1-Test3**	**Test2-Test1**	**Test3-Test2**
Plate 7	2164.3521	2164.3381	2164.6005	-0.2484	-0.014	0.2624
Plate 8	2151.1674	2151.0618	2151.0313	0.1361	-0.1056	-0.0305
Plate 9	2146.1375	2145.9337	2145.852	0.2855	-0.2038	-0.0817
Plate 10	2141.5829	2141.851	2141.6524	-0.0695	0.2681	-0.1986
Plate 11	2136.9892	2136.6829	2136.5164	0.4728	-0.3063	-0.1665
Plate 12	2125.4509	2125.5056	2125.4742	-0.0233	0.0547	-0.0314
				σ = **0.21 mm**		

5.7 Experiment 1: Results and Analysis

The beam deflection measurement from the range cameras are compared with the measurements from the terrestrial laser scanner and statistically quantified the closeness of measurements of the two methods. Experiment 1 deals with the deformation test done with the reinforced concrete beam without the SRP sheets. The interference test was only conducted for the Phase 2 experiment as it was the main deformation test. RC 1 captured seven thin plates and RC 2 captured six plates with Plate 7 common between the two range cameras. The Plate 13 falls outside the field-of-view of RC 2. In total, only 12 thin plates have been captured using the two range cameras. The Phase 1, Phase 2 and Phase 3 experiments were carried out consecutively whose results are described as follows.

5.7.1 Phase 1: Initial test

Figures 5.13(a) and 5.13(b) show the Phase 1 test results of the TLS and range cameras respectively. Section C.4 in Appendix C presents the measurements and deflection values of the Phase 1 experiment for both the sensors. The TLS plot in Figure 5.13(a) clearly indicates the ability of this sensor to detect the millimetre level displacement of the beam. The TLS measurements clearly show that even a small external force can cause irreversible beam damage of about 1 mm at the centre of the beam. This small beam displacement is indicated by the shift in position of the zero load curves that are measured when the external force is completely retracted to zero load state from the 3 mm displacement load state. Nevertheless this minuscule displacement of the beam is not accurately detected by the range cameras because of the biases caused by the interference of light from the two range cameras.

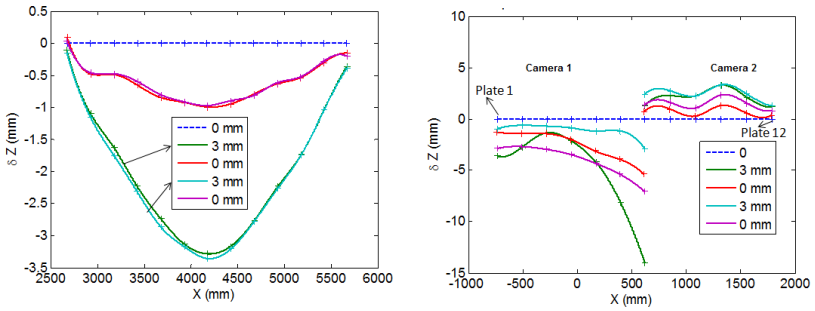

(a) TLS deflection values

(b) Range cameras deflection values

FIGURE 5.13: Phase 1 deflection results

It is also important to note that the measurements of RC 2 increases from 0 to 3 mm displacement while the TLS and RC 1 measurements decreases from 0 to 3 mm displacement, which is reflected by the opposite trend in the deflection values of the two range cameras in Figure 5.13(b). Though the decreasing trend of RC 1 is accurately portrayed as the TLS, yet the deflection measurements are very unrealistic. RC 1 data is doubly affected: firstly, because of the interference of the light; and secondly, this range camera was performing sub-optimally because it was switched on and off periodically during the operation thus this range camera was unable to attain the optimum internal operating temperature in that short period of operation. The unpredictable measurement of the range cameras clearly indicates the low sensitivity of this device which has been overwhelmed by the presence of interference biases. This shows that the range cameras are not sensitive enough to resolve small deformation while in the presence of the systematic and random biases.

5.7.2 Phase 2: Main deformation test

The Phase 2 experiment is the main deformation test where the beam is subjected to a continuous increasing external force at 1 mm deflection of the centre of the beam per minute up to the point of the failure of the beam. The point of the failure of the beam was observed at the nominal displacement value of 65 mm. Figure 5.14 is the plot of the deflection values of the two range cameras. The Z values and the deflection values of RC 1 and RC 2 are given in Tables C.11, C.12 and Tables C.13, C.14 in Appendix C.

Since Plate 7 is common to both the range cameras, the deflection measurement of the two range cameras are supposed to be same. However, there is a difference of within 2 mm (excluding the measurement for the outliers) between the two range cameras. This

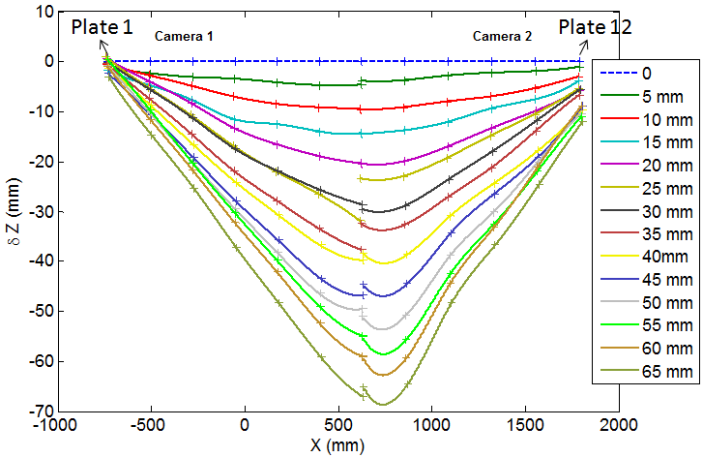

FIGURE 5.14: Centroid-based beam deflection measurement of the range cameras

difference is because of the variable random noise of the individual pixels in the two range cameras, sub-optimal performance of RC 1 and the measurement biases on both the range cameras caused by the interference of the light from the two range cameras. It can be also observed in Figure 5.14 that the spline curves for the 25 mm and the 35 mm for RC 1 deviate significantly from the general trend of the rest of the curves as indicated by the mismatch with the corresponding curves of RC 2. The cause of these outliers may be because RC 1 was switched off in order to avoid the problem of interference between the two range cameras. RC 1 was switched on only for a few seconds during it's data acquisition period at which this range camera may not have completely regained its operating internal temperature for optimal performance.

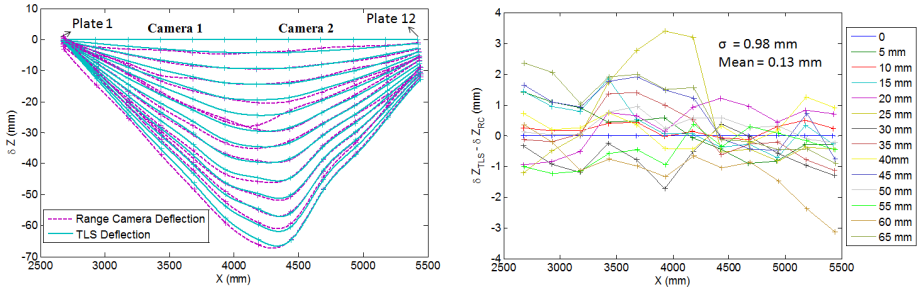

(a) Overlay of the RC and TLS deflection measurements

(b) Errors of the range cameras

FIGURE 5.15: Phase 2 deflection results

Figure 5.15(a) shows the deflection curves of the TLS and the range cameras. The range cameras 1 and 2 are connected at the common Plate 7 simply by averaging their values.

Figure 5.15(b) shows the deflection errors of the the range cameras whose computed values are given in Table C.15 in Appendix C. Table C.15 also shows the standard deviations of the row values for the individual thin plates and and the column values for the different nominal deflection values. The standard deviation for the complete data is 0.98 mm, for RC 1 is 1.02 mm and for RC 2 is 0.82 mm. The measurement precision of RC 1 is lower than RC 2 because RC 1 data is more biased due to periodic turning on and off process of this range camera.

It can be observed in Figure 5.15(b) that there is no visible trend in the errors for all deflection series which clearly indicates the randomness of the deflection errors of the range cameras. Because of the subtraction of the deflection measurements with the initial measurement at the zero load state, most of the systematic biases in the measurements have been reduced considerably by this process. But any form of random noise is still prevalent as it cannot be eliminated by the differencing method. The overall standard deviation of 0.98 mm can be loosely expressed as the precision of the range cameras while in the presence of the interference biases.

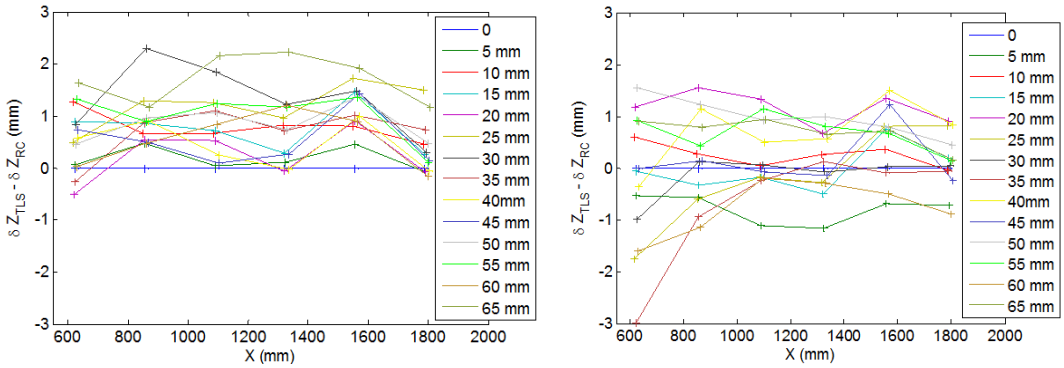

(a) Only RC 2 in operation

(b) Both RC 1 and 2 in operation

FIGURE 5.16: Deflection errors of the RC 2 for the light interference test

Figures 5.16(a) and 5.16(b) show the deflection errors of RC 2 for without and with the light interference bias respectively. While RC 1 was switched off, the RC 2 measurements indicate a presence of constant bias with a mean value of 0.79 mm as the deflection errors in Figure 5.16(a) are displaced one-sided. The constant bias could be attributed to the unmodelled systematic bias such as multipath or scattering errors. It is interesting to observe in this particular experiment that when the RC 1 was in operation, the RC 2 measurements indicate a randomly distributed errors with a mean value of 0.15 mm as depicted in Figure 5.16(b). Somehow strangely the interference of light has removed the constant bias observed in the no-interference case. However the standard deviation for the no-interference case is 0.60 mm

while the standard deviation for the with-interference case is 0.83 mm which indicate the lower precision of the measurements for the with-interference case. It is important to note that the standard deviation of 0.60 mm for the no-interference case is the best measurement result obtained for the range camera for the Phase 2 experiment.

5.7.3 Phase 3: Unloading

The Phase 3 of the experiment was to assess the permanent damage of the beam due to maximum force applied in the Phase 2 experiment causing failure of the beam. The force from the beam was reduced steadily to zero from the maximum force applied in the Phase 2 experiment. The force was decremented at no particular rate.

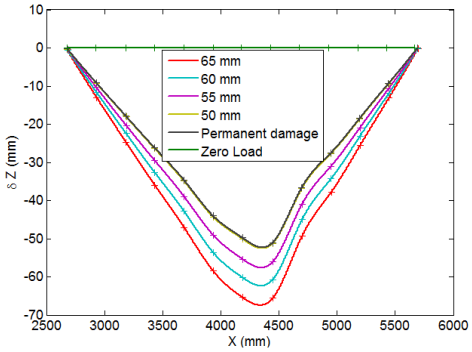

(a) TLS deflection values

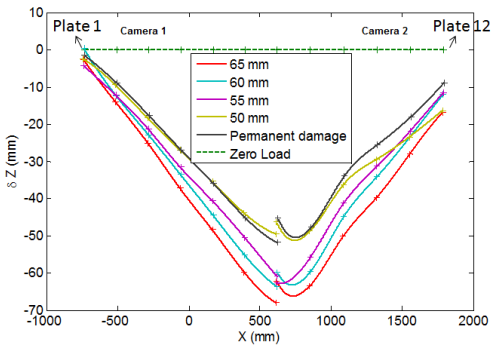

(b) Range cameras deflection values

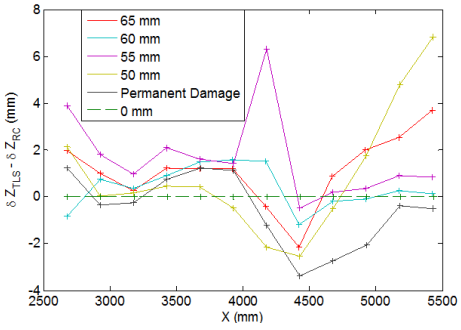

(c) Deflection errors of the range cameras

FIGURE 5.17: Phase 3 deflection results

The result of the Phase 3 experiment for the TLS and the range cameras are shown in Figures 5.17(a), 5.17(b) and 5.17(c) whose deflection values are provided in Section C.6 in

Appendix C. TLS deflection plot in Figure 5.17(a) shows a very consistent trend of the spline curves, while the range cameras's deflection curves in Figure 5.17(b) does not. The standard deviation of the differences in the deflection values between the TLS and the range cameras is 2.85 mm which is significantly higher than the 0.98 mm standard deviation of the Phase 2 deflection results. It is unknown why the range cameras measurements for Phase 3 are worse than Phase 2 as it is expected for these two experiments to at least produce a comparable measurement results. The only difference in the experiment of the Phase 2 and 3 is that the force was steadily applied at constant rate for the Phase 2 experiment while the force was retrieved at an unsteady rate for the Phase 3 experiment. However, the Phase 3 experiment happened very quickly which could have impacted the stability of the beam during the period of data capture.

As per the TLS measurement the reinforced concrete beam is deformed permanently by 49.77 mm as a result of the application of the maximum external force in Phase 2. On the other hand, RC 1 and RC 2 indicate a permanent damage of 48.77 and 46.18 mm respectively which is 1 mm less for RC 1 and 3.55 mm less for RC 2 from the TLS deflection value. The large deflection error of RC 2 is because the internal temperature of the camera may have systematically biased the measurements as it was in operation for more than two hours.

5.8 Experiment 2: Results and Analysis

Experiment 2 deals with the deformation test done for the beam with steel-reinforced polymer sheet. The test field setting for Experiment 2 is similar to Experiment 1. The range cameras were located at the exact position as in the Experiment 1, but TLS was only approximately located on the same point as in Experiment 1 because it was completely removed after Experiment 1 for safety reasons. The Phase 1, Phase 2 and Phase 3 experiments result are discussed in the following sections, with Phase 1 and Phase 2 also have additional results of the no-interference test conducted for RC 2.

5.8.1 Phase 1: Initial test

Figures 5.18(a) and 5.18(b) show the deflection results of the TLS and the range cameras for the Phase 2 experiment respectively. The Z-values and deflection values are provided in Section C.7 in Appendix C. Like in the case for Experiment 1, the TLS measurements are very consistent and reliably detected the small displacements of about 3 mm. The measurements of the range cameras are not consistent and appear to have affected by some

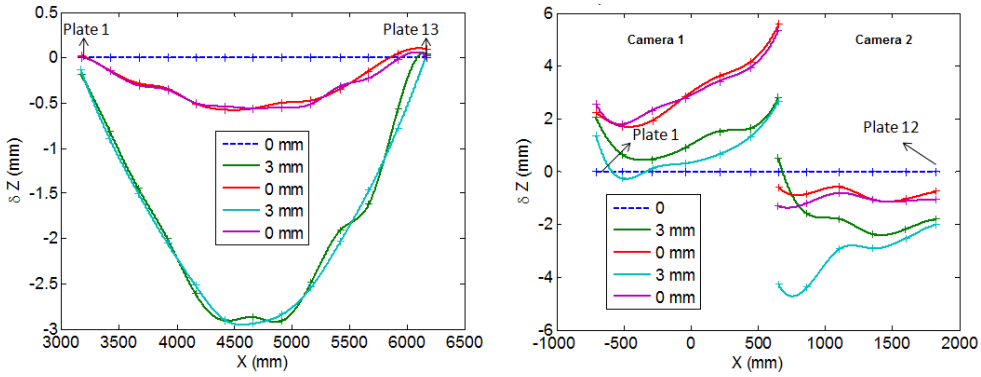

(a) TLS deflection measurements

(b) Range camera deflection measurements

FIGURE 5.18: Experiment 2 Phase 1 deflection results

unmodelled biases. While RC 2 measured the deflection in the same trend as the TLS, RC 1 measurements portrays opposite trend. Recall that, this trend of measurements of the range cameras was vice-versa in Experiment 1. This random measurements biases is attributed to the light interference biases from the two cameras on each other. So while in the presence of additional light sources of same frequency, the measurement of the range cameras are unsystematically affected leading to anomalous measurements.

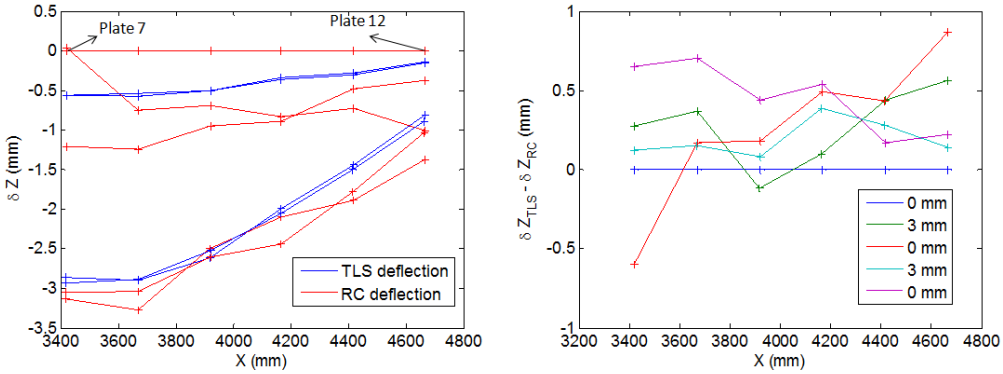

(a) TLS and RC 2 deflection values

(b) Deflection errors of RC 2

FIGURE 5.19: Phase 1 deflection results for the no interference case

On the other hand, the deflection curves of RC 2 measurements in the absence of light interference from RC 1 produces a better result. Figures 5.19(a) and 5.19(b) show the deflection curves overlay of the TLS and RC 2 and the deflection errors of RC 2 respectively when RC 1 was switched off. Table C.25 in Appendix C gives the values of the deflection

errors of RC 2 for all the reference points. The standard deviation and mean of 0.3 mm and 0.29 mm respectively for the deflection errors of RC 2 indicates that the range camera is capable of sensing millimetre level deformation if there are no external biases effecting the phase-shift ToF range measurements. This result also suggests that the range measurements of each range camera is biased by the light interferences from the two range cameras.

5.8.2 Phase 2: Main deformation test

The Phase 2 experiment results for the TLS and range cameras are shown in Figures 5.20(a), 5.20(b) and 5.20(c). The Tables in Section C.8 in Appendix C show the values for the Phase 2 Experiment 2 measurements.

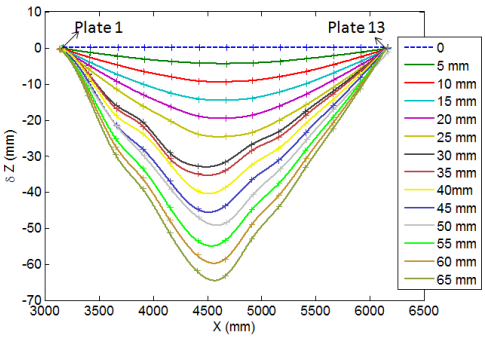

(a) Deflection curves of the TLS

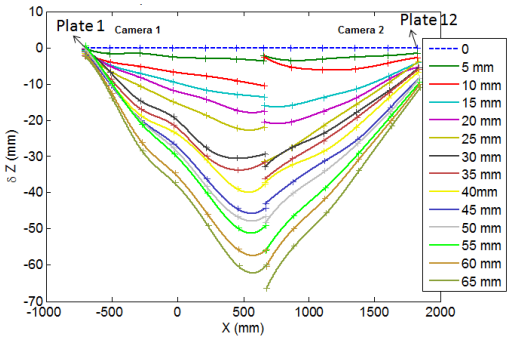

(b) Deflection curves of the range cameras

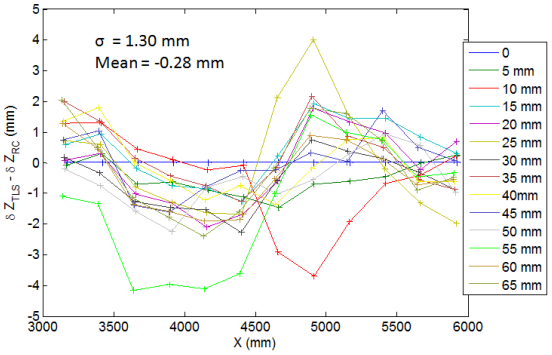

(c) Deflection errors of the range cameras

FIGURE 5.20: Phase 2 deflection results of Exp. 2

While the TLS deflection curves portray a smooth trend in deflection measurements, the deflection curves of the two range cameras are biased with some anomalies. Compared to

the measurements of the range cameras with the concrete beam test, the measurements for this experiment are more biased within the proximity of the common Plate 7. Nonetheless, the shape of the deflection curves for the range cameras closely follows the trend of the curves for the TLS.

The mean and the standard deviation of the deflection errors of the range cameras are -0.28 and 1.30 mm respectively, which is higher than the corresponding values of the Experiment 1. These high values are due to the measurement anomalies within the proximity of the Plate 7 where the effect of the interference of light is more prevalent. Though the experimental conditions were exactly the same for both experiments, it is observed that the interference have affected measurements for the Experiment 2 more than the Experiment 1. This differences in the light interference effects suggests the random nature of the interference biases.

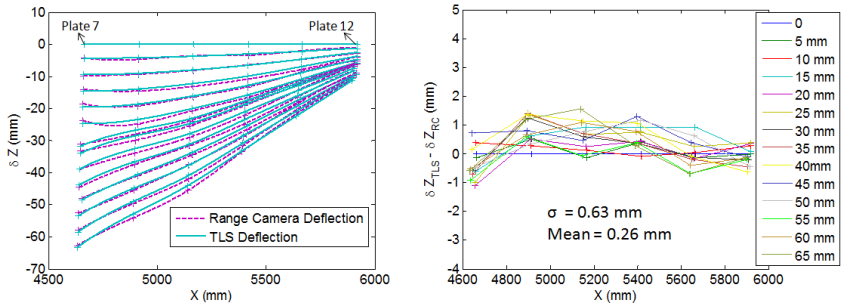

(a) Deflection curves of RC 2 and TLS

(b) Deflection errors of RC 2

FIGURE 5.21: No-interference results of Phase 2 experiment

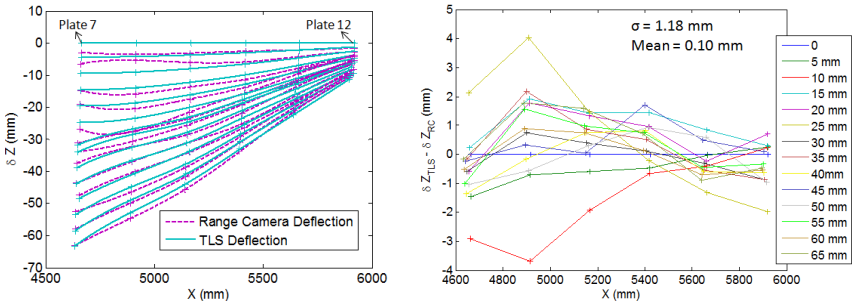

(a) Deflection curves of RC 2 and TLS

(b) Deflection errors of RC 2

FIGURE 5.22: With-interference results of the Phase 2 experiment

Figures 5.21(a) and 5.21(b) show the deflection results of RC 2 while RC 1 was switched off (no-interference), and Figures 5.22(a) and 5.22(b) show the deflection results when RC

1 was switched on (with-interference). The standard deviation of the deflection errors for no-interference and with-interference cases are 0.63 and 1.18 mm respectively. The larger spread in the errors for the with-interference case clearly indicates that the measurement of the RC 2 are biased by the light from RC 1. However the interference biases portrays randomness rather than systematic as it can be vividly observed from the distribution of the errors in Figure 5.22(b) and the low mean value of 0.10 mm. Similar to the results for the concrete beam (without the SRP sheets) experiment, the deflection errors of the RC 2 for the no-interference case portrays a constant bias with a mean of 0.26 mm while the with-interference case portrays a random error. The constant bias for this beam is significantly less than the corresponding value for the concrete beam Phase 2 deflection errors of the no-interference case, while the standard deviation is almost the same.

5.8.3 Phase 3: Unloading

Figures 5.23(a), 5.23(b) and 5.23(c) show the results of the Phase 3 experiment. The Z-values of the centroid and their deflection values are provided in Section C.9 in Appendix C. TLS measurements are consistent while the range cameras measurements are not. The large deviation of the 55 mm curve for the RC 2 was due to low return of the signal from the plates which caused the measured range to be longer than the actual distance. Plate 7 has only a few number of points registered within the limit of the range threshold of the plates. This indicate that the measurements of most of the pixels of this plate are outside the range threshold, which could only be caused by signal attenuation because of scene-dependent errors. Thus it suggests that all the plates were affected at that moment of exposure. The 55 mm curve is excluded from computing the range camera errors (Figure 5.23(c)) as it is an outlier.

Similar to the concrete beam Phase 3 experiment, RC 1 produced a better result than RC 2 in this experiment. However, the overall range camera measurement errors with standard deviation of 1.61 mm and mean of 0.86 mm is beyond the accuracy requirement for sensing the deformation. At the Plate 7 mark, the TLS recorded a permanent damage of the beam of 47.08 mm, while RC 1 and RC 2 recorded 48.19 mm and 43.03 mm respectively. While the RC 1 measurement at the Plate 7 differ by only 1 mm from the TLS measurement, the 5 mm difference of the RC2 measurements do not make any sense. It can only be speculated that the speedy process of retraction of force from the beam in the Phase 3 experiment may have interfered with the data capture, because other experimental settings were exactly same as the Phase 2 experiment.

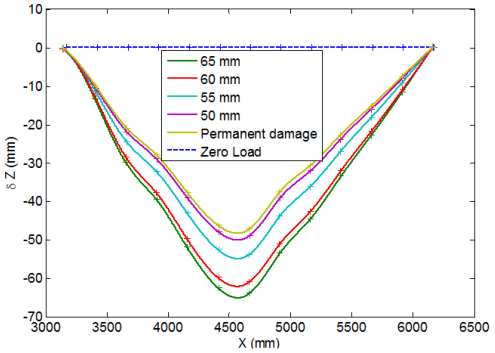

(a) Deflection curves of the TLS

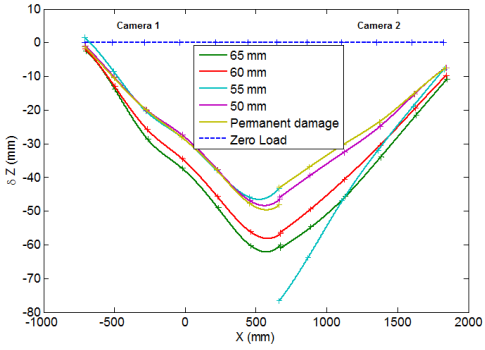

(b) Deflection curves of the range cameras

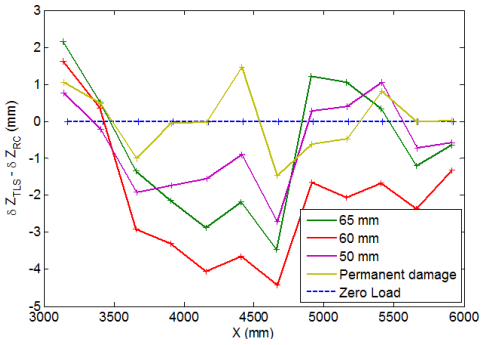

(c) Deflection errors of the range cameras

FIGURE 5.23: Phase 3 deflection results of Experiment 2

5.9 Measurement precision and accuracy of the range cameras

From the experimental results of the two beams, it has been seen that the light interference bias has affected the deflection measurements of the range cameras considerably. Yet, in the presence of the interference bias, the accuracy of the range cameras for the Phase 2 experiment is about 1 mm for the two beams. This measurement accuracy of the range camera is above the accuracy value of 10 mm quoted by the manufacturer. Nevertheless, the Phase 1 and Phase 3 results were not conforming with the Phase 2 results for both Experiment 1 and 2. It is understandable for the Phase 1 experiments because the higher magnitude of interference bias has prevented the range cameras from sensing the smaller deflection value of a maximum 3 mm in this experiment. On the other hand, the Phase 3 experimental results deviate hugely from what is expected at least to conform with the Phase 2 results. Because both the Phase 2 and 3 experiments were measuring larger deflection and

the Phase 3 test was performed immediately after the Phase 2 test with the same settings. However, the Phase 3 test proceeded faster than the Phase 2 test as shown in Figure 5.24. In addition, RC 2 was continuously operating for more than two and half hours (including the warm period of 45 minutes) where the internal temperature of the device may have affected its performance.

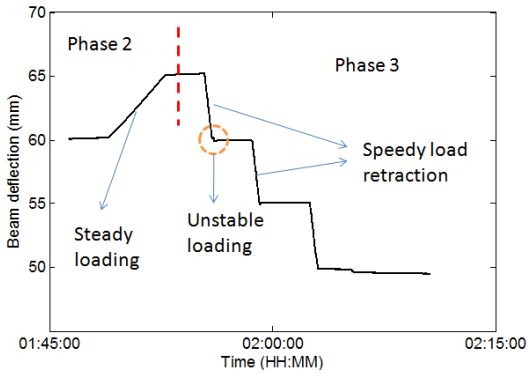

FIGURE 5.24: Phase 3 experiment profile

TABLE 5.6: Measurement precision and accuracy of the RC 2

	with-interference		**no-interference**	
	σ **(mm)**	**RMSE (mm)**	σ **(mm)**	**RMSE (mm)**
Exp. 1 Phase 2	0.83	0.84	0.60	0.99
Exp. 2 Phase 1	1.01	1.06	0.30	0.41
Exp. 2 Phase 2	1.18	1.17	0.63	0.68

The summary of the measurement precision and RMSE values of the RC 2 for the with-interference and no-interference cases are shown in Table 5.6. In all the interference tests reported in Phase 2 experiment of the concrete beam and the Phase 1 and 2 experiments of the beam with steel-reinforced polymer sheet the standard deflection errors are lower than the corresponding values for the with-interference case. Except for the concrete beam Phase 2 experiment, the RMSE values are better for the no-interference case than the with-interference case. The higher RMSE value of 0.99 mm for the concrete beam Phase 2 experiment is due to a constant bias caused by the unmodelled scene-dependent errors such as multipath, incidence angle error and the scattering distortion. On the other hand, even 3 mm displacement of the polymer sheet beam has been sensed by the range camera with measurement accuracy of 0.41 mm which is better than the quoted accuracy of the range cameras by more than an order of magnitude. Therefore the deformation test results suggest that in the absence of the light interference biases the range camera are capable of sensing sub-millimetre level deformation.

5.10 Limitations of the 3D range cameras for Structural Deformation Measurements

Owing to the small field-of-view of the range camera, there was a need to use two range cameras in order to capture the full beam span. Hence there is a need for registration of the two images into a common coordinate system using a common point observations. However, only less than 10% overlap was achieved between the two images where common point observations in this overlap region would provide a weak transformation solution because of weak network geometry. Therefore an alternative method of registration by transforming the coordinates of the two range cameras into a common coordinate system defined by the TLS system is used. High contrast white circular targets on black background were glued on the surface of the floor covering the complete FOV of the two range cameras which were used independently for the two range cameras to transform it's point clouds into the TLS coordinate system.

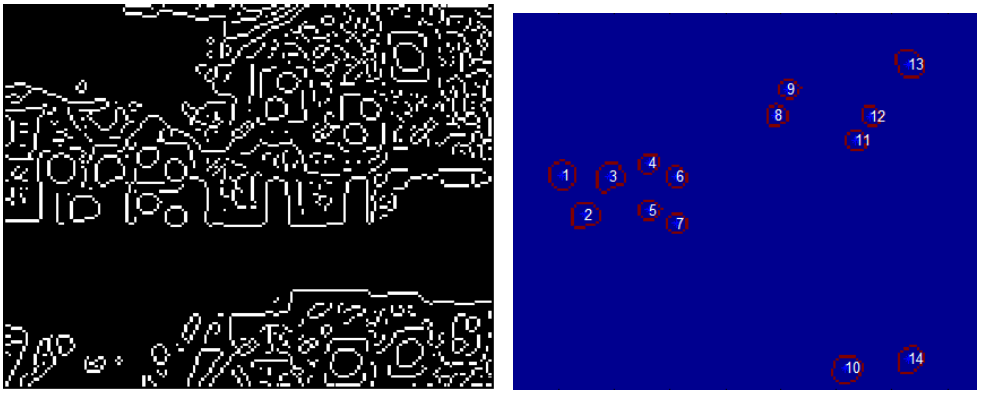

(a) Canny edge detection of the floor surface

(b) Only circular targets

FIGURE 5.25: Extraction of the circular targets

Figures 5.25(a) and 5.25(b) show the Canny-detected edges of the floor surface and the extracted circular targets from the amplitude image of the range camera respectively. An image processing technique similar to the one described in Section 5.4.2 was used to extract the point clouds of the circular targets. The point cloud and the corresponding least squares circle fitting is shown in Figure 5.26.

Figures 5.26(a) and 5.26(b) show the 2D view and 3D view of the 3D circle-fitting of the point cloud of one circular target. This clearly indicates that the 3D circle fit is biased by the large variation in the Z values of the point clouds of the circular targets. The Z values

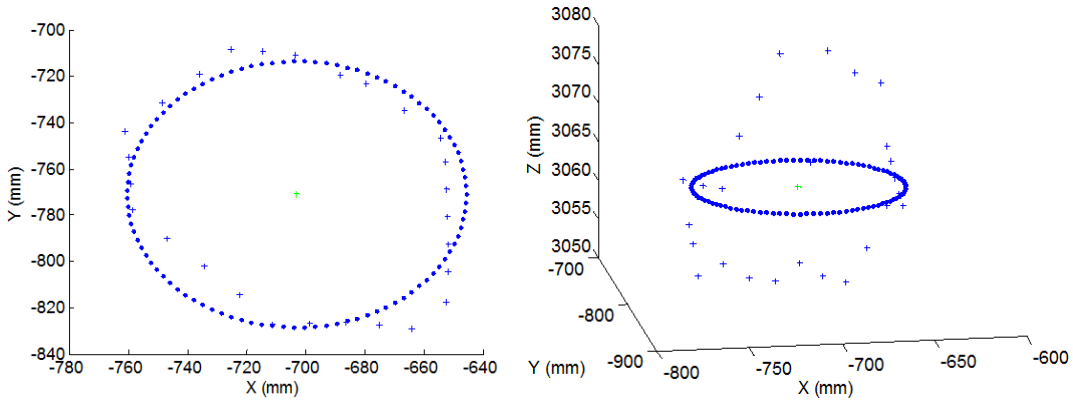

(a) 2D circle fit

(b) 3D circle fit

FIGURE 5.26: Circle fit of the range camera target

of the circular targets varied from 1 to 1.5 cm. This variation of the Z value is indicative of the presence of random biases in the range observations of the range cameras which are difficult to rectify because of the complexities of the occurrence of such range biases. The random biases may be the result of the difference in the reflectivity of the white and black surfaces of the circular targets at the edge of transition.

A terrestrial laser scanner was used to define the coordinates of all the circular targets in the TLS coordinate system. Then the point clouds of the range cameras were transformed into the TLS coordinate system by 3D rigid body transformation using the common points observation of the circular targets. The 3D rigid-body transformation fit was poorly adjusted which is solely due to the coordinate biases of the circular targets of the range camera. While the surface of the targets coordinated by the TLS varied by only 3 mm in the Z value, it varied by about 23 mm for the range camera. Despite the variation in Z value of the range camera is larger than the TLS, the transformation was poorly fitted in the X and Y coordinates. On further investigation, it was found out that the planimetric coordinates of the range camera are almost an order of magnitude worse than the z-coordinate.

The length of the beam as per the TLS measurement is 3005.64 mm as shown in Table C.40 in Appendix C which is 5 mm excess of the actual length of 3000 mm measured by the measuring tape. Thus the highly accurate TLS measurements is the reference for comparison for the range camera measurements. A taped measurement of 25 cm was used to position the thin plates at the bottom surface of the beam. Figure 5.27 shows the actual measurements of the distance between the centroid of the thin plates using the range cameras and TLS. Table 5.7 shows the measurements of the distance between two consecutive thin plates using two

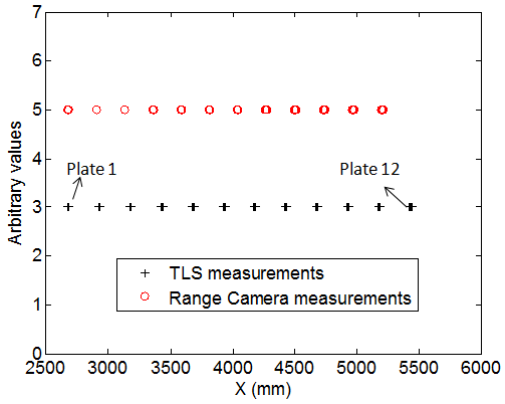

FIGURE 5.27: X-coordinate of the thin plates

TABLE 5.7: Measurement accuracy of the distance between the thin plates

	TLS (mm)	**Range Cameras (mm)**
P2-P1	255.06	197.09
P3-P2	256.08	229.52
P4-P3	246.21	245.86
P5-P4	252.12	251.98
P6-P5	252.75	234.99
P7-P6	253.00	207.05
P8-P7	248.32	212.79
P9-P8	250.58	240.68
P10-P9	246.88	249.96
P11-P10	251.78	248.00
P12-P11	250.13	221.86
Mean	251.17	230.89
STDEV	3.15	18.87

different sensors. While the TLS measurements are very accurate and consistent, the range camera measurements are not. The measurement standard error of TLS and range camera are 3.15 and 18.87 mm respectively, which indicates a very low measurement precision of the range camera. The mean distance between the plates are 251.17 and 230.89 mm for the TLS and the range camera respectively, where the length error of the range camera is about 20 mm and TLS is only 1 mm. This error in lateral coordinates is true only for the small distance between the plates. It can be observed that the lateral distance error increases as a function of distance.

Table C.41 in Appendix C shows the error of the range camera measurements of different plates as a function of distance from Plate 1. At Plates 2,7 and 12 the measurement errors

are 23.75, 142.49 and 225.83 mm respectively. These errors indicate that the lateral measurement errors increases as a function of the distance. These substantial errors in lateral coordinates are the cause of the failure of the rigid-body transformation of the point clouds of the range cameras at the required level of accuracy. The poor root mean square values in the x-and y-coordinates (observed up to 60 mm) of the transformation is directly a result of the low accuracy of the range camera lateral coordinates.

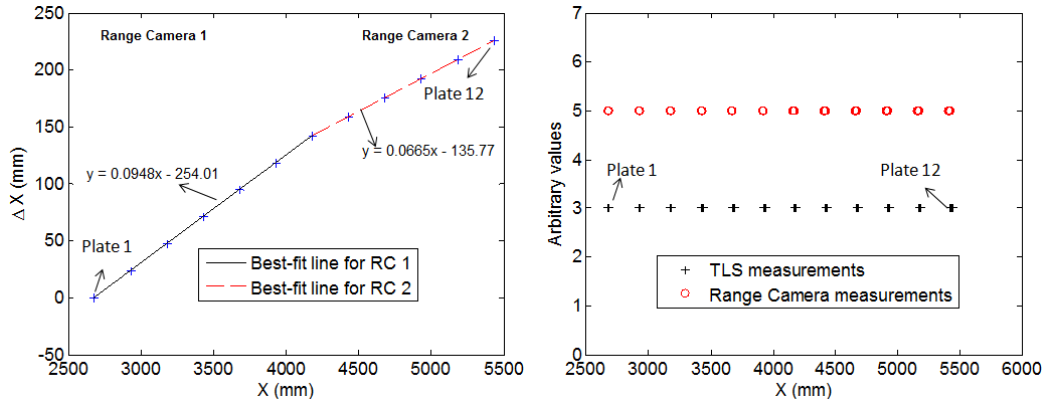

(a) Scale factor error determination

(b) Corrected x-coordinates of the range cameras

FIGURE 5.28: Scale factor error correction

It can be clearly observed in Figure 5.28(a) that the distance errors between the range cameras and the TLS is a scale factor error, which is caused by the systematic biases on the range observations of the range camera. The slopes of the best-fit line are the scale factor for the two range cameras that has to be corrected to their respective x-coordinates. The corrected x-coordinates of the range cameras are shown in Figure 5.28(b). After accounting for the scale factor error, the transformation errors are 6.511, 7.359 and 1.995 mm for x-, y- and z-coordinates respectively which is well within the noise of the camera. Still these transformation errors are too big to exactly register the point clouds of RC 1 and RC 2 to within the sub-millimetre accuracy requirement for the deflection measurements.

However, the lateral coordinates do not effect the Z values which is the only crucial parameter to sensing the relative deformation between the measurement epochs.

5.11 Summary

This chapter has presented the quantitative and qualitative analysis of the beam deflection measurement using the range cameras. The potential of the range cameras has been explored by deploying this measurement sensor for detecting millimetre level deformation of structural beams. Often there are instances where this device failed to sense the deformation reasonably, like in the case for the Phase 1 experiments. Even for the large deformation measurements, some deflection curves like the ones observed for the Phase 3 experiments are biased with random errors that could not be accounted for. In spite of these anomalous measurements observed for the Phase 1 and Phase 3 experiments, the range cameras did accurately sense the displacement measurement of the beams for the Phase 2 experiment with a standard errors of 0.98 mm for the concrete beam and 1.30 mm for the beam with steel-reinforced polymer sheet. It is a very satisfactory result for the range cameras to detect millimetre level deformation even in the presence of the systematic and random biases due to the interference of light from the two range cameras.

In the absence of the light interference, it has been observed that even a 3 mm deformation was detected with a standard error of 0.3 mm using RC 2 for the Phase 1 Experiment 2 case. Surely, this result suggests that the coarse resolution range cameras are highly capable of sensing the deformation especially in vertical direction because of the precise range observations. On the contrary, it has been found that the accuracy of the lateral measurements in x- and y- axes are unacceptable for high precision metric applications. So there is a requirement for further refinement of the calibration model to correct for the lateral coordinate distortions of the range camera.

Chapter 6

Conclusions and Recommendations

The RIM cameras are a state-of-the-art imaging technology where the 3D information of the scene can be captured without the use of any mechanical motors like in the laser scanners. Such a technology is possible because of the miniaturization of the semiconductor technology and the evolvement of the CCD/CMOS processes that can be implemented independently for each pixel. The distance to the target is measured by the continuous phase-shift time-of-flight method. This camera can not only capture static scene but is also able to capture dynamic scenes at video rate which has been not possible with the 3D laser scanning system, SV system and 1D laser transducer. With such a range measurement device, it is possible to achieve various static and dynamic range-based applications which were not possible with the aforementioned imaging systems. Or at the least the range cameras could prove to be a simple and direct alternative to using the conventional stereo-vision system for 3D imaging applications. However this camera suffers from significant geometric and radiometric distortions due to the presence of scene-independent and scene-dependent errors thereby limiting their use for only low accuracy metric applications. Nonetheless the future of the RIM cameras looks brighter due to further progress in the semiconductor technology and ever increasing research interest with respect to these cameras. Unless the lock-in-pixel technology is further developed to achieve a high SNR, it may be impossible to force an under performing measuring sensor to sense measurements at the tenth of a millimetre level. However, this project has shown that under favourable imaging conditions the RIM cameras can be used for structural deformation measurement, achieving measurement precision and accuracy within a millimetre.

6.1 Conclusions

In Chapter 3, the calibration of the range camera was investigated qualitatively and quantitatively. The standard camera distortions can be easily modelled using the collinearity equations augmented with the standard lens distortion terms. However some of the rangefinder biases are difficult to accurately model because of the presence of the scene-dependent biases such as the multipath error, angle of incidence error and scattering artefact. Nevertheless, much research is underway for developing a RIM camera calibration model either using a one-step self-calibration approach or a two-step photogrammetric adjustment. It has been successfully shown that both these methods can produce similar accuracy for the calibration of the range camera in spite of the fact that the high correlation between the lens model parameters and the rangefinder model parameters are a cause of concern for estimation of the parameters in the integrated self-calibration method.

One main problem of the self-calibration model is the ambiguity posed by over parameterisation. This problem of model identification is a serious cause of concern because of the possibility of wrongfully determining the set of model parameters which may not be accurately defining the physical basis of the calibration model. Therefore, a statistical method of model identification known as the Akaike Information Criterion was proposed for model identification in the integrated self-calibration bundle adjustment where large number of model parameters are involved in the physical model. Using the AIC method, the uncertainty in model identification has been greatly reduced from 30 candidate models to three models for the SR3000 case and from 10 models to 2 models for the SR4000 case. Based on the AIC selection procedure, the optimal calibration model for the SR3000 and the SR4000 range cameras involve ten and nine parameters respectively.

In Chapter 4, the effects of the scattering errors in the range and amplitude observations were presented for both the SR3000 and SR4000 range cameras using a simple two planar-objects experiment. It has been unambiguously shown that the scattering induced biases are scene-variant and non-linear, unlike the linearity and the shift-invariance assumption of the liner system model. The scattering errors depend on the position and the size of the scattering objects. In the presence of a large foreground object at a closer distance, the scattering-induced range bias can reach up to 2500 mm on the range measurement of the background objects. Empirically, it is being found that the scattering-induced range error is highly dependent on the surface area of the scattering object and the distance of the scattering object from the camera and the background scene. However, the scattering range bias is invariant with respect to the integration time used to capture the scene.

Two analytical scattering compensation model for scattering scenes having planar surfaces were presented with success rate above 60%. Both Model I and Model II are pixel-wise scattering compensation model which uses the scattering data to interpolate a new correction surface by cubic spline interpolation method. Model I produces better result than the Model II, however, it cannot be used for global prediction of the scattering compensation. Model II can be used for general prediction at different distances for different surface area of the scattering object, but it requires dense scattering data in order to improve the accuracy of the spline interpolation.

Furthermore, it has been observed that the SR4000 is less prone to the scattering errors by an order of magnitude less than the SR3000 range camera.

In Chapter 5, the quantitative and qualitative analysis of the beam deflection measurement using the SR4000 range camera was presented. The potential of the range cameras has been explored to the extreme limit by deploying this measuring device for detecting the millimetre level deformation. Often there were instances where this device failed to sense the deformation reasonably, like in the case for the Phase 1 and Phase 3 experiments. In spite of these anomalous measurements observed for the Phase 1 and Phase 3 experiments, the range cameras did accurately sense the displacement measurement of the beams for the Phase 2 experiment with a standard errors of 0.98 mm for the concrete beam and 1.30 mm for the beam with the steel-reinforced polymer sheet. These are very satisfactory results for the range cameras to detect millimetre level deformation even in the presence of the systematic biases due to the interference of light from the two range cameras.

In the absence of the light interference, it has been observed that even 3 mm deformation was detected with a standard error of 0.3 mm using RC 2 for the Phase 1 Experiment 2 case. For the concrete beam (without the SRP sheets) Phase 2 experiment, it has been observed that the standard error of the deflection errors of RC 2 reduced to 0.60 mm from 0.98 mm while in the absence of the light interference from RC 1. Similarly, for the beam with the SRP sheets the standard error is reduced to 0.63 mm from 1.18 mm. Surely, the results of RC 2 while in the absence of light from RC 1 suggests that the coarse resolution range cameras are highly capable of sensing the deformation especially in vertical direction because of the precise range observations. Conversely, it has been found that the lateral measurements in X- and Y- axes are affected by large scale factor error. The scale factor error in plannimetric coordinates is too big to be acceptable for high precision metric applications.

6.2 Recommendations for future work

The main goal of this thesis is to work towards achieving "*more and more precise measurements*" using the 3D range cameras. The task of measuring beam deflections requires sub-millimetre precision in order to reliably analyse the integrity of the structural members under external loading conditions. The use of the SR4000 range camera in structural deformation measurements in this thesis has shown that even the coarse resolution range camera with ±1 cm distance accuracy as per the specification of the manufacturer can reliably be used for sensing up to a third of a millimetre precision. However, such a high performance can be attained only with careful planning of the imaging environment where the possibility of all sources of systematic biases has to be eliminated completely from the imaging scene. Especially, the multipath effect due to external light reflection from the cornered objects, scattering artefact due to the presence of highly reflective foreground objects and the light interferences from another range camera has to be minimal or completely avoided from the imaging scene. Further recommendations as per the experiences of this work are as follows.

The work herein only involved in measuring the structural deformation of a static scene. However, the RIM sensors are capable of capturing dynamic scenes up to 54 frames per second which can be used for analysing the dynamics of the structural deformation. Such dynamic beam deflection profiles could further assist in understanding the subtle characteristics of the structural members and the joints while subjected to the external forces. Such an understanding could further assist in health monitoring of the structures for safety and serviceability purposes. Additionally, the range camera is capable of surface reconstruction with acquired 3D point clouds. This can provide highly accurate surface models of the deforming scenes which could be more accurate than the point-based models used in this thesis. Therefore, any future experiment must accommodate larger surface capture of the beam in order to reliably use for deflection analysis.

It is always the goal of a photogrammetrist or a metrologist to perfectly calibrate the measuring sensors so that the high-precision mensuration task can be attained reliably and successfully. While calibration can be perfectly achievable for well developed sensors like the standard cameras, it is quite a problem to perfectly calibrate the RIM cameras owing to scene-dependent errors which are highly dependent on the imaging scene environments. Even the calibration model presented in Chapter 2 could only calibrate up to RMSE accuracy of 7.9, 20.4 and 5.0 mm in X-, Y- and Z-coordinates respectively for the SR3000, and 18.4, 14.1 and 4.9 mm in X-, Y- and Z-coordinates respectively for the SR4000 range cameras. The average error in X-coordinates of 20 mm for the distance between the two consecutive target plates between the TLS and the range camera measurements substantiated

the calibration results which indicated 18 mm error for the x-coordinate. This magnitude of error values in plannimetric coordinates is substantially high for a mensuration device which are seemingly capable of measuring the Z deflection values with a precision of third of a millimetre. Therefore, it is very essential to continue working towards a better calibration model in the future. Without improvement in the calibration aspects of the range camera, it cannot be independently used for high-precision metrology applications.

References

Ahn, S. J., Warnecke, H. J. and Kotowski, R. (1999), 'Systematic geometric image measurement errors of circular object targets: mathematical formulation and correction', *Photogrammetric Record* **16**(93), 485–502.

Akaike, H. (1974), 'Information theory and an extension of the maximum likelihood principle', *IEEE Transactions on Automatic Control* **19**(1), 716–723.

Beder, C. and Koch, R. (2007), Calibration of focal length and 3d pose based on the reflectance and depth image of a planar object, *in* 'Proceedings of the Dynamic 3D Imaging Workshop', September, Heidelberg.

Beer, F. P. and Johnston, E. R. (1992), *Mechanics of materials*, McGraw-Hill, New York, USA.

Blais, J. A. R. (1981), 'On some model identification strategies using information theory', *Manuscripta Geodaetica* **16**(5), 326–332.

Boehm, J. and Pattinson, T. (2010), Accuracy of exterior orientation for a range camera, *in* 'International Archives of Photogrammetry, Remote Sensing and Spatial Information Sciences', Vol. XXXVIII, pp. 103–108.

Bostelman, R. and Albus, J. (2007), A multipurpose robotic wheelchair and rehabilitation device for the home, *in* 'Proceedings of the IEEE International Conference on Intelligent Robots and Systems', Oct. 29 -Nov. 2, San Diego, California, USA. http://ieeexplore.ieee.org.ezproxy.lib.ucalgary.ca (accessed 12 Feb. 2010).

Bostelman, R., Hong, T., Madhavan, R. and Weiss, B. (2005), 3d range imaging for urban search and rescue robotics research, *in* 'IEEE International Conference on Systems Safety, Security and Rescue Robotics', http://ieeexplore.ieee.org.ezproxy.lib.ucalgary.ca (accessed 01 Feb. 2010).

Bostelman, R., Russo, P., Albus, J., Hong, T. and Madhavan, R. (2006), Applications of 3d range camera towards healthcare mobility aids, *in* 'Proceedings of the IEEE International Conference on Networking, Sensing and Control', 23-25 April,Florida, USA. http://ieeexplore.ieee.org.ezproxy.lib.ucalgary.ca (accessed 12 Feb. 2010).

Breuer, P., Eckes, C. and Mller, S. (2007), Hand gesture recognition with a novel ir time-of-flight range camera-a pilot study, *in* 'Proceedings of the Mirage 2007, Computer Vision/-Computer Graphics Collaboration Techniques and Applications', 28-30 March, Rocquencourt, France.

Burnham, K. P. and Anderson, D. R. (2002), *Model selection and inference: a practical information-theoretic approach*, second edn, Springer-Verlag, New York, USA.

Buttgen, B., Oggier, T., Lehmann, M., Kaufmann, R. and Lustenberger, F. (2005), CCD/CMOS lock-in pixel for range imaging: Challenges, limitations and state-of-the-art, *in* 'Proceedings of the 1st Range Imaging Research Day', ETH Zurich, Switzerland.

Chiabrando, F., Filiberto, R., Piatti, D. and Rinaudo, F. (2009), 'Sensors for 3d imaging-metric evaluation and calibration of a ccd/cmos time-of-flight camera', *Sensors* **9**(12), 80–96.

Chiabrando, F., Piatta, D. and Rinaudo, F. (2010), Sr-4000 time-of-flight camera: Further experimental tests and first applications to metric surveys, *in* 'International Archives of Photogrammetry, Remote Sensing and Spatial Information Sciences', Vol. XXXVIII, pp. 149–154.

D'Errico, J. (2005), Matlab central file : Surface fitting using gridfit, http://www.mathworks.com/matlabcentral/fileexchange/8998 (accessed 15 Aug. 2010).

Du, H., Oggier, T., Lustenburger, F. and Charbon, E. (2005), A virtual keyboard based on true-3d optical ranging, *in* 'Proceedings of the British Machine Vision Conference', 5-8 September, Oxford, England.

El-Badry, M. (2010), Load deflection diagrams, [email] (Personal communication, 4 August 2010).

Ellekilde, L., Huang, S., Miro, J. A. and Dissanayake, G. (2007), 'Dense 3d map construction for indoor search and rescue', *Journal of Field Robotics* **24**(1), 71–89.

Falie, D. and Buzuloiu, V. (2007), Noise characteristics of 3d time-of-flight cameras, *in* 'International Symposium on Signals, Circuits and Systems', 13-14 July, Iasi, Romania.

Falie, D. and Buzuloiu, V. (2008a), Further investigations on time-of-flight cameras distance errors and their corrections, *in* '4th European Conference on Circuits and Systems for Communications', 10-11 July, Bucharest, Romania. http://ieeexplore.ieee.org (accessed 15 Aug. 2010).

Falie, D. and Buzuloiu, V. (2008b), Wide range time of flight camera for outdoor surveillance, *in* 'Microwaves, Radar and Remote Sensing Symposium', 22-24 September, Kiev, Ukraine. http://ieeexplore.ieee.org.ezproxy.lib.ucalgary.ca (accessed 12 Feb. 2010).

Fischler, M. A. and Bolles, R. C. (1981), 'Random sample consensus: a paradigm for model fitting with applications to image analysis and automated cartography', *Communications of the ACM* **24**(6), 381–395.

Fraser, C. S. (1997), 'Digital camera self-calibration', *ISPRS Journal of Photogrammetry and Remote Sensing* **52**, 149–159.

Fraser, C. S. and Riedel, B. (2000), 'Monitoring the thermal deformation of steel beams via vision metrology', *ISPRS Journal of Photogrammetry and Remote Sensing* **55**(1), 268–276.

Fuchs, S. and May, S. (2007), Calibration and registration for precise surface reconstruction with tof cameras, *in* 'Proc. of the Dynamic 3D Imaging Workshop', 11 September, Heidelberg, Germany.

Gill, J. and King, G. (2004), 'What to do when your hessian is not invertible? alternatives to model respecification in nonlinear estimation', *Sociological Methods and Research* **33**(1), 54–87.

Gonzalez, R. C. and Woods, R. E. (2008), *Digital Image Processing*, third edn, Pearson Prentice Hall, Upper Saddle River, NJ.

Gordon, S. J. and Lichti, D. D. (2007), 'Modeling terrestrial laser scanner data for precise structural deformation measurement', *Journal of Surveying Engineering* **133**(2), 72–80.

Greiner, G., Loos, J. and Wesselink, W. (1996), 'Data dependent thin plate energy and its use in interactive surface modeling', *Computer Graphics Forum* **15**(3), 175–185.

Guomundsson, S., Aanaes, H. and Larsen, R. (2007), Environmental effects on measurement uncertainties of time-of-flight cameras, *in* 'International Symposium on Signals, Circuits and Systems', Vol. 1, pp. 1–4.

Hansen, D. W., Larsen, R. and Lauze, F. (2007), Improving face detection with tof cameras, *in* 'Proceedings of IEEE International Symposium on Signals, Circuits and Systems', 12-13 July, Iasi, Romania.

Hibbeler, R. C. (2008), *Mechanics of Materials*, 7 edn, Pearson Printice Hall, New Jersey,USA.

Hussmann, S., Ringbeck, T. and Hagebeuker, B. (2008), *Stereo Vision*, In-Teh, chapter 7: A Performance Review of 3D TOF Vision Systems in Comparison to Stereo Vision Systems, pp. 103–130.

Jaakkola, A., Kaasalainen, S., Hyypp, J., Niittymki, H. and Akujrvi, A. (2008), Intensity calibration and imaging with swissranger sr3000 range camera, *in* 'International Archives of Photogrammetry, Remote Sensing and Spatial Information Sciences', Vol. XXXVII Part B3a, pp. 155–160.

Jamtsho, S. and Lichti, D. (2010), Modeling scattering distortion of 3d range camera, *in* 'International Archives of Photogrammetry, Remote Sensing and Spatial Information Sciences', Vol. XXXVIII, pp. 299–304.

Jauregui, D. V., White, K. R., Woodward, C. B. and Leitch, K. R. (2002), 'Static measurement of beam deformations via close-range photogrammetry', *Transportation Research Record* **1814**(1), 3–8.

Kahlmann, T. (2007), Range imaging metrology: Investigation, calibration and development, PhD Thesis, ETH, Zurich, Switzerland.

Kahlmann, T., Remondino, H. and Ingensand, H. (2006), Calibration for increased accuracy of the range imaging camera swissrangertm, *in* 'International Archives of Photogrammetry, Remote Sensing and Spatial Information Sciences', Vol. XXXVI Part 5, pp. 136–141.

Karel, W. (2008), Integrated range camera calibration using image sequences from hand-held operation, *in* 'International Archives of Photogrammetry, Remote Sensing and Spatial Information Sciences', Vol. XXXVII, pp. 945–951.

Karel, W., Dorninger, P. and Pfeifer, N. (2007), In situ determination of range camera quality parameters by segmentation, *in* 'Optical 3-D Measurement Techniques VIII', 9-12 July, Zurich, Switzerland. http://www.ipf.tuwien.ac.at/publications/2007/Karel_Dorninger_opt3d.pdf (accessed 12 Apr. 2010).

Karel, W., Ghuffar, S. and Pfeifer, N. (2010), Quantifying the distortion of distance observations caused by scattering in time-of-flight range cameras, *in* 'International Archives of Photogrammetry, Remote Sensing and Spatial Information Sciences', Vol. XXXVIII, pp. 316–321.

Kavli, T., Kirkhus, T., Thielemann, J. T. and Jagielski, B. (2008), Modelling and compensating measurement errors caused by scattering in time-of-flight cameras, *in* 'Proceedings SPIE:Two- and Three-Dimensional Methods for Inspection and Metrology VI,', Vol. 7066, pp. 4–13.

Kollorz, E., Penne, J., Hornegger, J. and Barke, A. (2008), 'Gesture recognition with a time-of-flight camera', *International Journal of Intelligent Systems Technologies and Applications* **5**(3-4), 334–343.

Kraus, A. D. (1987), *Matrices for Engineers*, Hemisphere Publishing Corporation, USA.

Kuang, S. (1996), *Geodetic Network Analysis and Optical Design: Concepts and Applications*, Ann Arbor Press, Chelsea, Michigan.

Lahamy, H. and Lichti, D. (2010), Real-time hand gesture recognition using range cameras, *in* 'International Archives of Photogrammetry, Remote Sensing and Spatial Information Sciences', Vol. XXXVII, pp. 54–59.

Lange, R. (2000), 3D time-of-flight distance measurement with custom solid-state sensors in cmos/ccd -technology, PhD Thesis, University of Siegen, Germany.

Lange, R. and Seitz, P. (2001), 'Solid-state time-of-flight range camera', *IEEE Journal of Quantum Electronics* **37**(3), 390–397.

Layton, J. B. (1997), 'Efficient direct computation of the pseudo-inverse and its gradient', *International Journal for Numerical Methods in Engineering* **40**(22), 4211–4223.

Li, Z. and Jarvis, R. (2009), Real time hand gesture recognition using a range camera, *in* 'Australasian Conference on Robotics and Automation(ACRA)', December 2-4, Sydney, Australia. http://www.araa.asn.au/acra/acra2009/papers/pap128s1.pdf (accessed 02 Feb. 2010).

Lichti, D. D. (2008), Self calibration of 3d range camera, *in* 'International Archives of Photogrammetry, Remote Sensing and Spatial Information Sciences', Vol. XXXVII, pp. 927–932.

Lichti, D. D., Kim, C. and Jamtsho, S. (2010), 'An integrated bundle adjustment approach to range camera geometric self-calibration', *ISPRS Journal of Photogrammetry and Remote Sensing* **65**(4), 360–368.

Lin, S. Y., Mills, J. P. and Gosling, P. D. (2009), 'Videogrammetric monitoring of as-built membrane roof structures', *Photogrammetric Record* **23**(122), 128–147.

Lindner, M. and Kolb, A. (2006), Calibration of the intensity related distance error of the pmd tof camera, *in* 'Proceedings of the SPIE on Intelligent Robots and Computer Vision XXV- Algorithms, Techniques, and Active Vision', 9 September, Boston, USA.

Lovas, T., Barsi, A., Detrekoi, A., Dunai, L., Csak, Z., Polgar, A., Berenyi, A., Kibedy, Z. and Szocs, K. (2008), Terrestrial laser scanning in deformation measurements of structures, *in* 'International Archives of the Photogrammetry, Remote Sensing and Spatial Information Sciences', Vol. XXXVII, pp. 527–532.

Luhmann, T., Robson, S., Kyle, S. and Harley, I. (2006), *Close range photogrammetry-principles, techniques and applications*, Whittles Publishing, Dunbeath.

MESA (2010), Swissranger sr4000 overview, http://www.mesa-imaging.ch (accessed 20 Jun. 2010).

Mure-Dubois, J. and Hugli, H. (2007), Optimized scattering compensation for time-of-flight-camera, *in* 'Proceedings of SPIE: The International Society for Optical Engineering', Vol. 6762, p. 6762 0H.

Myung, J. (2003), 'Tutorial on maximum likelihood estimation', *Journal of Mathematical Psychology* **47**(1), 90–100.

Niederost, M. and Maas, H. G. (1997), Automatic deformation measurement with a still video camera, *in* 'Optical 3D Measurement Techniques IV', Institute of Geodesy and Photogrammetry, Swiss Federal Institute of Technology, ETH Hoenggerberg, Zurich.

Oggier, T., Lehmann, M., Kaufmann, R., Schweizer, M., Richter, M., Metzler, P., Lang, G., Lustenberger, F. and Blanc, N. (2004), 'An all-solid-state optical range camera for 3d real-time imaging with sub-centimeter depth resolution of swissranger', *Optical Design and Engineering* **5249**(1), 534–545.

Oprisescu, S., Falie, D., Ciuc, M. and Buzuloiu, V. (2007), Measurements with toe cameras and their necessary corrections, *in* 'International Symposium on Signals, Circuits and Systems', Vol. 1, pp. 1–4.

Park, H. S. and Lee, H. M. (2007), 'A new approach for health monitoring of structures- terrestrial laser scanning', *Computer-Aided Civil and Infrastructure Engineering* **22**(1), 19–30.

Reulke, R. (2006), Combination of distance data with high resolution images, *in* 'Proceedings of the ISPRS Commission V Symposium', 25-27 September, Dresden, Germany.

Robbins, S., Murawski, B. and Schroeder, B. (2009), 'Photogrammetric calibration and colorization of the swissranger sr3100 3d range imaging sensor', *Optical Engineering* **48**(5), 1–8.

Ronnholm, P., Nuikka, M., Suominen, A., Salo, P., Hyypp, H., Pntinen, P., Haggrn, H., Vermeer, M., Puttonen, J., Hirsi, H., Kukko, A., Kaartinen, H., Hyypp, J. and Jaakkola, A. (2009), 'Comparison of measurement techniques and static theory applied to concrete beam deformation', *Photogrammetric Record* **24**(128), 351–371.

Rouzaud, D. (2008), Self-calibration of a laser range camera, MSc Thesis, École Polytechnique Fédérale de Lausanne , Switzerland.

Santrac, N., Friedland, G. and Rojas, R. (2006), High resolution segmentation with a time-of-flight 3d-camera using the example of a lecture scene, *in* 'Technical Report B-06-09,Fachbereich mathematic und informatik', September, Freie Universitt Berlin.

Schwarz, G. (1978), 'Estimating the dimension of a model', *The Annals of Statistics* **6**(2), 461–464.

Shakarji, C. M. (1998), 'Least-squares fitting algorithms of the nist algorithm testing system', *Journal of Research of the National Institute of Standards and Technology* **103**(6), 633–651.

Spirig, T. and Seitz, P. (1995), 'The lock-in ccd: Two-dimensional synchronous detection of light', *IEEE Journal of Quantum Electronics* **31**(9), 1705–1708.

Stockie, J. (2010), Cubic splines, http://www.math.sfu.ca/ stockie/teaching/-macm316/notes/splines.pdf (accessed 20 Jul. 2010).

Tsakiri, M., Lichti, D. D. and Pfeifer, N. (2006), Terrestrial laser scanning for deformation monitoring, *in* 'Proceedings of 3rd IAG Symposium on Geodesy for Geotechnical and Structural Engineering and 12th FIG Symposium on Deformation Measurements', Baden, Austria.

Westfeld, P., Mulsow, C. and Schulze, M. (2009), Photogrammetric calibration of range imaging sensors using intensity and range information simultaneously, *in* 'Proceedings Optical 3-D Measurement Techniques IX', July, Vienna, Austria.

Whiteman, T., Lichti, D. D. and Chandler, I. (2002), Measurement of deflections in concrete beams by close-range digital photogrammetry, *in* 'Proceedings of International Symposium on Geospatial Theory, Processing and Applications', Ottawa, USA.

Wiedemann, M., Sauer, M., Driewer, F. and Schilling, K. (2008), Analysis and characterization of the pmd camera for application in mobile robotics, *in* 'Proceedings of the 17th World Congress:The International Federation of Automatic Control', July 6-11, Seoul, Korea. http://www.nt.ntnu.no/users/skoge/prost/proceedings/ifac2008-/data/papers/3304.pdf (accessed 01 Feb. 2010).

Wiggenhagen, M. (1997), Long-term monitoring of the church st. michaelis in lueneburg, *in* 'International Archives of the Photogrammetry, Remote Sensing and Spatial Information Sciences', Vol. XXXIV, pp. 667–670.

Yamada, A., Furuhata, T., Shimada, K. and Hou, K. (1999), A discrete spring model for generating fair curves and surfaces, *in* 'Pacific Conference on Computer Graphics and Applications', 5-7 October, Seoul, Korea.

Appendix A

Appendix for Chapter 3

A.1 AIC computed values

Table A.1: Model selection results for the SR4000

Model No	**No of APs**	**No of Parameters**	**AIC**	$\frac{\mathbf{RSS}}{\mathbf{n}}$	$\mathbf{exp(-0.5 * (BIC - BIC_{min})}$
B8	7	337	2453.539	3.939	1
B6	9	339	2457.209	3.938	0.159582
B9	5	335	2462.647	3.979	0.010522
B10	5	335	2463.640	3.982	0.006407
B7	7	337	2465.633	3.976	0.002365
B1	13	343	3161.645	6.735	1.7E-154
B4	11	341	3196.461	6.939	4.7E-162
B2	12	342	3474.110	8.581	2.4E-222
B3	11	341	3479.717	8.631	1.5E-223
B5	9	339	3694.051	10.213	4.2E-270
		Min	2453.54	**sum**	1.178875

Model No	**Akaike Weights**	**RMSEx(mm)**	**RMSEy(mm)**	**RMSEz(mm)**
B8	0.848	18.37	14.13	4.90
B6	0.135	18.39	14.08	4.90
B9	0.009	32.90	63.76	13.09
B10	0.005	19.32	20.43	5.47
B7	0.002	19.32	20.27	5.45
B1	0.000	434.49	842.78	157.28
B4	0.000	466.87	899.85	168.31
B2	0.000	36.28	111.97	19.13
B3	0.000	37.08	114.16	19.51
B5	0.000	712.48	1333.24	252.06

TABLE A.2: AIC model selection results for SR3000

Model No	**No of APs**	**No of Parameters**	**AIC**	$\frac{\mathbf{RSS}}{\mathbf{n}}$	$\mathbf{exp(-0.5 * (BIC - BIC_{min})}$	**Akaike Weights**	**RMSEx(mm)**	**RMSEy(mm)**	**RMSEz(mm)**
A12	10	457	5999.882	5.552	1	0.651674	8.239	20.791	5.163
A26	8	455	6002.409	5.5642	0.282677	0.184213	9.27	26.827	5.674
A14	9	456	6003.985	5.5634	0.128523	0.083755	9.24	26.754	5.664
A10	11	458	6005.413	5.5586	0.062954	0.041026	8.094	20.504	5.084
A7	12	459	6007.776	5.5592	0.019313	0.012585	8.103	20.514	5.086
A16	9	456	6007.884	5.5707	0.018296	0.011923	9.522	27.832	5.79
A8	12	459	6008.453	5.5605	0.013767	0.008971	8.207	20.627	5.109
A6	13	460	6009.332	5.5584	0.008870	0.005781	8.158	20.569	5.1
A4	16	463	6018.429	5.5642	9.4E-005	6.1E-005	8.26	20.771	5.171
A1	18	465	6022.026	5.5635	1.6E-005	1.0E-005	8.233	20.736	5.163
A9	11	458	6029.651	5.6042	3.4E-007	2.2E-007	8.628	21.83	5.286
A11	11	458	6029.723	5.6043	3.3E-007	2.2E-007	8.53	21.752	5.257
A3	16	463	6037.503	5.6001	6.8E-009	4.4E-009	8.543	21.693	5.283
A13	10	457	6038.508	5.6247	4.1E-009	2.7E-009	7.793	20.599	5.027
A29	7	454	6038.828	5.6367	3.5E-009	2.3E-009	9.862	28.555	6.074
A19	8	455	6040.833	5.6367	1.3E-009	8.3E-010	9.862	28.555	6.073
A22	8	455	6041.912	5.6388	7.5E-010	4.9E-010	10.276	30.427	6.207
A25	8	455	6041.912	5.6388	7.5E-010	4.9E-010	10.276	30.427	6.207
A20	8	455	6042.161	5.6392	6.6E-010	4.3E-010	9.406	27.24	5.771
A17	9	456	6043.994	5.6389	2.6E-010	1.7E-010	9.698	28.332	5.917
A15	9	456	6047.626	5.6458	4.3E-011	2.8E-011	9.667	28.28	5.893
A5	15	462	6054.216	5.6355	1.6E-012	1.0E-012	7.72	20.427	5.008
A2	16	463	6056.504	5.6361	5.1E-013	3.3E-013	7.724	20.434	5.008
A18	9	456	6061.556	5.6724	4.1E-014	2.6E-014	8.214	21.88	5.17
A30	6	453	6103.071	5.764	3.9E-023	2.6E-023	10.51	30.518	6.335
A23	8	455	6164.970	5.8775	1.4E-036	9.2E-037	10.53	30.602	6.377
A21	8	455	6499.944	6.58	2.6E-109	1.7E-109	9.098	26.757	5.569
A24	8	455	6841.558	7.383	1.7E-183	1.1E-183	21.559	61.542	11.857
A28	7	454	6880.921	7.4866	4.8E-192	3.2E-192	10.894	31.739	6.638
A27	7	454	6887.424	7.5031	1.9E-193	1.2E-193	9.698	28.298	5.97
		Min	5999.882	**Sum**	1.534400				

Appendix B

Appendix for Chapter 4

B.1 Cubic Spline estimation

Cubic splines are often better choice for curve fitting as the spline fits the given data points exactly. A detail description of a computationally efficient method of constructing cubic splines through N number of data points is presented hereon as per the methods described by Stockie (2010). Equation B.1 is the cubic spline equation described by piecewise third-order polynomial for N number of data points where there are N-1 splines.

$$F_i(x) = a_i + b_i(x - x_i) + c_i(x - x_i)^2 + d_i(x - x_i)^3 \tag{B.1}$$

Where i = 1,2,$\cdots$,N-1 and a_i,b_i,c_i and d_i are the four parameters for each spline defined for each sub-interval $[x_i,x_{i+1}]$.

The main features of the cubic spline interpolation are:

- The spline pass through all the data points
- The first derivative is continuous at all interior points
- The second derivative is continuous at all interior points
- The boundary conditions at the end points are defined

By using these four conditions, Equation B.1 can be solved numerically. The first condition states that each spline, $F_i(x)$ passes through two points (x_i and x_{i+1}). So the number of

equations formed from all the splines from first condition is equal to 2[N-1]. The second condition states that the first derivative of Equation B.1 for the interior points between two successive splines are equal. From second condition,[N-2] equations can be obtained. The third condition states that the second derivative of Equation B.1 for the interior points between the two successive splines are equal. From third condition, [N-2] equations can be obtained. The fourth condition states that a constraint must be enforced on the first and the last point which thereby provides 2 equations. Using all the conditions of the spline interpolation,[4N-4] equations are obtained. The total number of unknown parameters in the spline equation is equal to four times (a_i,b_i,c_i and d_i) the number of splines (N-1), i.e. 4N-4. Hence a unique solution for the spline interpolation can be obtained using the aforementioned four conditions.

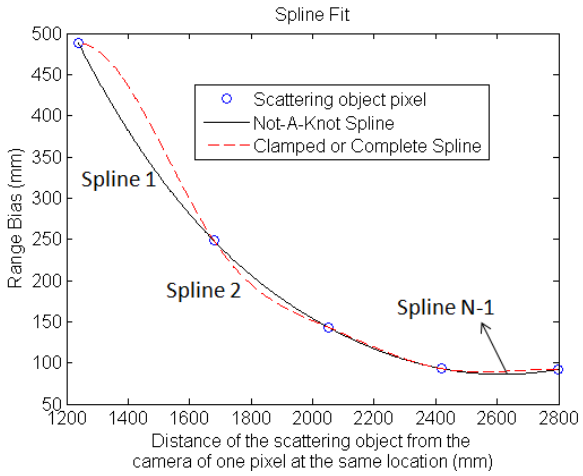

FIGURE B.1: Two method of spline interpolation

Figure B.1 shows the spline fit with four splines having 5 data points. Mathematically, the spline equation along with the first and second derivatives of spline 1, 2 and N-1 are represented from Equations B.2 to B.10.

Spline 1

$$F_1(x) = a_1 + b_1(x - x_1) + c_1(x - x_1)^2 + d_1(x - x_1)^3 \tag{B.2}$$

$$F_1^{'}(x) = b_1 + 2c_1(x - x_1) + 3d_1(x - x_1)^2 \tag{B.3}$$

$$F_1^{''}(x) = 2c_1 + 3d_1(x - x_1) \tag{B.4}$$

Spline 2

$$F_2(x) = a_2 + b_2(x - x_2) + c_2(x - x_2)^2 + d_2(x - x_2)^3 \tag{B.5}$$

$$F_2^{'}(x) = b_2 + 2c_2(x - x_2) + 3d_2(x - x_2)^2 \tag{B.6}$$

$$F_2^{''}(x) = 2c_2 + 3d_2(x - x_2) \tag{B.7}$$

$\cdots$,

Spline N-1

$$F_{N-1}(x) = a_{N-1} + b_{N-1}(x - x_{N-1}) + c_{N-1}(x - x_{N-1})^2 + d_{N-1}(x - x_{N-1})^3 \tag{B.8}$$

$$F_{N-1}^{'}(x) = b_{N-1} + 2c_{N-1}(x - x_{N-1}) + 3d_{N-1}(x - x_{N-1})^2 \tag{B.9}$$

$$F_{N-1}^{''}(x) = 2c_{N-1} + 3d_{N-1}(x - x_{N-1}) \tag{B.10}$$

The first three spline conditions can be expressed as follows.

First Condition

$$F_i(x_i) = a_i + b_i(x_i - x_i) + c_i(x_i - x_i)^2 + d_i(x_i - x_i)^3$$

$$= a_i$$

$$\Rightarrow y_i = a_i \tag{B.11}$$

$$F_i(x_{i+1}) = a_i + b_i(x_{i+1} - x_i) + c_i(x_{i+1} - x_{i+1})^2 + d_i(x_{i+1} - x_{i+1})^3$$

$$\Rightarrow y_{i+1} = a_i + b_i(h_i) + c_i(h_i)^2 + d_i(h_i)^3 \tag{B.12}$$

where $h_i = x_{i+1} - x_i$ and i = 1,2,$\cdots$,N

Second Condition

$$F_i^{'}(x_{i+1}) = F_{i+1}^{'}(x_{i+1})$$

$$b_i + 2c_i(x_{i+1} - x_i) + 3d_i(x_{i+1} - x_i)^2 = b_{i+1} + 2c_{i+1}(x_{i+1} - x_{i+1}) + 3d_{i+1}(x_{i+1} - x_{i+1})^2$$

$$\Rightarrow b_i + 2c_i(h_i) + 3d_i(h_i)^2 - b_{i+1} = 0 \tag{B.13}$$

where $h_i = x_{i+1} - x_i$ and i = 1,2,$\cdots$,N-1

Third Condition

$$F_i^{''}(x_{i+1}) = F_{i+1}^{''}(x_{i+1})$$

$$2c_i + 6d_i(x_{i+1} - x_i) = 2c_{i+1} + 6d_{i+1}(x_{i+1} - x_{i+1})$$

$$\Rightarrow 2c_i + 6d_i(h_i) - 2c_{i+1} = 0 \tag{B.14}$$

where $h_i = x_{i+1} - x_i$ and i = 1,2,$\cdots$,N-1

The above equations can be further simplified by defining

$$m_i = F_i^{''}(x_i) = 2c_i \tag{B.15}$$

$$\Rightarrow c_i = \frac{m_i}{2} \tag{B.16}$$

Substituting Equation B.15 in Equation B.14, we get

$$F_i^{''}(x_{i+1}) = F_{i+1}^{''}(x_{i+1})$$

$$\Rightarrow m_i + 6d_i(h_i) - m_{i+1} = 0$$

$$\Rightarrow d_i = \frac{m_{i+1} - m_i}{6h_i} \tag{B.17}$$

Further substituting Equations B.16, B.17 and B.11 in Equation B.12, we get

$$y_{i+1} = a_i + b_i(h_i) + c_i(h_i)^2 + d_i(h_i)^3$$

$$\Rightarrow y_{i+1} = y_i + b_i(h_i) + \tfrac{m_i}{2}(h_i)^2 + \tfrac{m_{i+1}-m_i}{6h_i}(h_i)^3$$

$$\Rightarrow b_i = \frac{y_{i+1} - y_i}{h_i} - \frac{h_i}{2}m_i - \frac{h_i}{6}(m_{i+1} - m_i) \tag{B.18}$$

Finally, substituting Equations B.16, B.17 and B.18 in Equation B.13, we get

$$b_i + 2c_i(h_i) + 3d_i(h_i)^2 - b_{i+1} = 0$$

$$\tfrac{y_{i+1}-y_i}{h_i} - \tfrac{h_i}{2}m_i - \tfrac{h_i}{6}(m_{i+1} - m_i) + 2\tfrac{m_i}{2}(h_i) + 3\tfrac{m_{i+1}-m_i}{6h_i}(h_i)^2 - b_{i+1} = 0$$

$$\Rightarrow h_i m_i + 2(h_i + h_{i+1})m_{i+1} + h_{i+1}m_{i+2} = 6\left[\frac{y_{i+2} - y_{i+1}}{h_{i+1}} - \frac{y_{i+1} - y_i}{h_i}\right] \tag{B.19}$$

Equation B.19 is the fundamental spline equation. Rearranging the different terms by group results into a tri-diagonal set of linear system of equations as shown in Equation B.20. This tri-diagonal system of linear equations can be solved trivially using simple algorithm.

$$\begin{bmatrix} ? & & & & & & \\ h_1 & 2(h_1+h_2) & h_2 & & & & \\ & h_2 & 2(h_2+h_3) & h_3 & \ddots & & \\ & & \ddots & \ddots & \ddots & & \\ & & & \ddots & h_{n-2} & & \\ & & & h_{n-2} & 2(h_{n-2}+h_{n-1}) & h_{n-1} & \\ & & & & & ? & \end{bmatrix} \begin{bmatrix} m_1 \\ m_2 \\ \vdots \\ \vdots \\ \vdots \\ m_{n-1} \\ m_n \end{bmatrix} = 6 \begin{bmatrix} ? \\ \frac{y_3-y_2}{h_2} - \frac{y_2-y_1}{h_1} \\ \vdots \\ \vdots \\ \vdots \\ \frac{y_n-y_{n-1}}{h_{n-1}} - \frac{y_{n-1}-y_{n-2}}{h_{n-2}} \\ ? \end{bmatrix} \tag{B.20}$$

Excluding the first and the last equations represented by ? symbol results into [N-2] set of equations available for solving N unknowns$(m_1, \cdots, m_n)$. The two deficit equations are obtained by defining the boundary conditions for the first and the last data point of the spline. There are several ways of defining constraints in the end points, such as:

- Natural Spline (Zero curvature)

  $m_1 = 0$ and $m_n = 0$

- Specified first derivatives at the first and last point (Clamped Spline)

  $F_1^{'}(x_1) = P$ and $F_{n-1}^{'}(x_n) = Q$

  The first and last equations becomes

  $\Rightarrow 2h_1m_1 + h_1m_2 = 6\left[\frac{y_2-y_1}{h_1} - P\right]$

  $\Rightarrow h_{n-1}m_{n-1} + 2h_{n-1}m_n = 6\left[Q - \frac{y_n-y_{n-1}}{h_{n-1}}\right]$

  The design matrix of Equation B.20 becomes

$$\begin{bmatrix} 2h_1 & h_1 & 0 & \cdots & \cdots & & \\ h_1 & 2(h_1+h_2) & h_2 & & & & \\ 0 & h_2 & 2(h_2+h_3) & h_3 & \ddots & & \\ & & & \ddots & \ddots & & \\ & & & & \ddots & h_{n-2} & \\ & & & & h_{n-2} & 2(h_{n-2}+h_{n-1}) & h_{n-1} \\ & & & & 0 & h_{n-1} & 2h_{n-1} \end{bmatrix}$$

- Specified second derivatives at the first and last point

  $F_1^{''}(x_1) = J$ and $F_n^{''}(x_n) = K$

- Zero slope

  $F_1^{'}(x_1) = 0$ and $F_n^{'}(x_n) = 0$

- Not-a-Knot spline

  $F_1'''(x_2) = F_2'''(x_2)$ and $F_{N-2}'''(x_{N-1}) = F_{N-1}'''(x_{N-1})$

  Using $F_i'''(x) = 6d_i$ and Equation B.17, the condition equations become

  $\Rightarrow m_2 - m_1 = m_3 - m_2$

  $\Rightarrow m_{n-1} - m_{n-2} = m_n - m_{n-1}$

  The design matrix in this case is

$$\begin{bmatrix} -1 & 2 & -1 & \cdots & \cdots & & \\ h_1 & 2(h_1+h_2) & h_2 & & & & \\ 0 & h_2 & 2(h_2+h_3) & h_3 & \ddots & & \\ & & & \ddots & \ddots & & \\ & & & & \ddots & h_{n-2} & \\ & & & & h_{n-2} & 2(h_{n-2}+h_{n-1}) & h_{n-1} \\ & & & & -1 & 2 & -1 \end{bmatrix}$$

Appendix C

Appendix for Chapter 5

C.1 MATLAB code for the automatic extraction of the thin plates

```
Data preparation

clear all;
close all;
clc;
%input file path
inputFile='D:\Summer2010\StructuralDeformation\Data\ProcessExp1\Sonam...
\Interference\AllStops\SR4000_Cam2Sonam_Exp1_1to14Img_Interf2.sri';
%extracting data from the matlab .sri format file
[X,Y,Z,R,B]=extractData(inputFile);
%define image coordinate system x and y- axes
x_ax = 0:0.04:176*0.04-0.04;
y_ax=0:0.04:144*0.04-0.04;
[Xa, Ya] = meshgrid(x_ax,y_ax);
%Step 1: Segment Thin Plates for all dataset by using Z threshold value
[Xnew Ynew Znew Rnew Bnew] = getSegmentedB(Xa,Ya,Z,R,B);
B2=Bnew{1};%first image

Automatic extraction of thin plates point cloud

figure;
set(gca,'FontSize',13)
imagesc(B{1})
title('Amplitude Image of the actual deformation scene')
colormap(gray)
```

```
figure;
set(gca,'FontSize',13)
imagesc(B2)
title('Amplitude image after Z based segmentation')
%Canny edge detection
%B2 (144,176): amplitude image
BW = edge(B2,'canny');%binary image with edges detected
figure;
set(gca,'FontSize',13)
imagesc(BW)
title('Canny edge detection')
%.....................................................
%Centroid based classification
cc = bwconncomp(BW);%returns the connected components cc found in BW
stats = regionprops(cc, 'Centroid');%measures a set of properties
% ('Area','Centroid') for each connected component (object) in CC,
% which is a structure returned by bwconncomp Centroid: centre of
%the region
cen = ceil([stats.Centroid]);%fixing the integer values
cenR = reshape(cen,2,length(cen)/2);
idx1 = find(cenR(2,:) < 100 & cenR(2,:) > 60);
%ismember returns a vector the same length as labelmatrix(cc),
% containing logical 1 (true) where the elements of idx1 are
%in the set labelmatrix(cc), and logical 0 (false) elsewhere
BW2 = ismember(labelmatrix(cc), idx1);
%BW2 is new binary image with most of the undesired edges are removed,
%however still some unwanted edges are present
figure;
set(gca,'FontSize',13)
imagesc(BW2)
title('Centroid based classification')
%.....................................................
%Further calssification based on the Eccentricity
ee = bwconncomp(BW2);
stats2 = regionprops(ee,'Eccentricity');
%Eccentricity: Scalar that specifies the eccentricity of the ellipse that
%has the same second-moments as the region
idx0 = find([stats2.Eccentricity] > .75);
idx00 = find([stats2.Eccentricity] < .94);
idx=intersect(idx0,idx00);%the intersection of the two sets
BW4 = ismember(labelmatrix(ee), idx);
figure;
set(gca,'FontSize',13)
imagesc(BW4)
title('Eccentricity based classification')
```

```
%.....................................................
%Further classification based on the area of the region
ee = bwconncomp(BW4);
stats2 = regionprops(ee, 'Area');
%Area: area of the region
idx = find([stats2.Area] > 30);
BW4 = ismember(labelmatrix(ee), idx);
figure;
set(gca,'FontSize',13)
imagesc(BW4)
title('Area based classification')
```

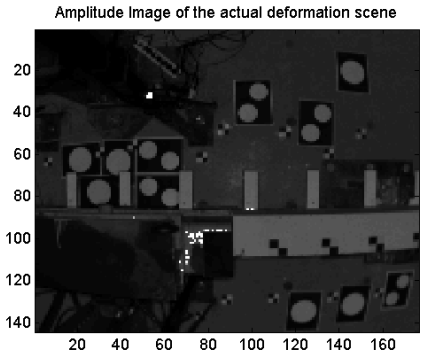

(a)

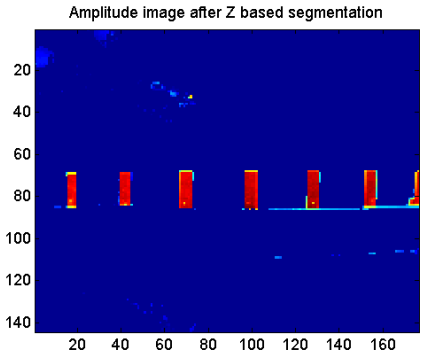

(b)

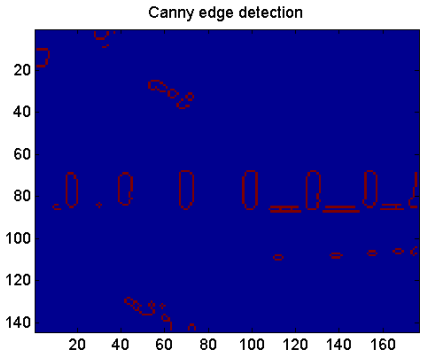

(c)

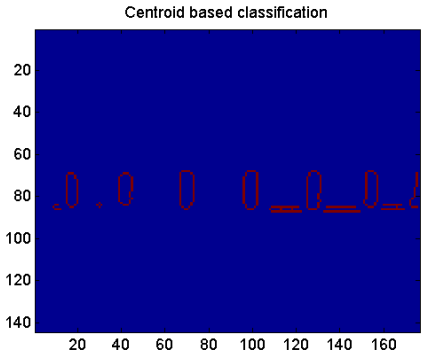

(d)

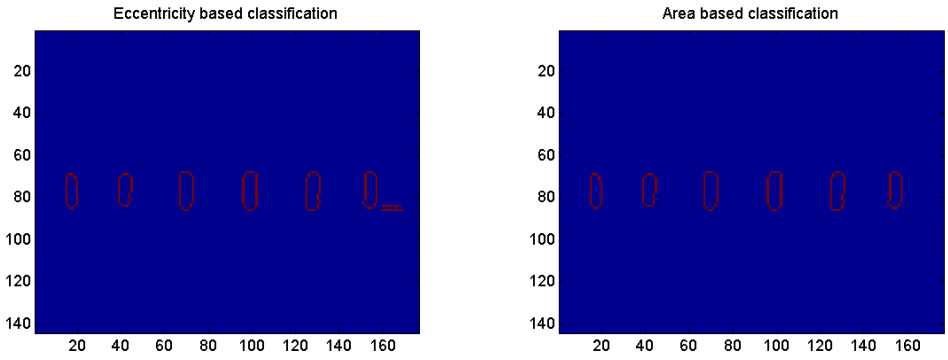

(e) (f)

C.2 RANSAC based segmentation

According to Fischler and Bolles (1981), RANSAC (Random Sample Consensus) is a new paradigm for estimating model parameters on a consensus set of inliers which are modified and selected iteratively based on statistical evaluation. Hence the data outliers are excluded from the estimation effectively. Traditionally, the least squares method fits a model on a given set of data and then iteratively remove the outliers based on some statistical evaluation. What RANSAC does is that it begins estimation of the model parameters using minimum set of points required for a particular model and then modify this set with consistent data iteratively based on statistical evaluation.

For instance, in a plane fitting RANSAC will begin by selecting randomly a set of 3 points as the minimum points require to fit a plane is three, and then compute the plane parameters for all the sets. The set that best fits the plane is ranked higher than the other sets, which then form a consensus set that will be selected for the next iteration where neighbourhood points will be incorporated for further estimation. This process continues iteratively until all the points had been evaluated for their closeness of fit with the instantiated model. Whenever the set of selected inliers exceeds the minimum number of points required for the parameter estimation, a least squares method can be used to update the model parameters of the consensus set. If one consensus set fails at some point of iteration, then the next best consensus set is chosen for further evaluation. If none of the consensus set are successful in achieving the predefined threshold, then the algorithm terminate in failure or solve the model parameters with the best available consensus set.

In the case of the plane fitting, initially three points are selected to compute the plane parameters using the method of the orthogonal regression. The plane is defined as given in Equation C.2

$$\vec{n}^T(\vec{r_i} - \vec{\bar{r}}) = 0 \tag{C.1}$$

where $\vec{n}$ is the normal of the plane, $\vec{r_i}$ is the observation point reduced to the centroid of the set of the planar points, and $\vec{\bar{r}}$ is the point on the plane.

Using this model parameters, an additional point p in the neighbourhood can be tested for its suitability for inclusion in the consensus set by evaluating the metric distance as follows.

$$\delta = \|\vec{n}^T(\vec{r_p} - \vec{\bar{r}})\| \tag{C.2}$$

Where $\vec{r_p}$ is the position vector of p reduced to the centroid. If the δ is within the predefined threshold then this point is included as the inliers, else it is discarded as the outliers. This procedure is repeated for the other points and the other available initial sets in order to obtain the best consensus set for estimating the final plane parameters.

C.3 TLS accuracy assessment data

TABLE C.1: Concrete beam: Deflection values of the TLS and laser transducer

	TLS			**Laser Transducer**		
	Strip 5	**Strip 7**	**Strip 9**	**Strip 5**	**Strip 7**	**Strip 9**
5 mm	-3.70	-4.30	-3.70	4.33	5.01	4.32
10 mm	-8.03	-9.39	-8.13	8.70	10.00	8.64
15 mm	-11.98	-14.37	-12.32	13.09	15.01	12.71
20 mm	-15.85	-19.41	-16.02	16.83	20.00	16.56
25 mm	-19.11	-24.42	-19.72	20.63	25.00	19.95
30 mm	-22.59	-29.49	-23.57	22.17	30.00	23.40
35 mm	-26.24	-34.49	-27.45	NA	35.00	27.08
40 mm	-30.15	-39.44	-31.25	NA	40.00	30.90
45 mm	-33.65	-44.44	-35.02	NA	45.00	34.50
50 mm	-37.02	-49.50	-38.90	NA	50.00	37.88
55 mm	-40.07	-54.42	-42.65	NA	55.01	40.96
60 mm	-42.95	-59.46	-45.77	NA	60.00	43.80
65 mm	-46.03	-64.33	-48.99	NA	65.00	46.96

TABLE C.2: Polymer sheet beam: Deflection values of the TLS and laser transducer

	TLS			**Laser Transducer**		
	Strip 5	**Strip 7**	**Strip 9**	**Strip 5**	**Strip 7**	**Strip 9**
5 mm	-3.79	-4.38	-3.81	4.50	5.01	4.30
10 mm	-8.06	-9.42	-8.04	8.87	10.00	8.62
15 mm	-12.34	-14.54	-12.51	13.25	15.00	12.90
20 mm	-16.29	-19.54	-16.23	20.01	23.22	19.34
25 mm	-20.22	-24.59	-20.14	21.42	25.00	20.88
30 mm	-23.44	-31.98	-28.80	24.21	31.91	25.99
35 mm	-24.95	-34.34	-30.35	25.78	35.01	27.89
40 mm	-28.17	-39.19	-31.71	29.08	40.00	31.31
45 mm	-31.57	-44.29	-36.52	32.40	45.00	34.47
50 mm	-34.16	-48.73	-38.79	35.78	50.00	37.73
55 mm	-38.26	-53.96	-43.56	39.19	55.01	41.08
60 mm	-41.65	-59.05	-46.97	42.61	60.01	44.42
65 mm	-44.95	-63.88	-50.42	46.02	65.00	47.78

C.4 Experiment 1: Phase 1 data

Table C.3: Exp. 1 Phase 1: Centroid measurement of the TLS

	0 mm	**3 mm**	**0 mm**	**3 mm**	**0 mm**
Plate 1	3563.699	3563.598	3563.737	3563.539	3563.796
Plate 2	3566.709	3565.650	3566.260	3565.577	3566.257
Plate 3	3565.301	3563.638	3564.803	3563.524	3564.791
Plate 4	3564.324	3562.097	3563.732	3562.014	3563.675
Plate 5	3562.248	3559.515	3561.445	3559.39	3561.401
Plate 6	3563.064	3559.935	3562.151	3559.899	3562.142
Plate 7	3560.558	3557.285	3559.585	3557.209	3559.563
Plate 8	3560.569	3557.412	3559.681	3557.367	3559.625
Plate 9	3561.683	3558.922	3560.872	3558.909	3560.888
Plate 10	3561.500	3559.265	3560.882	3559.237	3560.865
Plate 11	3562.393	3560.650	3561.866	3560.647	3561.853
Plate 12	3562.105	3561.075	3561.824	3561.071	3561.804
Plate 13	3561.473	3561.113	3561.273	3561.084	3561.317

Table C.4: Exp. 1 Phase 1: Deflection values of the TLS

	0 mm	**3 mm**	**0 mm**	**3 mm**	**0 mm**
Plate 1	0	-0.1005	0.038	-0.1601	0.0979
Plate 2	0	-1.0584	-0.4491	-1.1316	-0.4515
Plate 3	0	-1.6632	-0.4987	-1.7772	-0.5098
Plate 4	0	-2.2265	-0.5922	-2.3099	-0.6489
Plate 5	0	-2.7329	-0.8028	-2.8581	-0.8466
Plate 6	0	-3.1293	-0.9131	-3.165	-0.9221
Plate 7	0	-3.2737	**-0.9729**	-3.3498	**-0.9953**
Plate 8	0	-3.1576	-0.8886	-3.2027	-0.9443
Plate 9	0	-2.7612	-0.8114	-2.774	-0.7953
Plate 10	0	-2.2349	-0.6175	-2.2632	-0.6342
Plate 11	0	-1.7425	-0.527	-1.7454	-0.5396
Plate 12	0	-1.0304	-0.2811	-1.0341	-0.3009
Plate 13	0	-0.3591	-0.1999	-0.3891	-0.156

Table C.5: Exp. 1 Phase 1: Centroid measurement of the RC 1

	0 mm	**3 mm**	**0 mm**	**3 mm**	**0 mm**
Plate 1	2167.663	2164.029	2166.392	2166.696	2164.789
Plate 2	2162.374	2159.586	2160.972	2161.757	2159.691
Plate 3	2160.059	2158.710	2158.636	2159.361	2157.111
Plate 4	2155.980	2153.878	2154.016	2155.117	2152.530
Plate 5	2153.767	2149.595	2150.652	2152.587	2149.463
Plate 6	2148.309	2140.189	2144.391	2147.140	2142.932
Plate 7	2146.167	2132.146	2140.772	2143.208	2139.095

Table C.6: Exp. 1 Phase 1: Deflection values of the RC 1

	0 mm	**3 mm**	**0 mm**	**3 mm**	**0 mm**
Plate 1	0	-3.6339	-1.2714	-0.9673	-2.8746
Plate 2	0	-2.7885	-1.4022	-0.6173	-2.684
Plate 3	0	-1.3486	-1.4225	-0.698	-2.9474
Plate 4	0	-2.1017	-1.9639	-0.8636	-3.4497
Plate 5	0	-4.172	-3.1152	-1.1802	-4.3045
Plate 6	0	-8.1198	-3.9174	-1.1684	-5.3765
Plate 7	0	-14.0213	-5.3952	-2.9589	-7.0723

Table C.7: Exp. 1 Phase 1: Centroid measurement of the RC 2

	0 mm	**3 mm**	**0 mm**	**3 mm**	**0 mm**
Plate 7	2161.526	2162.804	2162.236	2163.943	2162.880
Plate 8	2153.810	2156.082	2154.782	2156.543	2155.411
Plate 9	2147.052	2149.300	2147.321	2149.296	2148.124
Plate 10	2142.117	2145.401	2143.413	2145.441	2144.442
Plate 11	2135.872	2138.023	2136.454	2138.349	2137.418
Plate 12	2127.942	2129.162	2128.309	2129.241	2128.770

Table C.8: Exp. 1 Phase 1: Deflection values of the RC 2

	0 mm	**3 mm**	**0 mm**	**3 mm**	**0 mm**
Plate 7	0	1.2787	0.7103	2.4174	1.3544
Plate 8	0	2.2712	0.9714	2.7321	1.6006
Plate 9	0	2.2479	0.2689	2.244	1.0714
Plate 10	0	3.2837	1.2958	3.3235	2.3248
Plate 11	0	2.1513	0.5819	2.4777	1.5463
Plate 12	0	1.2196	0.3672	1.2988	0.8282

C.5 Experiment 1: Phase 2 data

TABLE C.9: Exp. 1 Phase 2: Centroid measurement of the TLS

	0 mm	**5 mm**	**10 mm**	**15 mm**	**20 mm**	**25 mm**	**30 mm**
Plate 1	3563.796	3563.544	3563.469	3563.517	3563.477	3563.562	3563.326
Plate 2	3566.257	3564.983	3563.692	3562.466	3561.48	3560.636	3559.758
Plate 3	3564.791	3562.563	3560.096	3557.904	3555.907	3554.156	3552.365
Plate 4	3563.675	3560.663	3557.099	3553.981	3551.144	3548.637	3545.985
Plate 5	3561.401	3557.705	3553.374	3549.415	3545.555	3542.263	3538.770
Plate 6	3562.142	3557.987	3552.958	3548.215	3543.386	3539.177	3534.802
Plate 7	3559.563	3555.262	3550.179	3545.199	3540.149	3535.142	3530.069
Plate 8	3559.625	3555.436	3550.421	3545.497	3540.910	3536.216	3531.243
Plate 9	3560.885	3557.172	3552.755	3548.563	3544.888	3541.222	3537.401
Plate 10	3560.865	3557.776	3554.175	3550.763	3547.998	3545.239	3542.396
Plate 11	3561.853	3559.621	3557.012	3554.647	3552.809	3550.964	3549.108
Plate 12	3561.804	3560.459	3559.026	3557.733	3556.810	3555.910	3554.976
Plate 13	3561.317	3561.076	3560.952	3560.902	3560.884	3560.925	3560.957

	35 mm	**40 mm**	**45 mm**	**50 mm**	**55 mm**	**60 mm**	**65 mm**
Plate 1	3563.316	3563.305	3563.234	3563.128	3563.180	3563.146	3563.169
Plate 2	3558.751	3557.722	3556.855	3556.057	3555.321	3554.515	3553.702
Plate 3	3550.433	3548.524	3546.646	3544.819	3543.415	3541.980	3540.551
Plate 4	3543.231	3540.356	3537.622	3535.088	3532.827	3530.651	3528.401
Plate 5	3535.090	3531.158	3527.621	3524.224	3521.160	3518.261	3515.173
Plate 6	3529.805	3524.975	3520.271	3516.004	3512.200	3508.461	3504.558
Plate 7	3525.063	3520.104	3515.065	3509.989	3505.022	3499.978	3495.097
Plate 8	3526.380	3521.263	3515.034	3509.506	3503.684	3499.290	3494.974
Plate 9	3533.571	3529.843	3526.183	3522.361	3518.723	3515.627	3512.452
Plate 10	3539.509	3536.759	3533.990	3531.123	3528.427	3526.184	3523.736
Plate 11	3547.206	3545.330	3543.552	3541.666	3539.863	3538.412	3536.910
Plate 12	3554.029	3553.117	3552.202	3551.259	3550.416	3549.754	3549.015
Plate 13	3561.010	3560.996	3561.079	3561.079	3561.187	3561.225	3561.320

TABLE C.10: Exp. 1 Phase 2: Deflection (δZ) values of the TLS

	0 mm	**5 mm**	**10 mm**	**15 mm**	**20 mm**	**25 mm**	**30 mm**
Plate 1	0	-0.2523	-0.3273	-0.28	-0.3199	-0.2348	-0.4703
Plate 2	0	-1.2741	-2.5655	-3.7908	-4.7771	-5.6215	-6.4994
Plate 3	0	-2.2284	-4.6953	-6.8872	-8.8848	-10.6352	-12.4263
Plate 4	0	-3.0117	-6.5759	-9.6943	-12.5306	-15.0384	-17.6902
Plate 5	0	-3.6964	-8.027	-11.9862	-15.847	-19.1381	-22.6317
Plate 6	0	-4.1551	-9.1841	-13.9274	-18.7559	-22.9645	-27.34
Plate 7	0	-4.3011	-9.3844	-14.364	-19.4143	-24.4209	-29.4941
Plate 8	0	-4.1886	-9.2041	-14.1279	-18.7146	-23.4093	-28.3817
Plate 9	0	-3.7131	-8.1303	-12.3223	-15.997	-19.663	-23.4836
Plate 10	0	-3.0898	-6.6906	-10.1025	-12.8676	-15.6267	-18.4697
Plate 11	0	-2.2313	-4.8402	-7.2057	-9.044	-10.8888	-12.745
Plate 12	0	-1.3446	-2.7779	-4.0713	-4.9941	-5.8941	-6.828
Plate 13	0	-0.2408	-0.3651	-0.4144	-0.4323	-0.3911	-0.3598

	35 mm	**40 mm**	**45 mm**	**50 mm**	**55 mm**	**60 mm**	**65 mm**
Plate 1	-0.48	-0.4915	-0.5625	-0.6683	-0.6164	-0.6508	-0.6273
Plate 2	-7.5057	-8.535	-9.4023	-10.2006	-10.9359	-11.7423	-12.5547
Plate 3	-14.3583	-16.2676	-18.1459	-19.9726	-21.3768	-22.8116	-24.2409
Plate 4	-20.4439	-23.3195	-26.0527	-28.5871	-30.8477	-33.0246	-35.2745
Plate 5	-26.3114	-30.2433	-33.7807	-37.1778	-40.2412	-43.1409	-46.2287
Plate 6	-32.3372	-37.1672	-41.8705	-46.1382	-49.9423	-53.6811	-57.5839
Plate 7	-34.5002	-39.4592	-44.498	-49.5738	-54.541	-59.5847	-64.4656
Plate 8	-33.2453	-38.3617	-44.5906	-50.119	-55.9414	-60.3345	-64.6509
Plate 9	-27.3141	-31.0417	-34.7016	-38.5241	-42.1623	-45.2576	-48.4327
Plate 10	-21.3562	-24.1063	-26.876	-29.7421	-32.4383	-34.6812	-37.1294
Plate 11	-14.6467	-16.5227	-18.3001	-20.1868	-21.9899	-23.4406	-24.9421
Plate 12	-7.7745	-8.6866	-9.6021	-10.5448	-11.3874	-12.0501	-12.7893
Plate 13	-0.3065	-0.3203	-0.2374	-0.2378	-0.1297	-0.0918	0.0036

TABLE C.11: Exp. 1 Phase 2: Centroid measurement of the RC 1

	0 mm	**5 mm**	**10 mm**	**15 mm**	**20 mm**	**25 mm**	**30 mm**
Plate 1	-2150.90	-2152.58	-2151.48	-2152.61	-2150.31	-2149.92	-2151.03
Plate 2	-2149.28	-2151.65	-2152.00	-2154.01	-2153.21	-2154.40	-2154.85
Plate 3	-2151.01	-2154.14	-2155.85	-2158.68	-2159.36	-2161.65	-2162.23
Plate 4	-2151.05	-2154.50	-2158.03	-2162.58	-2164.33	-2167.83	-2168.48
Plate 5	-2152.74	-2156.93	-2161.21	-2165.27	-2169.25	-2174.64	-2174.58
Plate 6	-2150.71	-2155.45	-2159.87	-2164.68	-2169.59	-2177.08	-2176.32
Plate 7	-2150.68	-2155.32	-2160.16	-2164.98	-2171.01	-2182.57	-2179.23

	35 mm	**40 mm**	**45 mm**	**50 mm**	**55 mm**	**60 mm**	**65 mm**
Plate 1	-2151.23	-2152.13	-2153.12	-2151.69	-2150.52	-2151.91	-2153.99
Plate 2	-2156.59	-2157.98	-2159.78	-2159.52	-2158.97	-2160.81	-2163.88
Plate 3	-2165.41	-2167.54	-2170.08	-2171.03	-2171.24	-2172.69	-2176.29
Plate 4	-2172.85	-2175.11	-2178.87	-2180.41	-2181.31	-2183.31	-2188.23
Plate 5	-2180.45	-2183.35	-2188.43	-2190.86	-2192.53	-2194.90	-2200.96
Plate 6	-2184.03	-2187.46	-2194.06	-2197.09	-2199.70	-2203.06	-2209.80
Plate 7	-2188.25	-2190.38	-2197.44	-2200.12	-2205.43	-2209.53	-2217.66

TABLE C.12: Exp. 1 Phase 2: Deflection (δZ) values of the RC 1

	0 mm	**5 mm**	**10 mm**	**15 mm**	**20 mm**	**25 mm**	**30 mm**
Plate 1	0	-1.6742	-0.579	-1.7095	0.5951	0.9857	-0.1292
Plate 2	0	-2.3712	-2.7275	-4.7359	-3.9319	-5.1228	-5.5749
Plate 3	0	-3.1304	-4.8385	-7.6754	-8.3552	-10.641	-11.2268
Plate 4	0	-3.4444	-6.9786	-11.5299	-13.2723	-16.7729	-17.4276
Plate 5	0	-4.1861	-8.4618	-12.5252	-16.5037	-21.8943	-21.8358
Plate 6	0	-4.7354	-9.1591	-13.9734	-18.8795	-26.3689	-25.6082
Plate 7	0	-4.6408	-9.4743	-14.2972	-20.3287	-31.8902	-28.5471

	35 mm	**40 mm**	**45 mm**	**50 mm**	**55 mm**	**60 mm**	**65 mm**
Plate 1	-0.3244	-1.2249	-2.2188	-0.7896	0.386	-1.0068	-3.084
Plate 2	-7.3187	-8.7056	-10.4997	-10.241	-9.6913	-11.5298	-14.6038
Plate 3	-14.4063	-16.5326	-19.0698	-20.0253	-20.2337	-21.6795	-25.2854
Plate 4	-21.794	-24.0558	-27.8148	-29.3524	-30.2587	-32.2517	-37.1798
Plate 5	-27.7072	-30.6077	-35.6824	-38.1181	-39.7883	-42.1543	-48.2188
Plate 6	-33.3158	-36.7485	-43.3503	-46.3821	-48.9883	-52.3476	-59.0897
Plate 7	-37.5665	-39.6954	-46.7526	-49.4365	-54.7467	-58.8447	-66.9719

TABLE C.13: Exp. 1 Phase 2: Centroid measurement of the RC 2

	0 mm	**5 mm**	**10 mm**	**15 mm**	**20 mm**	**25 mm**	**30 mm**
Plate 7	-2190.20	-2194.04	-2199.76	-2204.72	-2210.56	-2213.54	-2219.62
Plate 8	-2174.00	-2177.74	-2183.14	-2187.75	-2193.92	-2196.87	-2202.76
Plate 9	-2157.47	-2160.28	-2165.46	-2169.52	-2174.42	-2176.68	-2180.92
Plate 10	-2144.56	-2146.82	-2151.54	-2153.93	-2157.87	-2159.36	-2162.46
Plate 11	-2129.05	-2130.99	-2134.39	-2136.60	-2138.92	-2139.56	-2140.84
Plate 12	-2112.95	-2114.02	-2115.97	-2116.73	-2118.65	-2118.39	-2118.48

	35 mm	**40 mm**	**45 mm**	**50 mm**	**55 mm**	**60 mm**	**65 mm**
Plate 7	-2222.67	-2228.57	-2234.87	-2241.08	-2245.28	-2249.22	-2255.28
Plate 8	-2206.62	-2212.68	-2218.48	-2224.70	-2229.59	-2233.29	-2238.52
Plate 9	-2184.50	-2188.28	-2191.73	-2196.24	-2199.93	-2201.86	-2205.72
Plate 10	-2165.70	-2168.84	-2170.96	-2174.62	-2177.08	-2177.77	-2181.23
Plate 11	-2142.92	-2146.83	-2148.08	-2149.12	-2150.88	-2150.11	-2153.55
Plate 12	-2119.59	-2122.54	-2121.79	-2123.26	-2123.87	-2121.87	-2124.83

TABLE C.14: Exp. 1 Phase 2: Deflection (δZ) values of the RC 2

	0 mm	**5 mm**	**10 mm**	**15 mm**	**20 mm**	**25 mm**	**30 mm**
Plate 7	0	-3.8394	-9.5603	-14.5157	-20.3612	-23.3391	-29.4207
Plate 8	0	-3.7367	-9.1369	-13.7445	-19.92	-22.871	-28.7543
Plate 9	0	-2.8087	-7.997	-12.0521	-16.9538	-19.2157	-23.4495
Plate 10	0	-2.2565	-6.9823	-9.3699	-13.3051	-14.8017	-17.8953
Plate 11	0	-1.9346	-5.3419	-7.5475	-9.8713	-10.5055	-11.7857
Plate 12	0	-1.0701	-3.021	-3.7884	-5.7006	-5.4477	-5.5335

	35 mm	**40 mm**	**45 mm**	**50 mm**	**55 mm**	**60 mm**	**65 mm**
Plate 7	-32.4688	-38.3669	-44.6739	-50.8809	-55.0819	-59.0166	-65.0769
Plate 8	-32.6175	-38.6748	-44.4827	-50.6977	-55.5871	-59.2896	-64.5175
Plate 9	-27.0326	-30.8168	-34.2644	-38.7755	-42.4599	-44.389	-48.2522
Plate 10	-21.144	-24.2795	-26.4031	-30.0606	-32.5164	-33.2059	-36.6713
Plate 11	-13.8657	-17.7735	-19.0257	-20.0686	-21.8227	-21.056	-24.4975
Plate 12	-6.6427	-9.5985	-8.8447	-10.3129	-10.9286	-8.9244	-11.8859

TABLE C.15: Exp. 1 Phase 2: Deflection errors of the range cameras($\delta Z_{TLS} - \delta Z_{RC}$)

	0 mm	**5 mm**	**10 mm**	**15 mm**	**20 mm**	**25 mm**	**30 mm**
Plate 1	0	1.421	0.251	1.429	-0.949	-1.220	-0.341
Plate 2	0	1.097	0.162	0.939	-0.845	-0.498	-0.924
Plate 3	0	0.911	0.143	0.788	-0.529	0.005	-1.199
Plate 4	0	0.432	0.402	1.843	0.741	1.734	-0.262
Plate 5	0	0.489	0.434	0.539	0.647	2.756	-0.795
Plate 6	0	0.578	-0.025	0.046	0.123	3.406	-1.731
Plate 7	0	-0.061	0.132	0.041	0.929	3.192	-0.511
Plate 8	0	-0.443	-0.064	-0.380	1.213	-0.535	0.375
Plate 9	0	-0.903	-0.134	-0.271	0.955	-0.449	-0.035
Plate 10	0	-0.833	0.291	-0.732	0.437	-0.825	-0.574
Plate 11	0	-0.296	0.501	0.341	0.827	-0.383	-0.959
Plate 12	0	-0.275	0.242	-0.283	0.705	-0.448	-1.295
σ	**0.00**	**0.76**	**0.20**	**0.78**	**0.74**	**1.70**	**0.58**

35 mm	**40 mm**	**45 mm**	**50 mm**	**55 mm**	**60 mm**	**65 mm**	σ**(mm)**
-0.1231	0.733	1.643	0.121	-1.014	0.355	2.358	**1.08**
-0.1870	0.199	1.097	0.038	-1.244	-0.212	2.047	**0.91**
0.0480	0.265	0.923	0.052	-1.143	-1.132	1.029	**0.77**
1.3501	0.736	1.762	0.765	-0.589	-0.772	1.905	**0.91**
1.3959	0.364	1.901	0.940	-0.459	-0.986	1.990	**1.08**
0.9818	-0.418	1.489	0.243	-0.957	-1.333	1.505	**1.31**
0.5165	-0.429	1.224	0.584	0.372	-0.655	1.557	**1.01**
-0.6251	0.319	-0.105	0.581	-0.351	-1.042	-0.130	**0.57**
-0.2832	-0.229	-0.438	0.249	0.297	-0.868	-0.186	**0.47**
-0.2122	0.175	-0.472	0.315	0.078	-1.475	-0.458	**0.55**
-0.7819	1.252	0.726	-0.118	-0.166	-2.384	-0.447	**0.90**
-1.1324	0.911	-0.757	-0.233	-0.459	-3.126	-0.904	**1.21**
0.82	**0.52**	**0.95**	**0.36**	**0.55**	**0.92**	**1.19**	**0.98**

C.6 Experiment 1: Phase 3 data

TABLE C.16: Exp. 1 Phase 3: Deflection values of the TLS

	65 mm	**60 mm**	**55 mm**	**50 mm**	**Permanent damage**	**Zero Load**
Plate 1	-0.6226	-0.6097	-0.499	-0.4682	-0.3637	0
Plate 2	-13.0062	-11.6474	-10.3963	-9.275	-9.1895	0
Plate 3	-24.7653	-22.4451	-20.3118	-18.0517	-17.8836	0
Plate 4	-35.9313	-32.5873	-29.4522	-26.3136	-26.0796	0
Plate 5	-47.0753	-42.8698	-38.9614	-34.9204	-34.6448	0
Plate 6	-58.506	-53.6469	-49.0537	-44.3165	-44.0088	0
Plate 7	-65.4537	-60.2241	-55.3858	-50.0676	**-49.7663**	0
Plate 8	-65.6091	-60.7377	-56.1371	-51.307	-51.0873	0
Plate 9	-49.2308	-44.9951	-40.9989	-36.85	-36.5859	0
Plate 10	-37.7636	-34.2562	-31.0494	-27.7654	-27.5488	0
Plate 11	-25.4828	-23.1007	-20.9159	-18.6135	-18.4257	0
Plate 12	-13.0936	-11.8726	-10.6704	-9.4499	-9.3293	0
Plate 13	-0.1524	-0.1411	-0.079	-0.0835	-0.038	0

TABLE C.17: Exp. 1 Phase 3: Deflection values of the RC 1

	65 mm	**60 mm**	**55 mm**	**50 mm**	**Permanent damage**	**Zero Load**
Plate 1	2.2323	5.1648	0.567	2.3697	3.3509	0
Plate 2	-9.9096	-8.2827	-8.1121	-5.222	-4.7437	0
Plate 3	-21.2113	-18.9957	-17.4601	-14.4191	-13.8129	0
Plate 4	-33.4452	-29.7899	-27.8248	-23.0606	-23.1199	0
Plate 5	-44.3391	-40.4185	-36.6371	-31.3997	-31.9381	0
Plate 6	-55.2582	-50.7603	-46.0206	-39.3749	-40.6989	0
Plate 7	-62.2845	-57.9836	-55.2291	-43.8608	**-46.1798**	0

TABLE C.18: Exp. 1 Phase 3: Deflection values of the RC 2

	65 mm	**60 mm**	**55 mm**	**50 mm**	**Permanent damage**	**Zero Load**
Plate 7	-65.6712	-61.4676	-56.9521	-52.6467	**-48.7709**	0
Plate 8	-66.3495	-62.0743	-57.6211	-53.4218	-51.3044	0
Plate 9	-51.2549	-46.5166	-41.7691	-37.7697	-36.3221	0
Plate 10	-40.6342	-36.4706	-32.5164	-29.336	-28.511	0
Plate 11	-27.2434	-24.8584	-22.1375	-20.4591	-19.8814	0
Plate 12	-14.0373	-12.4833	-10.8196	-9.6562	-9.2227	0

C.7 Experiment 2: Phase 1 data

TABLE C.19: Exp. 2 Phase 1: Centroid measurement of the TLS

	0 mm	**3 mm**	**0 mm**	**3 mm**	**0 mm**
Plate 1	3550.932	3550.718	3550.904	3550.771	3550.915
Plate 2	3549.454	3548.782	3549.595	3548.704	3549.449
Plate 3	3546.633	3545.470	3546.917	3545.416	3546.609
Plate 4	3545.856	3544.204	3546.204	3544.148	3545.843
Plate 5	3545.214	3543.111	3545.721	3543.204	3545.219
Plate 6	3545.017	3542.694	3545.593	3542.704	3545.054
Plate 7	3536.882	3534.585	3537.445	3534.512	3536.883
Plate 8	3543.646	3541.242	3544.146	3541.312	3543.595
Plate 9	3543.971	3541.966	3544.445	3541.902	3543.930
Plate 10	3543.549	3541.994	3543.898	3541.868	3543.581
Plate 11	3544.289	3542.817	3544.429	3542.968	3544.210
Plate 12	3543.843	3543.235	3543.800	3543.032	3543.787
Plate 13	3542.028	3541.973	3541.933	3541.969	3541.982

TABLE C.20: Exp. 2 Phase 1: Deflection values of the TLS

	0 mm	**3 mm**	**0 mm**	**3 mm**	**0 mm**
Plate 1	0.0	-0.214	-0.028	-0.161	-0.016
Plate 2	0.0	-0.671	0.142	-0.750	-0.005
Plate 3	0.0	-1.162	0.285	-1.217	-0.023
Plate 4	0.0	-1.652	0.348	-1.707	-0.013
Plate 5	0.0	-2.102	0.508	-2.010	0.005
Plate 6	0.0	-2.323	0.576	-2.313	0.037
Plate 7	0.0	-2.297	0.563	-2.370	0.001
Plate 8	0.0	-2.404	0.500	-2.333	-0.051
Plate 9	0.0	-2.005	0.475	-2.068	-0.040
Plate 10	0.0	-1.555	0.349	-1.681	0.032
Plate 11	0.0	-1.472	0.141	-1.320	-0.079
Plate 12	0.0	-0.608	-0.043	-0.810	-0.056
Plate 13	0.0	-0.055	-0.095	-0.059	-0.046

TABLE C.21: Exp. 2 Phase 1: Centroid measurement of the RC 1

	0 mm	**3 mm**	**0 mm**	**3 mm**	**0 mm**
Plate 1	-2159.970	-2157.902	-2157.703	-2158.593	-2157.390
Plate 2	-2156.878	-2156.200	-2155.151	-2157.127	-2155.083
Plate 3	-2156.353	-2155.878	-2154.427	-2156.239	-2154.036
Plate 4	-2154.531	-2153.632	-2151.694	-2154.217	-2151.744
Plate 5	-2151.934	-2150.405	-2148.327	-2151.273	-2148.509
Plate 6	-2149.503	-2147.857	-2145.344	-2148.166	-2145.565
Plate 7	-2153.823	-2150.997	-2148.240	-2151.146	-2148.488

TABLE C.22: Exp. 2 Phase 1: Deflection values of the RC 1

	0 mm	**3 mm**	**0 mm**	**3 mm**	**0 mm**
Plate 1	0.000	2.068	2.267	1.377	2.580
Plate 2	0.000	0.677	1.726	-0.249	1.795
Plate 3	0.000	0.475	1.926	0.114	2.317
Plate 4	0.000	0.899	2.837	0.314	2.788
Plate 5	0.000	1.530	3.607	0.661	3.425
Plate 6	0.000	1.647	4.160	1.337	3.938
Plate 7	0.000	2.826	5.582	2.677	5.334

TABLE C.23: Exp. 2 Phase 1: Centroid measurement of the RC 2

	0 mm	**3 mm**	**0 mm**	**3 mm**	**0 mm**
Plate 7	-2172.9725	-2176.106	-2172.936	-2176.026	-2174.183
Plate 8	-2156.7979	-2160.065	-2157.544	-2159.839	-2158.043
Plate 9	-2148.7811	-2151.273	-2149.470	-2151.378	-2149.726
Plate 10	-2141.3927	-2143.486	-2142.228	-2143.830	-2142.288
Plate 11	-2133.2166	-2135.101	-2133.938	-2135.001	-2133.691
Plate 12	-2118.9947	-2120.369	-2120.002	-2120.028	-2119.363

TABLE C.24: Exp. 2 Phase 1: Deflection values of the RC 2

	0 mm	**3 mm**	**0 mm**	**3 mm**	**0 mm**
Plate 7	0	-3.1333	0.0364	-3.054	-1.2103
Plate 8	0	-3.2669	-0.7465	-3.0409	-1.2453
Plate 9	0	-2.4915	-0.6884	-2.5969	-0.9449
Plate 10	0	-2.0937	-0.8352	-2.4374	-0.8957
Plate 11	0	-1.8843	-0.7213	-1.7845	-0.4749
Plate 12	0	-1.3748	-1.0077	-1.0332	-0.3685

TABLE C.25: Exp. 2 Phase 1: Deflection errors of the RC 2 for the no interference case

	0 mm	**3 mm**	**0 mm**	**3 mm**	**0 mm**
Plate 7	0	0.561	0.867	0.141	0.222
Plate 8	0	0.437	0.436	0.282	0.167
Plate 9	0	0.098	0.492	0.389	0.539
Plate 10	0	-0.118	0.180	0.079	0.442
Plate 11	0	0.367	0.170	0.152	0.706
Plate 12	0	0.273	-0.599	0.121	0.648

C.8 Experiment 2: Phase 2 data

TABLE C.26: Exp. 2 Phase 2: Centroid measurements of the TLS

	0 mm	**5 mm**	**10 mm**	**15 mm**	**20 mm**	**25 mm**	**30 mm**
Plate 1	3542.028	3541.874	3541.86	3541.826	3541.897	3541.905	3541.791
Plate 2	3543.843	3542.519	3541.202	3539.961	3539.018	3538.013	3536.732
Plate 3	3544.289	3541.990	3539.547	3536.988	3535.032	3532.888	3528.423
Plate 4	3543.549	3540.377	3536.973	3533.439	3530.541	3527.436	3522.992
Plate 5	3543.971	3540.155	3535.911	3531.437	3527.683	3523.758	3514.915
Plate 6	3543.646	3539.380	3534.421	3529.479	3524.728	3519.760	3510.871
Plate 7	3536.882	3532.502	3527.469	3522.345	3517.346	3512.306	3505.101
Plate 8	3545.017	3540.782	3535.944	3531.059	3526.355	3521.565	3518.241
Plate 9	3545.214	3541.441	3537.190	3532.950	3529.070	3525.200	3522.009
Plate 10	3545.856	3542.798	3539.287	3535.916	3533.005	3530.039	3528.194
Plate 11	3546.633	3544.418	3541.95	3539.650	3537.697	3535.739	3534.531
Plate 12	3549.454	3548.189	3546.911	3545.673	3544.678	3543.708	3543.134
Plate 13	3550.932	3550.728	3550.646	3550.680	3550.735	3550.833	3550.824

	35 mm	**40 mm**	**45 mm**	**50 mm**	**55 mm**	**60 mm**	**65 mm**
Plate 1	3541.879	3541.807	3541.570	3541.682	3541.559	3541.53	3541.629
Plate 2	3536.541	3535.879	3534.606	3533.167	3532.725	3531.655	3530.584
Plate 3	3527.552	3525.585	3522.950	3522.483	3519.144	3516.878	3514.564
Plate 4	3521.852	3519.827	3515.546	3513.659	3510.215	3507.328	3504.486
Plate 5	3513.278	3511.804	3506.937	3504.764	3499.710	3496.142	3492.534
Plate 6	3508.676	3504.028	3498.965	3496.650	3490.298	3486.162	3481.804
Plate 7	3502.791	3498.032	3492.995	3488.414	3483.387	3478.339	3473.554
Plate 8	3516.527	3512.503	3508.353	3504.346	3500.151	3496.055	3492.088
Plate 9	3520.542	3517.393	3514.079	3511.496	3507.553	3504.318	3501.167
Plate 10	3527.149	3524.823	3522.314	3520.494	3517.479	3515.075	3512.717
Plate 11	3533.828	3532.247	3530.609	3529.651	3527.400	3525.845	3524.268
Plate 12	3542.788	3542.054	3541.195	3540.190	3539.644	3538.935	3538.155
Plate 13	3550.824	3550.874	3550.862	3549.885	3550.958	3551.034	3551.101

TABLE C.27: Exp. 2 Phase 2: Deflection (δZ) values of the TLS

	0 mm	**5 mm**	**10 mm**	**15 mm**	**20 mm**	**25 mm**	**30 mm**
Plate 1	0	-0.154	-0.168	-0.202	-0.131	-0.122	-0.237
Plate 2	0	-1.324	-2.640	-3.882	-4.824	-5.829	-7.110
Plate 3	0	-2.298	-4.742	-7.300	-9.256	-11.401	-15.865
Plate 4	0	-3.172	-6.576	-10.110	-13.008	-16.113	-20.557
Plate 5	0	-3.816	-8.060	-12.534	-16.288	-20.213	-29.056
Plate 6	0	-4.266	-9.225	-14.167	-18.918	-23.886	-32.775
Plate 7	0	-4.380	-9.413	-14.537	-19.536	-24.576	-31.781
Plate 8	0	-4.236	-9.073	-13.959	-18.662	-23.452	-26.776
Plate 9	0	-3.773	-8.023	-12.264	-16.144	-20.013	-23.205
Plate 10	0	-3.058	-6.569	-9.940	-12.851	-15.817	-17.662
Plate 11	0	-2.215	-4.683	-6.982	-8.936	-10.894	-12.102
Plate 12	0	-1.265	-2.543	-3.780	-4.776	-5.745	-6.320
Plate 13	0	-0.204	-0.286	-0.251	-0.197	-0.098	-0.108

	35 mm	**40 mm**	**45 mm**	**50 mm**	**55 mm**	**60 mm**	**65 mm**
Plate 1	-0.148	-0.220	-0.457	-0.345	-0.469	-0.498	-0.399
Plate 2	-7.302	-7.963	-9.236	-10.676	-11.117	-12.188	-13.259
Plate 3	-16.737	-18.704	-21.339	-21.806	-25.144	-27.410	-29.724
Plate 4	-21.697	-23.723	-28.003	-29.890	-33.334	-36.222	-39.063
Plate 5	-30.692	-32.167	-37.034	-39.207	-44.260	-47.829	-51.436
Plate 6	-34.970	-39.618	-44.680	-46.995	-53.348	-57.484	-61.842
Plate 7	-34.091	-38.851	-43.887	-48.468	-53.495	-58.543	**-63.329**
Plate 8	-28.490	-32.515	-36.664	-40.671	-44.866	-48.963	-52.930
Plate 9	-24.672	-27.821	-31.135	-33.718	-37.661	-40.896	-44.047
Plate 10	-18.707	-21.033	-23.541	-25.361	-28.377	-30.781	-33.139
Plate 11	-12.805	-14.386	-16.024	-16.982	-19.232	-20.788	-22.365
Plate 12	-6.665	-7.400	-8.258	-9.264	-9.809	-10.519	-11.299
Plate 13	-0.108	-0.058	-0.070	-1.047	0.026	0.102	0.170

TABLE C.28: Exp. 2 Phase 2:: Centroid measurements of the RC 1

	0 mm	**5 mm**	**10 mm**	**15 mm**	**20 mm**	**25 mm**	**30 mm**
Plate 1	-2157.527	-2157.592	-2158.978	-2158.330	-2157.751	-2158.363	-2157.947
Plate 2	-2155.083	-2156.725	-2159.046	-2159.898	-2160.208	-2161.517	-2161.872
Plate 3	-2154.036	-2155.638	-2159.237	-2161.146	-2162.278	-2164.628	-2168.636
Plate 4	-2151.744	-2154.302	-2158.425	-2161.106	-2163.443	-2166.564	-2170.832
Plate 5	-2148.509	-2151.429	-2156.328	-2160.200	-2162.704	-2167.084	-2176.033
Plate 6	-2145.565	-2148.723	-2154.704	-2158.469	-2162.815	-2167.768	-2176.072
Plate 7	-2148.488	-2152.181	-2158.993	-2162.086	-2165.952	-2170.375	-2177.910

	35 mm	**40 mm**	**45 mm**	**50 mm**	**55 mm**	**60 mm**	**65 mm**
Plate 1	-2159.664	-2159.100	-2158.741	-2157.656	-2156.916	-2159.307	-2159.982
Plate 2	-2163.736	-2164.845	-2165.349	-2165.008	-2164.870	-2167.725	-2168.838
Plate 3	-2170.921	-2172.754	-2173.995	-2174.256	-2175.021	-2180.098	-2182.610
Plate 4	-2173.000	-2174.886	-2178.144	-2179.400	-2181.119	-2186.383	-2189.028
Plate 5	-2178.457	-2179.471	-2184.755	-2186.910	-2188.674	-2194.427	-2197.550
Plate 6	-2179.270	-2184.447	-2189.977	-2192.108	-2195.286	-2201.209	-2205.792
Plate 7	-2180.088	-2186.102	-2192.759	-2195.021	-2197.553	-2204.219	-2208.496

TABLE C.29: Exp. 2 Phase 2: Deflection (δZ) values of the RC 1

	0 mm	**5 mm**	**10 mm**	**15 mm**	**20 mm**	**25 mm**	**30 mm**
Plate 1	0.000	-0.065	-1.450	-0.803	-0.224	-0.836	-0.420
Plate 2	0.000	-1.642	-3.963	-4.815	-5.125	-6.434	-6.789
Plate 3	0.000	-1.602	-5.201	-7.111	-8.243	-10.593	-14.600
Plate 4	0.000	-2.558	-6.682	-9.363	-11.700	-14.820	-19.088
Plate 5	0.000	-2.920	-7.819	-11.691	-14.195	-18.575	-27.524
Plate 6	0.000	-3.158	-9.139	-12.904	-17.250	-22.203	-30.507
Plate 7	0.000	-3.693	-10.505	-13.598	-17.463	-21.887	-29.422

	35 mm	**40 mm**	**45 mm**	**50 mm**	**55 mm**	**60 mm**	**65 mm**
Plate 1	-2.136	-1.573	-1.214	-0.128	0.611	-1.780	-2.454
Plate 2	-8.653	-9.762	-10.266	-9.925	-9.787	-12.642	-13.755
Plate 3	-16.886	-18.718	-19.959	-20.221	-20.985	-26.062	-28.575
Plate 4	-21.257	-23.142	-26.400	-27.656	-29.375	-34.639	-37.285
Plate 5	-29.948	-30.962	-36.245	-38.401	-40.165	-45.917	-49.040
Plate 6	-33.705	-38.882	-44.412	-46.543	-49.721	-55.644	-60.227
Plate 7	-31.600	-37.614	-44.271	-46.532	-49.065	-55.731	**-60.008**

TABLE C.30: Exp. 2 Phase 2: Centroid measurements of the RC 2

	0 mm	**5 mm**	**10 mm**	**15 mm**	**20 mm**	**25 mm**	**30 mm**
Plate 7	-2175.743	-2177.906	-2178.259	-2191.670	-2196.151	-2207.271	-2208.718
Plate 8	-2158.646	-2162.185	-2164.032	-2174.525	-2179.082	-2186.116	-2186.160
Plate 9	-2149.899	-2153.073	-2155.992	-2163.593	-2167.376	-2171.389	-2173.496
Plate 10	-2142.190	-2144.784	-2148.096	-2153.580	-2156.008	-2157.801	-2159.975
Plate 11	-2133.649	-2135.848	-2137.928	-2141.483	-2142.351	-2143.237	-2145.439
Plate 12	-2119.190	-2120.708	-2121.968	-2123.283	-2124.669	-2122.964	-2124.646

	35 mm	**40 mm**	**45 mm**	**50 mm**	**55 mm**	**60 mm**	**65 mm**
Plate 7	-2211.984	-2213.119	-2218.791	-2224.089	-2231.640	-2236.064	-2242.039
Plate 8	-2189.306	-2190.987	-2195.637	-2198.759	-2205.072	-2208.507	-2213.343
Plate 9	-2175.432	-2178.470	-2181.070	-2183.914	-2188.543	-2191.547	-2195.541
Plate 10	-2161.403	-2164.035	-2167.442	-2168.496	-2171.314	-2173.106	-2176.048
Plate 11	-2145.915	-2147.445	-2150.168	-2151.212	-2152.425	-2153.722	-2155.108
Plate 12	-2124.994	-2125.958	-2127.545	-2127.489	-2128.660	-2129.155	-2130.012

TABLE C.31: Exp. 2 Phase 2: Deflection (δZ) values of the RC 2

	0 mm	**5 mm**	**10 mm**	**15 mm**	**20 mm**	**25 mm**	**30 mm**
Plate 7	0.000	-2.163	-2.516	-15.927	-20.408	-31.527	-32.975
Plate 8	0.000	-3.539	-5.386	-15.879	-20.436	-27.470	-27.514
Plate 9	0.000	-3.174	-6.093	-13.694	-17.477	-21.490	-23.597
Plate 10	0.000	-2.594	-5.906	-11.390	-13.818	-15.611	-17.785
Plate 11	0.000	-2.199	-4.279	-7.834	-8.702	-9.588	-11.791
Plate 12	0.000	-1.518	-2.778	-4.093	-5.479	-3.773	-5.456

	35 mm	**40 mm**	**45 mm**	**50 mm**	**55 mm**	**60 mm**	**65 mm**
Plate 7	-36.240	-37.376	-43.048	-48.345	-55.897	-60.321	-66.296
Plate 8	-30.660	-32.340	-36.991	-40.113	-46.426	-49.861	-54.696
Plate 9	-25.533	-28.571	-31.171	-34.015	-38.644	-41.648	-45.642
Plate 10	-19.213	-21.845	-25.253	-26.306	-29.124	-30.916	-33.858
Plate 11	-12.266	-13.796	-16.519	-17.563	-18.777	-20.073	-21.459
Plate 12	-5.804	-6.767	-8.355	-8.298	-9.469	-9.965	-10.821

TABLE C.32: Exp. 2 Phase 2: Deflection errors of the range cameras($\delta Z_{TLS} - \delta Z_{RC}$)

	0 mm	**5 mm**	**10 mm**	**15 mm**	**20 mm**	**25 mm**	**30 mm**
Plate 1	0	-0.089	1.283	0.601	0.093	0.713	0.183
Plate 2	0	0.318	1.323	0.933	0.300	0.605	-0.321
Plate 3	0	-0.696	0.459	-0.189	-1.013	-0.808	-1.265
Plate 4	0	-0.614	0.105	-0.747	-1.308	-1.292	-1.468
Plate 5	0	-0.896	-0.241	-0.843	-2.093	-1.638	-1.532
Plate 6	0	-1.108	-0.085	-1.263	-1.668	-1.683	-2.268
Plate 7	0	-1.452	-2.902	0.226	-0.601	2.131	-0.583
Plate 8	0	-0.697	-3.687	1.920	1.773	4.018	0.738
Plate 9	0	-0.599	-1.931	1.431	1.333	1.477	0.392
Plate 10	0	-0.464	-0.663	1.450	0.967	-0.206	0.123
Plate 11	0	-0.017	-0.404	0.852	-0.234	-1.306	-0.311
Plate 12	0	0.253	0.235	0.312	0.703	-1.972	-0.864
σ	0	0.537	1.554	1.001	1.225	1.839	0.904

35 mm	**40 mm**	**45 mm**	**50 mm**	**55 mm**	**60 mm**	**65 mm**	σ**(mm)**
1.988	1.352	0.757	-0.217	-1.080	1.282	2.056	**0.907**
1.351	1.798	1.030	-0.750	-1.330	0.454	0.496	**0.877**
0.149	0.015	-1.380	-1.585	-4.159	-1.348	-1.149	**1.153**
-0.441	-0.580	-1.602	-2.234	-3.958	-1.583	-1.779	**1.014**
-0.744	-1.205	-0.788	-0.807	-4.095	-1.911	-2.396	**1.004**
-1.265	-0.736	-0.269	-0.452	-3.627	-1.840	-1.614	**0.938**
-0.171	-1.356	-0.228	-1.029	-1.015	-0.517	-0.176	**1.140**
2.169	-0.174	0.326	-0.559	1.559	0.897	1.767	**1.856**
0.862	0.750	0.035	0.298	0.984	0.753	1.595	**0.980**
0.507	0.813	1.711	0.945	0.747	0.135	0.719	**0.710**
-0.539	-0.590	0.495	0.581	-0.456	-0.715	-0.906	**0.615**
-0.861	-0.632	0.097	-0.966	-0.340	-0.554	-0.478	**0.713**
1.135	**1.009**	**0.960**	**0.893**	**2.082**	**1.114**	**1.486**	**1.305**

TABLE C.33: Exp. 2 Phase 2: Deflection errors of the range cameras($\delta Z_{TLS} - \delta Z_{RC}$) for the no-interference case

	Plate 7	**Plate 8**	**Plate 9**	**Plate 10**	**Plate 11**	**Plate 12**
0 mm	0	0	0	0	0	0
5 mm	-0.142	0.505	-0.131	0.401	-0.134	0.002
10 mm	0.394	0.287	0.134	-0.097	0.042	0.273
15 mm	-0.601	0.625	0.922	0.929	0.920	0.077
20 mm	-1.121	0.515	0.239	0.427	-0.168	0.359
25 mm	-1.010	1.347	0.674	0.741	0.259	0.371
30 mm	-0.575	1.243	0.584	0.362	-0.105	-0.226
35 mm	-0.721	1.406	0.691	0.363	-0.191	-0.466
40 mm	0.151	1.364	1.129	1.071	-0.084	-0.634
45 mm	0.713	0.788	0.460	1.291	0.375	-0.110
50 mm	-0.471	0.333	0.770	1.157	0.623	-0.467
55 mm	-0.919	0.600	-0.073	0.373	-0.704	-0.192
60 mm	-0.545	0.634	1.099	0.775	-0.408	-0.148
65 mm	-0.582	1.205	1.548	0.266	-0.687	-0.146

TABLE C.34: Exp. 2 Phase 2: Deflection errors of the range cameras ($\delta Z_{TLS} - \delta Z_{RC}$) for the with-interference case

	Plate 7	**Plate 8**	**Plate 9**	**Plate 10**	**Plate 11**	**Plate 12**
0 mm	0	0	0	0	0	0
5 mm	-1.452	-0.697	-0.599	-0.464	-0.017	0.253
10 mm	-2.902	-3.687	-1.931	-0.663	-0.404	0.235
15 mm	0.226	1.920	1.431	1.450	0.852	0.312
20 mm	-0.601	1.773	1.333	0.967	-0.234	0.703
25 mm	2.131	4.018	1.477	-0.206	-1.306	-1.972
30 mm	-0.583	0.738	0.392	0.123	-0.311	-0.864
35 mm	-0.171	2.169	0.862	0.507	-0.539	-0.861
40 mm	-1.356	-0.174	0.750	0.813	-0.590	-0.632
45 mm	-0.228	0.326	0.035	1.711	0.495	0.097
50 mm	-1.029	-0.559	0.298	0.945	0.581	-0.966
55 mm	-1.015	1.559	0.984	0.747	-0.456	-0.340
60 mm	-0.517	0.897	0.753	0.135	-0.715	-0.554
65 mm	-0.176	1.767	1.595	0.719	-0.906	-0.478

C.9 Experiment 2: Phase 3 data

Table C.35: Exp. 2 Phase 3: Deflection values of the TLS

	Zero Load	**65 mm**	**60 mm**	**55 mm**	**50 mm**	**Permanent damage**
Plate 1	0	-0.292	-0.233	-0.018	-0.206	-0.059
Plate 2	0	-13.221	-12.548	-11.228	-10.447	-9.870
Plate 3	0	-29.911	-28.534	-24.393	-21.797	-20.826
Plate 4	0	-39.426	-37.665	-32.182	-28.996	-27.949
Plate 5	0	-51.923	-49.794	-43.120	-39.180	-37.785
Plate 6	0	-62.399	-59.746	-52.516	-47.855	-46.225
Plate 7	0	-63.896	-60.891	-53.739	-48.858	**-47.077**
Plate 8	0	-53.478	-51.059	-43.804	-39.090	-37.463
Plate 9	0	-44.538	-42.605	-36.112	-32.025	-30.608
Plate 10	0	-33.511	-32.051	-26.915	-23.759	-22.647
Plate 11	0	-22.659	-21.681	-18.090	-15.886	-15.108
Plate 12	0	-11.461	-10.970	-9.087	-7.954	-7.508
Plate 13	0	0.200	0.123	0.220	0.166	0.071

Table C.36: Exp. 2 Phase 3: Deflection values of the RC 1

	0 mm	**65 mm**	**60 mm**	**55 mm**	**50 mm**	**Permanent damage**
Plate 1	0	-2.454	-1.860	1.592	-0.972	-1.116
Plate 2	0	-13.755	-12.903	-8.570	-10.231	-10.352
Plate 3	0	-28.575	-25.617	-20.250	-19.888	-19.817
Plate 4	0	-37.285	-34.367	-27.878	-27.272	-27.904
Plate 5	0	-49.040	-45.742	-37.843	-37.629	-37.762
Plate 6	0	-60.227	-56.092	-45.857	-46.950	-47.685
Plate 7	0	-60.008	-56.739	-43.301	-46.439	**-48.194**

Table C.37: Exp. 2 Phase 3: Deflection values of the RC 2

	0 mm	**65 mm**	**60 mm**	**55 mm**	**50 mm**	**Permanent damage**
Plate 7	0	-60.848	-56.219	-76.626	-45.864	**-43.026**
Plate 8	0	-54.696	-49.403	-63.842	-39.370	-36.859
Plate 9	0	-45.591	-40.547	-46.931	-32.430	-30.140
Plate 10	0	-33.858	-30.389	-31.865	-24.807	-23.450
Plate 11	0	-21.459	-19.317	-18.851	-15.179	-15.099
Plate 12	0	-10.821	-9.654	-7.832	-7.383	-7.533

C.10 Accuracy in x-coordinate

TABLE C.38: X values of the TLS

	Plate 1	**Plate 2**	**Plate 3**	**Plate 4**	**Plate 5**	**Plate 6**
0 mm	2677.993	2927.366	3176.739	3426.112	3675.485	3924.858
5 mm	2677.781	2927.305	3176.829	3426.353	3675.877	3925.401
10 mm	2677.280	2927.116	3176.952	3426.788	3676.624	3926.460
15 mm	2677.145	2927.167	3177.189	3427.211	3677.233	3927.255
20 mm	2677.333	2927.524	3177.716	3427.907	3678.099	3928.291
25 mm	2677.781	2928.188	3178.596	3429.004	3679.411	3929.819
30 mm	2678.322	2928.824	3179.327	3429.830	3680.332	3930.835
35 mm	2678.803	2929.473	3180.143	3430.812	3681.482	3932.152
40 mm	2678.352	2929.171	3179.990	3430.809	3681.628	3932.447
45 mm	2679.045	2930.006	3180.967	3431.928	3682.889	3933.849
50 mm	2680.401	2931.405	3182.408	3433.411	3684.415	3935.418
55 mm	2680.605	2931.715	3182.824	3433.933	3685.042	3936.152
60 mm	2681.416	2932.491	3183.565	3434.640	3685.714	3936.788
65 mm	2682.613	2933.696	3184.779	3435.863	3686.946	3938.029

Plate 7	**Plate 8**	**Plate 9**	**Plate 10**	**Plate 11**	**Plate 12**	**Plate 13**
4174.230	4423.603	4672.976	4922.349	5171.722	5421.095	5670.468
4174.925	4424.449	4673.973	4923.497	5173.021	5422.545	5672.069
4176.295	4426.131	4675.967	4925.803	5175.639	5425.474	5675.310
4177.278	4427.300	4677.322	4927.344	5177.366	5427.388	5677.410
4178.482	4428.674	4678.865	4929.057	5179.248	5429.44	5679.632
4180.227	4430.634	4681.042	4931.449	5181.857	5432.265	5682.672
4181.338	4431.840	4682.343	4932.846	5183.348	5433.851	5684.354
4182.822	4433.492	4684.162	4934.831	5185.501	5436.171	5686.841
4183.266	4434.085	4684.904	4935.722	5186.542	5437.360	5688.180
4184.810	4435.771	4686.732	4937.693	5188.654	5439.614	5690.575
4186.421	4437.425	4688.428	4939.431	5190.435	5441.438	5692.441
4187.261	4438.370	4689.479	4940.589	5191.698	5442.807	5693.917
4187.863	4438.937	4690.011	4941.086	5192.160	5443.234	5694.309
4189.112	4440.195	4691.278	4942.361	5193.445	5444.528	5695.611

TABLE C.39: X values of the range camera

	Plate 1	**Plate 2**	**Plate 3**	**Plate 4**	**Plate 5**	**Plate 6**
0 mm	-731.543	-505.747	-279.952	-54.156	171.640	397.435
5 mm	-733.348	-507.287	-281.225	-55.164	170.898	396.959
10 mm	-739.559	-513.492	-287.426	-61.359	164.707	390.774
15 mm	-735.394	-509.089	-282.783	-56.477	169.828	396.134
20 mm	-736.958	-510.538	-284.118	-57.698	168.722	395.142
25 mm	-743.602	-516.674	-289.745	-62.817	164.112	391.040
30 mm	-733.148	-506.447	-279.746	-53.045	173.656	400.357
35 mm	-739.741	-512.744	-285.747	-58.750	168.246	395.243
40 mm	-730.667	-503.472	-276.278	-49.083	178.112	405.307
45 mm	-731.492	-503.923	-276.353	-48.784	178.786	406.355
50 mm	-735.121	-507.944	-280.767	-53.590	173.588	400.765
55 mm	-733.302	-506.334	-279.366	-52.398	174.571	401.539
60 mm	-732.824	-505.889	-278.953	-52.018	174.918	401.853
65 mm	-726.772	-499.801	-272.829	-45.858	181.114	408.085

	Plate 7	**Plate 8**	**Plate 9**	**Plate 10**	**Plate 11**	**Plate 12**
0 mm	623.231	856.345	1089.459	1322.573	1555.687	1788.801
5 mm	623.021	856.523	1090.024	1323.526	1557.027	1790.528
10 mm	616.840	850.562	1084.284	1318.006	1551.728	1785.449
15 mm	622.440	855.590	1088.740	1321.890	1555.040	1788.190
20 mm	621.562	855.159	1088.757	1322.354	1555.951	1789.549
25 mm	617.969	851.320	1084.671	1318.022	1551.374	1784.725
30 mm	627.058	860.715	1094.371	1328.028	1561.685	1795.341
35 mm	622.240	855.702	1089.164	1322.626	1556.088	1789.550
40 mm	632.501	866.865	1101.228	1335.592	1569.956	1804.319
45 mm	633.924	867.930	1101.936	1335.942	1569.948	1803.954
50 mm	627.942	862.605	1097.267	1331.929	1566.592	1801.254
55 mm	628.507	862.823	1097.138	1331.454	1565.770	1800.085
60 mm	628.789	862.765	1096.741	1330.717	1564.693	1798.669
65 mm	635.056	869.419	1103.782	1338.145	1572.508	1806.871

TABLE C.40: TLS: Length of the thin plates from Plate 1

	Plate 1	**Plate 2**	**Plate 3**	**Plate 4**	**Plate 5**	**Plate 6**	**Plate 7**
0 mm	0	249.37	498.75	748.12	997.49	1246.86	1496.24
5 mm	0	249.52	499.05	748.57	998.10	1247.62	1497.14
10 mm	0	249.84	499.67	749.51	999.34	1249.18	1499.01
15 mm	0	250.02	500.04	750.07	1000.09	1250.11	1500.13
20 mm	0	250.19	500.38	750.57	1000.77	1250.96	1501.15
25 mm	0	250.41	500.82	751.22	1001.63	1252.04	1502.45
30 mm	0	250.50	501.01	751.51	1002.01	1252.51	1503.02
35 mm	0	250.67	501.34	752.01	1002.68	1253.35	1504.02
40 mm	0	250.82	501.64	752.46	1003.28	1254.10	1504.91
45 mm	0	250.96	501.92	752.88	1003.84	1254.80	1505.76
50 mm	0	251.00	502.01	753.01	1004.01	1255.02	1506.02
55 mm	0	251.11	502.22	753.33	1004.44	1255.55	1506.66
60 mm	0	251.07	502.15	753.22	1004.30	1255.37	1506.45
65 mm	0	251.08	502.17	753.25	1004.33	1255.42	1506.50
Mean	0	250.47	500.94	751.41	1001.88	1252.35	1502.82
STDEV	0	0.57	1.15	1.72	2.30	2.87	3.45

	Plate 8	**Plate 9**	**Plate 10**	**Plate 11**	**Plate 12**	**Plate 13**
0 mm	1745.61	1994.98	2244.36	2493.73	2743.10	2992.48
5 mm	1746.67	1996.19	2245.72	2495.24	2744.76	2994.29
10 mm	1748.85	1998.69	2248.52	2498.36	2748.19	2998.03
15 mm	1750.15	2000.18	2250.20	2500.22	2750.24	3000.26
20 mm	1751.34	2001.53	2251.72	2501.92	2752.11	3002.30
25 mm	1752.85	2003.26	2253.67	2504.08	2754.48	3004.89
30 mm	1753.52	2004.02	2254.52	2505.03	2755.53	3006.03
35 mm	1754.69	2005.36	2256.03	2506.70	2757.37	3008.04
40 mm	1755.73	2006.55	2257.37	2508.19	2759.01	3009.83
45 mm	1756.73	2007.69	2258.65	2509.61	2760.57	3011.53
50 mm	1757.02	2008.03	2259.03	2510.03	2761.04	3012.04
55 mm	1757.76	2008.87	2259.98	2511.09	2762.20	3013.31
60 mm	1757.52	2008.59	2259.67	2510.74	2761.82	3012.89
65 mm	1757.58	2008.67	2259.75	2510.83	2761.91	3013.00
mean	1753.29	2003.76	2254.23	2504.70	2755.17	**3005.64**
STDEV	4.02	4.60	5.17	5.75	6.32	6.89

TABLE C.41: Errors in measurement of the distance of the thin plates w.r.t Plate 1

	Plate 1	**Plate 2**	**Plate 3**	**Plate 4**	**Plate 5**	**Plate 6**
0 mm	0	23.58	47.15	70.73	94.31	117.89
5 mm	0	23.46	46.92	70.39	93.85	117.31
10 mm	0	23.77	47.54	71.31	95.08	118.85
15 mm	0	23.72	47.43	71.15	94.87	118.58
20 mm	0	23.77	47.54	71.31	95.09	118.86
25 mm	0	23.48	46.96	70.44	93.92	117.40
30 mm	0	23.80	47.60	71.41	95.21	119.01
35 mm	0	23.67	47.35	71.02	94.69	118.37
40 mm	0	23.62	47.25	70.87	94.50	118.12
45 mm	0	23.39	46.78	70.17	93.57	116.96
50 mm	0	23.83	47.65	71.48	95.30	119.13
55 mm	0	24.14	48.28	72.42	96.56	120.71
60 mm	0	24.14	48.28	72.42	96.56	120.69
65 mm	0	24.11	48.22	72.34	96.45	120.56
Mean	0	23.75	47.50	71.25	95.00	118.74
STDEV	0	0.25	0.49	0.74	0.98	1.23

	Plate 7	**Plate 8**	**Plate 9**	**Plate 10**	**Plate 11**	**Plate 12**
0 mm	141.46	157.72	173.98	190.24	206.50	222.76
5 mm	140.77	156.80	172.82	188.84	204.86	220.89
10 mm	142.62	158.73	174.84	190.96	207.07	223.19
15 mm	142.30	159.17	176.04	192.91	209.79	226.66
20 mm	142.63	159.22	175.82	192.41	209.01	225.60
25 mm	140.88	157.93	174.99	192.04	209.10	226.16
30 mm	142.81	159.66	176.50	193.35	210.19	227.04
35 mm	142.04	159.25	176.45	193.66	210.87	228.08
40 mm	141.75	158.20	174.66	191.11	207.57	224.02
45 mm	140.35	157.30	174.26	191.21	208.17	225.12
50 mm	142.96	159.30	175.64	191.98	208.32	224.66
55 mm	144.85	161.64	178.43	195.23	212.02	228.81
60 mm	144.83	161.93	179.03	196.13	213.23	230.33
65 mm	144.67	161.39	178.11	194.83	211.55	228.27
Mean	142.49	159.16	175.83	192.49	209.16	225.83
STDEV	1.47	1.59	1.78	2.02	2.30	2.61